CHALMERS

Correlation Work on Shaker Rig Tests and Simulations

An investigation of damper, bushing, friction and tire modeling with respect to vertical vibration insulation

Master's thesis in Automotive Engineering

OSKAR JONSON
ERIK ENDERS

Department of Applied Mechanics
Division of Vehicle Engineering and Autonomous Systems
Group of Vehicle Dynamics
CHALMERS UNIVERSITY OF TECHNOLOGY
Göteborg, Sweden 2016

MASTER'S THESIS IN AUTOMOTIVE ENGINEERING

Correlation Work on Shaker Rig Tests and Simulations

An investigation of damper, bushing, friction and tire
modeling with respect to vertical vibration insulation

OSKAR JONSON
ERIK ENDERS

Department of Applied Mechanics
Division of Vehicle Engineering and Autonomous Systems
Group of Vehicle Dynamics
CHALMERS UNIVERSITY OF TECHNOLOGY

Göteborg, Sweden 2016

Correlation Work on Shaker Rig Tests and Simulations
An investigation of damper, bushing, friction and tire
modeling with respect to vertical vibration insulation
Master's thesis in Automotive Engineering
OSKAR JONSON
ERIK ENDERS
Department of Applied Mechanics
Division of Vehicle Engineering and Autonomous Systems
Group of Vehicle Dynamics
Chalmers University of Technology

Abstract

In the Automotive Industry it becomes more and more important to reduce costs and cut down development time. It is one of the main challenges in order to stay competitive, also for the Volvo Car Cooperation, where this thesis work was carried out in cooperation with Chalmers University of Technology. With regard to Vehicle Dynamics, a large amount of the cost is generated while prototype cars need to be set-up and changed to meet requirements during the testing phase. With the increase in computational power and the availability of advanced software for vehicle dynamics simulations in recent years, it is now possible to do some of this work earlier in the design phase. The future goal is to use prototype testing mainly for validation of having met the requirements, rather than changing the car to achieve them. For this to be possible, it needs to be assured that the CAE methods are stable and show good correlation to physical testing. This thesis focuses on correlation of vertical vibration insulation simulations. The starting point was that shaker rig tests showed different results from shaker rig simulations in Adams Car. A thorough pre-study was performed to understand the theory of key areas for vertical vehicle dynamics, such as damper, bushing, tire and friction modeling. The technical background section of this work should therefore provide all the needed information to understand the carried out work, also for a reader new to this field. As a next step, simulation models are developed ranging from linear quarter car state-space models in MATLAB to more advanced non-linear quarter car models in Dymola. The most advanced Dymola model features a self-developed low-pass filter damper model, hydro engine mount and top mount bushings as well as different friction implementations. Friction modeling was also investigated with a full car model in Adams Car. Shaker rig, damper and suspension parameter measurement machine tests where conducted, to parametrize models and gain more insight into the physical phenomenas that are tried to be replicated. Friction was identified as the largest factor why simulations and tests do not correlate. The implementation of friction improved results significantly, especially at low frequencies. More accurate damper modeling that tries to capture the hysteresis loop in the Force-Velocity Diagram due to compressibility, cavitation and backlash, seems to have a smaller influence on shaker rig simulation correlation, especially in the low frequency range ($0 - 3$ Hz). It could be verified that accurate bushing and tire modeling is needed to obtain good correlation at higher frequencies ($3 - 20$ Hz). Convergence of simulations was found as a main issue for models that included friction. Validation of bushing and tire modeling, as well as accurate parametrization of friction and improved solve-ability of models with friction remain as future tasks.

Keywords: Vertical Vehicle Dynamics, Damper Modeling, Damper Testing, Bushing Modeling, Friction Modeling, Tire Modeling, Correlation, 4-Post Shaker Rig, SPMM, Vibration Insulation, Suspension, Eigenfrequency, Transmissibility, MATLAB, Dymola, Adams

Preface

This thesis work was conducted at Chalmers University of Technology in cooperation with Volvo Car Cooperation in the time between 15. January 2016 and 15. June 2016. The everyday work took place at the Volvo CAE Vehicle Dynamics Department in Gothenburg, physical testing was performed at Hällered Proving Ground, which is also part of the Volvo Car Cooperation. The work was supervised by Matthijs Klomp (Volvo) and Anton Albinsson (Chalmers). Examiner of this thesis was Mathias Lidberg, professor for Vehicle Dynamics at Chalmers.

We would like to thank our Supervisors Anton and Matthijs for their valuable inputs, advice and time spent to help us during our work. We would also like to thank Mathias for taking over the examination of this work besides having an already full enough time schedule. Many thanks also to our student colleagues Martin Ljunggren, Gunnar Sahlin, Karl-Johan Hagelin and Robert Samefors for many interesting conversations, work related as well as in our free time. Last but not least we would like to thank the people at the CAE Vehicle Dynamics Department and Hällered Proving Ground, as they always took their time and tried to help us where ever they could.

Nomenclature

Upper case Roman letters

A	constant for trail solution of a differential equation
B	constant for trail solution of a differential equation
C	constant for trail solution of a differential equation
$C_{1,2}$	constants for trail solution of a differential equation
C_d	damping coefficient at the damper
C_w	damping coefficient at the wheel
D	constant for trail solution of a differential equation
D_s	static deflection
E	Young modulus
F^*	external exciting force
F_0	exciting force amplitude
F_{ext}	external force
F_d	damper force
F_r	friction force
F_s	spring force
F_t	output force amplitude
F_z	normal force
$\mathcal{F}(x)$	Fourier transform of x
G_{amp}	amplitude gain w.r.t. static deflection
G_{ampD}	equivalent to G_{amp}
H	response amplitude
$H_{a \to b}$	transfer function from a to b
I	inertia
I_{cm}	inertia w.r.t. center of mass
Im	imaginary part of a complex number
K_w	wheel rate
K_s	spring rate
L	wheelbase
N	number of samples/data points
Q	exciting acceleration amplitude $\left(= \frac{F_0}{m} \right)$
Re	real part of a complex number
T	transmissibility
$T_{1,2}$	summarized terms for the solution of a force excited system
T_{dispD}	transmissibility for a displacement input
T_{forceF}	transmissibility for a force input
$T_{peak}(\xi)$	peak transmissibility as a function of frequency ratio
Z_e	engine displacement in z-direction
$\dot{Z}_e$	engine velocity in z-direction
$\ddot{Z}_e$	engine acceleration in z-direction
Z_r	road input displacement in z-direction
$\dot{Z}_r$	road input velocity in z-direction
$\ddot{Z}_r$	road input acceleration in z-direction
Z_{sm}	sprung mass displacement
$\dot{Z}_{sm}$	sprung mass velocity
$\ddot{Z}_{sm}$	sprung mass acceleration
Z_{um}	unsprung mass displacement
$\dot{Z}_{um}$	unsprung mass velocity
$\ddot{Z}_{um}$	unsprung mass acceleration

Lower case Roman letters

a	acceleration
c	damping coefficient
c^*	critical damping coefficient
c_e	engine mount damping
c_s	sprung mass damping
f	frequency
f	actual force
f_0	coulomb friction force level
g	gravity of the earth
i	imaginary unit
k	spring stiffness
k_e	engine mount stiffness
k_s	sprung mass spring stiffness
l_c	length of lower control arm
l_d	length from lower inner hardpoints to damper attachment point
l_f	distance between front axle and CoG in x-direction
l_r	distance between CoG and rear axle in x-direction
m	mass
m_e	engine mass
q	overdamped solution for the characteristic equation
r_m	motion ration
s_a	acceleration shape factor (curve factor)
s_d	damper displacement
s_w	wheel displacement
t	time
$u(t)$	ansatz-function for a trial solution
v	velocity
v_{rel}	relative velocity
v_s	Stribeck velocity
z	displacement in z-direction
$\dot{z}$	velocity in z-direction
$\ddot{z}$	acceleration in z-direction
z_{hom}	homogeneous solution for z-displacement
z_{par}	particular solution for z-displacement
z_r	road input displacement in z-direction
$\dot{z}_r$	road input velocity in z-direction
$\ddot{z}_r$	road input acceleration in z-direction
z_s	suspended mass displacement in z-direction
$\dot{z}_s$	suspended mass velocity in z-direction
$\ddot{z}_s$	suspended mass acceleration in z-direction
z_t	trial solution for displacement in z-direction

Abbreviations

CoG	Center of Gravity
HHT	Hilbert-Hughes-Taylor method
K&C	Kinematics and Compliance
LuGre	Lund-Grenoble (friction model)
MNF	Modal Neutral File
SPA	Volvo Scalable Product Platform
SPMM	Suspension Parameter Measurement Machine (also used as K&C test-rig)
SR	Shaker Rig

Greek letters

α	damper installation angle
β	constant for trial solution
$\delta(f)$	dirac delta function of frequency
ϵ	strain
$\dot{\epsilon}$	rate of strain
η	viscosity
λ	eigenvalue of the characteristic equation
μ	coefficient of friction
μ_{stat}	static friction coefficient
μ_{dyn}	dynamic friction coefficient
μ_v	dynamic friction level (μ_{dyn})
Ω	excitation frequency
ω_0	undamped eigenfrequency
ω_D	damped eigenfrequency
ν	damping exponent
ϕ	phase shift
σ	stress
σ_0	bristle stiffness
σ_1	bristle damping
φ	phase angle
φ_{in}	phase angle of the input
φ_R	phase angle of the response
ξ	frequency ratio
ξ_A^*	frequency ratio for the peak in amplitude gain
ξ_T^*	frequency ratio for the peak in transmissibility
ζ	damping factor/damping ratio

CONTENTS

List of Figures

List of Tables

1 Introduction

This thesis is conducted in cooperation with Volvo Cars Cooperation. It aims to improve simulation correlation with respect to vertical vibration insulation in a vehicle. This is important to be able to evaluate the ride comfort in early stages of the design process to shorten development times and reduce costs. It also helps to obtain design targets for components such as bushings, springs and dampers. Another advantage is that requirements regarding ride comfort can be continuously followed up during the design phase.

1.1 Background

Today, most of the CAE ride comfort analysis is done with full vehicle models in advanced simulation software as ADAMS Car or Dymola. In early concept phases, these models have to be simplified, since not all design parameters are known at this stage. These models are mainly used to evaluate different design concepts. For this to be useful, the accuracy of these models has to be known and should be as good as possible. For quasi-static analysis of the kinematics and compliance (K&C) of a suspension, these methods are well developed and have good correlation to real tests. What is missing are corresponding methods and evaluation criteria for the dynamic analysis of the suspension system with regard to vertical excitations. As of now, requirements and the initial designs are based on previous experience. At a later stage during the development, prototypes are used to evaluate the performance of the car with respect to the set requirements. If these requirements are not fulfilled, the suspension system gets tuned and changed in order to achieve the best possible result. These tests, as well as design changes at this stage, are expensive and should be minimised. The aim is to use CAE methods to evaluate and test the car at an earlier stage, when it is easier to implement bigger changes. Simulations are in general cheaper and faster than real tests. A reliable and accurate CAE model early in the development phase could therefore be used to optimise the design and reduce the amount of physical testing down to verification of simulation results. This would help to reduce development costs as well as cycle times and would therefore result in a better position for the Volvo Car Cooperation in the international competition with other car companies.

1.2 Purpose

The aim of this thesis is to investigate the correlation between shaker rig tests and virtual (CAE) test methods. Currently there is a discrepancy of the eigenfrequencies of the suspension system evaluated in laboratory tests on a 4-post shaker rig, compared to the ones obtained by simulation of CAE models. To evaluate ride comfort in a CAE environment, better models that capture the dynamic characteristics of the suspension accurately are needed. This thesis will investigate the source of the discrepancies as well as creating appropriate models for dynamic suspension analysis. Focus lies on generating knowledge in all relevant areas for vertical vibration insulation, because at the Volvo Car Cooperation vertical vehicle dynamics are not as well known as the area of lateral and longitudinal dynamics.

1.3 Research Questions

The main question for this thesis is to investigate where the difference from simulation results to real tests is originating from. Finally the question should be answered, if and how different models of a part, such as dampers, bushings and friction or tires can be improved in order to obtain higher correlation.

1.4 Delimitations

The thesis will not treat the theory of subjective comfort, but will be limited to analyse transmissibility through the suspension with respect to the sprung mass (SM) and unsprung mass (UM). Furthermore the focus will lie on the comparison of simulations and shaker rig test with sinusoidal input signals. Random inputs signals as well as real road data input will not be investigated.

2 Theory

This chapter starts with a section on vibration theory, followed by a simple introduction to different suspension components. Finally simple representations of these components are presented.

2.1 Vibration theory

In dynamics, an oscillating system is described by the following ordinary second order differential equation:

$$m\ddot{z}(t) + c\dot{z}(t) + kz(t) = F^* \tag{2.1}$$

For a single degree of freedom system, m, c, k and F_0 are constants. For multi degree of freedom systems they become matrices. In both cases m contains information about the mass, c about the damping, k about the stiffness and F^* about the external forces. For freely oscillating systems

$$F^* = 0 \tag{2.2}$$

for harmonically forced oscillations

$$F^* = F_0 \sin(\Omega t) \tag{2.3}$$

and for general forced oscillations

$$F^* = F(t) \tag{2.4}$$

Gravity is not included in the equations of motion since it only generates an off-set in the initial position and doesn't influence the dynamic behavior of the system.

2.1.1 Undamped-free oscillations

In case of an undamped and free oscillation (Figure 2.1), c and F^* are zero. The differential equation (2.1) becomes:

$$m\ddot{z}(t) + kz(t) = 0 \tag{2.5}$$

$$\Leftrightarrow \quad \ddot{z}(t) + \frac{k}{m}z(t) = 0 \tag{2.6}$$
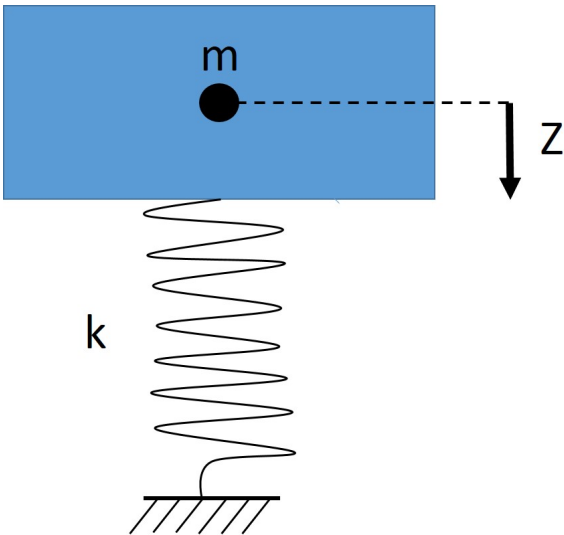
Figure 2.1: *Model for undamped free oscillations (1 DOF)*

This equation can be solved with the help of a trial solution

$$z_t(t) = Ce^{\lambda t} \tag{2.7}$$

The characteristic equation of Equation 2.6

$$\lambda^2 + \frac{k}{m} = 0 \tag{2.8}$$

yields the two eigenvalues

$$\lambda_{1,2} = \pm i\sqrt{\frac{k}{m}} \tag{2.9}$$

where

$$\omega_0 = \sqrt{\frac{k}{m}} \tag{2.10}$$

is the eigenfrequency of the undamped system. Since both eigenvalues are linearly independent solutions of the differential equation, the trial solution becomes:

$$z(t) = C_1 e^{i\omega_0 t} + C_2 e^{-i\omega_0 t} \tag{2.11}$$

With the help of the Euler's Formula this solution can be rewritten in trigonometric functions as:

$$\begin{aligned}
z(t) &= C_1 e^{i\omega_0 t} + C_2 e^{-i\omega_0 t} \\
&= D\cos(\omega_0 t + \varphi) \\
&= A\cos(\omega_0 t) + B\sin(\omega_0 t).
\end{aligned} \tag{2.12}$$

C_1, C_2, D, φ, A and B are constants, which are determined for specific solutions with the help of initial and/or boundary conditions. The Equations 2.12 describes the behavior of the system in the time domain. Another option to describe a system like this would be in the frequency domain. This is useful to analyse a systems behavior and will be shown later.

2.1.2 Damped-free oscillations

For a free oscillating damped system as shown in Figure 2.2 Equation 2.1 becomes:

$$m\ddot{z} + c\dot{z} + kz = 0 \tag{2.13}$$

$$\Leftrightarrow \quad \ddot{z} + \frac{c}{m}\dot{z} + \frac{k}{m}z = 0 \tag{2.14}$$
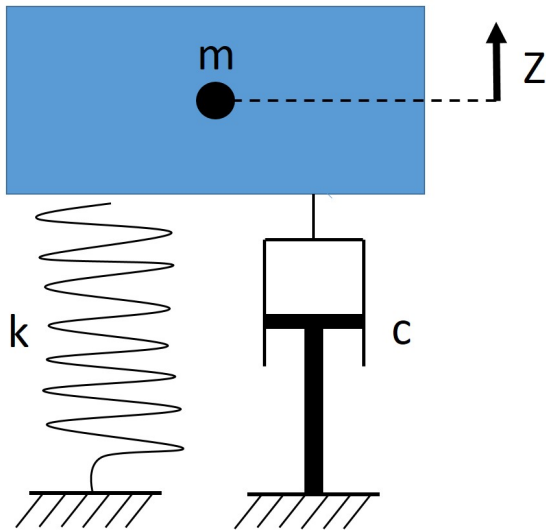
Figure 2.2: *Model for damped free oscillations (1 DOF)*

To solve this equation the damping exponent

$$\nu = \frac{c}{2m} \tag{2.15}$$

is introduced and a trial solution

$$z_t = e^{-\beta t} u(t) \tag{2.16}$$

is used in order to rewrite Equation 2.14 in the form of Equation 2.6. [Mil06] By using Equation 2.15, Equation 2.14 can be rewritten as:

$$\ddot{z} + 2\nu\dot{z} + \omega_0^2 z = 0 \tag{2.17}$$

where ω_0 is the undamped eigenfrequency. Inserting Equation 2.16 into Equation 2.17 yields:

$$\frac{\mathrm{d}^2}{\mathrm{d}t^2}\left[e^{-\beta t}u(t)\right] + 2\nu\frac{\mathrm{d}}{\mathrm{d}t}\left[e^{-\beta t}u(t)\right] + \omega_0^2 e^{-\beta t}u(t) = 0 \tag{2.18}$$

Deriving the terms in the brackets gives:

$$\left[\beta^2 e^{-\beta t}u(t) - 2\beta e^{-\beta t}\dot{u}(t) + e^{-\beta t}\ddot{u}(t)\right] + 2\nu\left[-\beta e^{-\beta t}u(t) + e^{-\beta t}\dot{u}(t)\right] + \omega_0^2 e^{-\beta t}u(t) = 0 \tag{2.19}$$

which can be simplified to:

$$e^{-\beta t}\ddot{u}(t) + 2\left(\nu - \beta\right)e^{-\beta t}\dot{u}(t) + \left(\beta^2 - 2\nu\beta + \omega_0^2\right)e^{-\beta t}u(t) = 0 \tag{2.20}$$

Choosing $\beta = \nu$ in order to get rid of the damping term ($\dot{u}(t)$) and dividing by $e^{-\beta t}$ gives:

$$\ddot{u}(t) + \left(\omega_0^2 - \nu^2\right)u(t) = 0 \tag{2.21}$$

It can be see that Equation 2.21 is the same form as Equation 2.6, which can also be written as:

$$\ddot{z}(t) + \omega_0^2 z(t) = 0 \tag{2.22}$$

The only difference is that now the stiffness term is not unconditionally non-zero and positive, but instead depends on the magnitude of the damping exponent ν in relation to the undamped eigenfrequency ω_0. There are three different cases (Table 2.1) which can be expressed with the help of the damping factor ζ:

$$\zeta = \frac{\nu}{\omega_0} \tag{2.23}$$

Table 2.1: Different solutions for a damped system

Name	Damping Factor
Under-damped	$0 < \zeta < 1$
Critical-damped	1
Over-damped	$\zeta > 1$

Inserting Equation 2.15 into Equation 2.23 and rearranging yields the critical damping coefficient c^*:

$$c^* = 2\sqrt{km} \tag{2.24}$$

The damping factor can therefore also be expressed in terms of the damping coefficient as:

$$\zeta = \frac{c}{c^*} \tag{2.25}$$

The response of the system for different damping ratios in the time domain can be seen in Figure 2.3
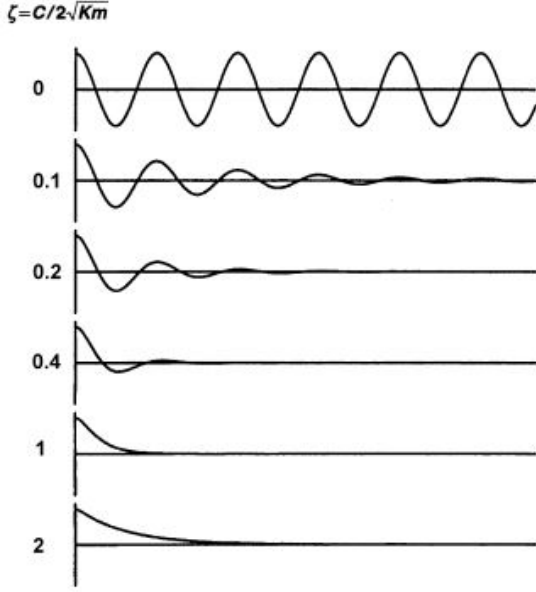
Figure 2.3: *Response for a self oscillating system with linear damping and different damping ratios [Dix07]*

Using Equation 2.23 the stiffness term can be reformulated as follows:

$$\omega_0^2 - \nu^2 = \omega_0^2 - \zeta^2 \omega_0^2 = \omega_0^2 \left(1 - \zeta^2\right) \tag{2.26}$$

From the characteristic equation we obtain the eigenvalues:

$$\lambda_{1,2} = \pm i\omega_0 \sqrt{1 - \zeta^2} \tag{2.27}$$

In case $\zeta < 1$ the eigenvalues are imaginary which means the solution is oscillatory and the damped eigenfrequency of the freely oscillating system can be identified as:

$$\omega_D = \omega_0 \sqrt{1 - \zeta^2} \tag{2.28}$$

If $\zeta = 1$ the eigenvalues become 0 (double eigenvalue):

$$\lambda_{1,2} = 0 \tag{2.29}$$

The solution is not oscillatory but instead linear. If $\zeta > 1$ the eigenvalues become real:

$$\lambda_{1,2} = \pm i\omega_0 \sqrt{-1(\zeta^2 - 1)} = \pm i\omega_0 \sqrt{-1}\sqrt{\zeta^2 - 1} = \pm i^2 \omega_0 \sqrt{\zeta^2 - 1} = \mp \omega_0 \sqrt{\zeta^2 - 1} \tag{2.30}$$

This gives a hyperbolic solution. The solutions for the underdamped and the overdamped case for Equation 2.21 can be obtained by inserting the eigenvalues into the trial solution (Equation 2.7) similar to the undamped case. Therefore the solution for the underdamped case becomes:

$$u(t) = C_1 e^{i\omega_D t} + C_2 e^{-i\omega_D t} = A \cos(\omega_D t) + B \sin(\omega_D t) \tag{2.31}$$

The solution for the overdamped case defining $q = \omega_0 \sqrt{\zeta^2 - 1}$ reads:

$$u(t) = C_1 e^{qt} + C_2 e^{-qt} \tag{2.32}$$

For the critical damped case Equation 2.21 reduces to:

$$\ddot{u}(t) = 0 \tag{2.33}$$

The solution can be obtained by integrating twice and reads:

$$u(t) = A + Bt \tag{2.34}$$

The solutions for Equation 2.14 can now be found by substituting the solutions for $u(t)$ into Equation 2.16. Underdamped case:

$$z(t) = e^{-\nu t} \left[A \cos(\omega_D t) + B \sin(\omega_D t) \right] \tag{2.35}$$

The factor in front of the brackets is the damping term and is responsible for the amplitude of the oscillatory motion approaching zero with time:

$$\lim_{t \to \infty} z(t) = 0 \tag{2.36}$$

The term in the brackets is the oscillatory part similar to the undamped case. The only difference is that the system oscillates with the damped eigenfrequency ω_D instead of the undamped eigenfrequency ω_0. The solution for the critical damped case is:

$$z(t) = e^{-\nu t} \left[A + Bt \right] \tag{2.37}$$

The damping term in front of the brackets stays the same. In the brackets however there is only a linear term which doesn't oscillate. The amplitude will therefore approach the zero position without any overshoot. The solution to the overdamped case is:

$$z(t) = e^{-\nu t} \left[C_1 e^{qt} + C_2 e^{-qt} \right] \tag{2.38}$$

The term in the brackets is a hyperbolic term this time and will delay the approach of the amplitude towards zero compared to the critical damped case.

2.1.3 Damped-forced oscillations with a force input

Considering now a harmonically forced oscillating damped system, Equation 2.17 becomes:

$$\ddot{z} + 2\nu \dot{z} + \omega_0^2 z = Q \sin(\Omega t) \tag{2.39}$$

where $Q = \frac{F_0}{m}$ with F_0 being the disturbing/exciting force, so that Q represents the exciting accaleration. The disturbance term on the right hand side represents the external force that excites the system with an amplitude Q and a frequency Ω. Figure 2.4 shows an example system for this case.
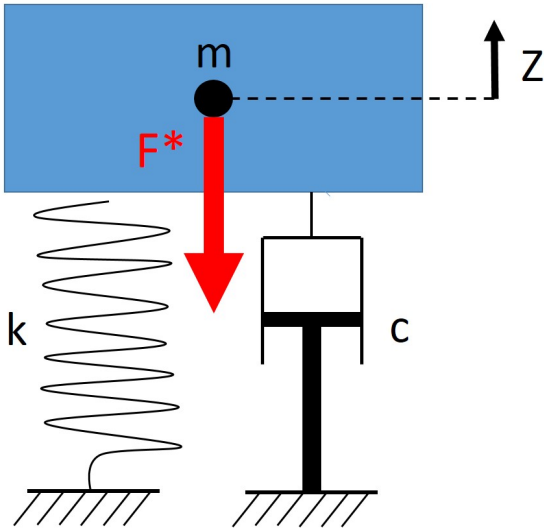
Figure 2.4: *Model for damped forced oscillations with force input (F*) (1 DOF)*

Mathematically, this differential equation now also has particular solution in addition to the homogeneous solution of differential equation for the freely oscillating system:

$$z(t) = z_{hom}(t) + z_{par}(t) \tag{2.40}$$

To solve for the particular solution, again a trial solution approach is used. The function for the trial solution depends on the type of function for the disturbance. For the harmonic disturbance the following trial solution is used:

$$z_{par}(t) = C_1 \sin(\Omega t) + C_2 \cos(\Omega t) \tag{2.41}$$

Inserting Equation 2.41 into Equation 2.39 yields:

$$\frac{\mathrm{d}^2}{\mathrm{d}t^2}\left[C_1\sin(\Omega t) + C_2\cos(\Omega t)\right] + 2\nu\frac{\mathrm{d}}{\mathrm{d}t}\left[C_1\sin(\Omega t) + C_2\cos(\Omega t)\right] +$$
$$+\omega_0^2\left[C_1\sin(\Omega t) + C_2\cos(\Omega t)\right] = Q\sin(\Omega t) \tag{2.42}$$

Deriving the terms in brackets yields:

$$-C_1\Omega^2\sin(\Omega t) - C_2\Omega^2\cos(\Omega t) + 2\nu C_1\Omega\cos(\Omega t) - 2\nu C_2\Omega\sin(\Omega t)+$$
$$+C_1\omega_0^2\sin(\Omega t) + C_2\omega^2\cos(\Omega t) = Q\sin(\Omega t) \tag{2.43}$$

This can be rearranged to:

$$T_1 sin(\Omega t) + T_2 cos(\Omega t) = 0 \tag{2.44}$$

with

$$T_1 = (\omega_0^2 - \Omega^2)C_1 - 2\nu\Omega C_2 - Q \tag{2.45}$$
$$T_2 = (\omega_0^2 - \Omega^2)C_2 + 2\nu\Omega C_1 \tag{2.46}$$

For Equation 2.44 to hold true, the condition $T_1 = 0 \wedge T_2 = 0$ must be fulfilled. This give two equations for two unknowns and yields:

$$C_1 = \frac{\frac{Q}{\omega_0^2-\Omega^2}}{1 + \frac{4\nu^2\Omega^2}{(\omega_0^2-\nu^2)^2}} \tag{2.47}$$

$$C_2 = -\frac{2\nu\Omega}{\omega_0^2 - \Omega^2}C_1 \tag{2.48}$$

Introducing the frequency ratio

$$\xi = \frac{\Omega}{\omega_0} \tag{2.49}$$

and the static deflection

$$D_s = \frac{F_0}{k} = \frac{Q}{\omega_0^2} \tag{2.50}$$

C_1 and C_2 can be rewritten as:

$$C_1 = \frac{D_s(1 - \xi^2)}{(1 - \xi)^2 + (2\zeta\xi)^2} \tag{2.51}$$

$$C_2 = \frac{-2D_s\xi\zeta}{(1 - \xi^2)^2 + (2\xi\zeta)^2} \tag{2.52}$$

The general solution to Equation 2.39 becomes:

$$z(t) = e^{-\nu t}u(t) + C_1 sin(\Omega t) + C_2 cos(\Omega t) \tag{2.53}$$

In this case the homogeneous part of the solution, which is the same as for the free vibrating system, is called the transient part since it will vanish with time after the system excitement has begun. The second part (particular solution) is called the steady state part of the solution. This term will determine the behavior of the system long enough after the start of excitement. Using this steady state term, two important response criteria can be defined. The response amplitude is calculated as:

$$H = \sqrt{C_1^2 + C_2^2} = \frac{D_s}{\sqrt{(1 - \xi^2)^2 + (2\xi\zeta)^2}} \tag{2.54}$$

and the response phase angle as:

$$\varphi_R = \arctan\left(-\frac{C_2}{C_1}\right) = \arctan\left(\frac{2\xi\zeta}{1 - \xi^2}\right) \tag{2.55}$$

The steady state amplitude gain is then defined as

$$G_{amp} = \frac{H}{D_s} \tag{2.56}$$

and the phase shift as

$$\phi = \varphi_R - \varphi_{in} \tag{2.57}$$

where φ_R is the phase of the response and φ_{in} is the phase of the input (disturbance). From Equation 2.54 it can be seen that the gain in Amplitude is calculated as:

$$G_{amp} = \frac{1}{\sqrt{(1 - \xi^2)^2 + (2\xi\zeta)^2}} \tag{2.58}$$

Assuming a system with fixed parameters, where the only variable is the exciting frequency Ω and therefore ξ, it can be followed that $G_{amp} \simeq 1$ for $\xi \simeq 0$ and $G_{amp} \simeq 0$ for $\xi \to \infty$. To find the frequency ratio that gives the highest amplitude gain for a certain system, Equation 2.58 is derived and set to zero:

$$\frac{\partial}{\partial\xi} G_{amp}(\xi, \zeta) = \frac{(2 - 2\xi^2)(-2\xi) + 8\zeta^2}{2\left[(1 - \xi^2)^2 + (2\xi\zeta)^{\frac{3}{2}}\right]} \stackrel{!}{=} 0 \tag{2.59}$$

This statement can only be fulfilled if the numerator is zero. It follows that

$$(2 - 2\xi^2)(-2\xi) + 8\zeta^2 \stackrel{!}{=} 0 \tag{2.60}$$

and the frequency ratio ξ^* for the peak[1] in amplitude gain is given as:

$$\xi_A^* = \sqrt{1 - 2\zeta^2} \tag{2.61}$$

To obtain the transmissibility, the output force amplitude F_t is set in relation to the input force amplitude F_0:

$$T = \frac{F_t}{F_0} \tag{2.62}$$

The output force consisting out of the damper force F_d and the spring force F_s. For the steady state motion these are given as:

$$F_s = kH \sin(\Omega t - \lambda) \tag{2.63}$$
$$F_d = cH\Omega \cos(\Omega t - \lambda) \tag{2.64}$$

The output force amplitude is consequently calculated as:

$$F_t = \sqrt{\hat{F}_s^2 + \hat{F}_d^2} = H\sqrt{k^2 + c^2\Omega^2} \tag{2.65}$$

Using Equation 2.58 and 2.50, the transmissibility can be calculated as:

$$T = G_{amp} \frac{\sqrt{k^2 + c^2\Omega^2}}{k} = G_{amp}\sqrt{1 + \frac{c^2\Omega^2}{k^2}} \tag{2.66}$$

Using the fact that

$$\frac{c^2\Omega^2}{k^2} = (2\xi\zeta)^2 \tag{2.67}$$

and Equation 2.58 gives:

$$T = \sqrt{\frac{1 + (2\xi\zeta)^2}{(1 - \xi^2)^2 + (2\xi\zeta)^2}} \tag{2.68}$$

To obtain the frequency ratio at which the peak transmissibility occurs, Equation 2.68 is derived and set to zero:

$$\frac{\partial}{\partial\xi} T(\xi, \zeta) = \frac{2\xi(2\zeta^2\xi^4 + \xi^2 - 1)}{\sqrt{\frac{4\zeta^2\xi^2 + 1}{\xi^4 + (4\zeta^2 - 2)\xi^2 + 1}}(\xi^4 + 4\xi^2\zeta^2 - 2\xi^2 + 1)^2} \stackrel{!}{=} 0 \tag{2.69}$$

This yields:

$$\xi_T^* = \sqrt{\frac{\sqrt{2(2\zeta)^2 + 1} - 1}{(2\zeta)^2}} \tag{2.70}$$

---

[1] Can be checked with the second derivative

2.1.4 Damped-forced oscillations with a displacement input

A system can not only be excited with a force input, but also with a displacement input. Figure 2.5 shows a representative damped one mass system for this case.
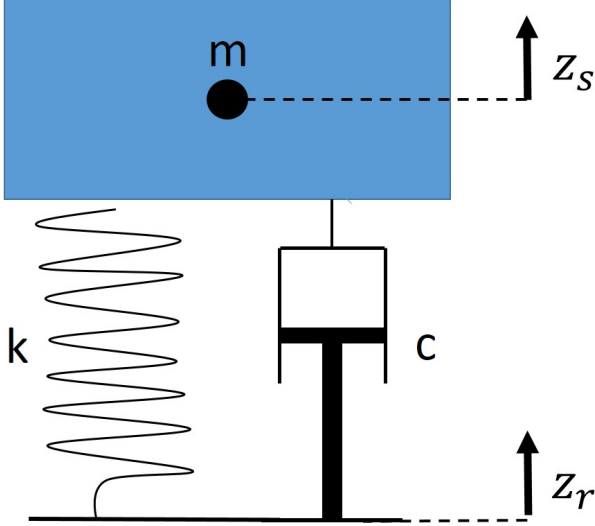
Figure 2.5: *Model for damped forced oscillations with displacement input (z_r) (1 DOF)*

For this case the equations of motion become:

$$k(z_r - z_s) + c(\dot{z}_r - \dot{z}_s) - m\ddot{z}_s = 0 \tag{2.71}$$

this can be rearranged to

$$m\ddot{z}_s + c\dot{z}_s + kz_s = kz_r + c\dot{z}_r \tag{2.72}$$

assuming an harmonically excited system

$$z_r = A\sin(\Omega t) \tag{2.73}$$

and Equation 2.71 can be rewritten as

$$\ddot{z}_s + \frac{c}{m}\dot{z}_s + \frac{k}{m}z_s = \frac{k}{m}A\sin(\Omega t) + \frac{c}{m}A\Omega\cos(\Omega t) \tag{2.74}$$

which is equal to

$$\ddot{z}_s + 2\nu\dot{z}_s + \omega_0^2 z_s = \omega_0^2 A\sin(\Omega t) + 2\nu A\Omega\cos(\Omega t) \tag{2.75}$$

Using again the trial solution

$$C_1\sin(\Omega t) + C_2\cos(\Omega t) \tag{2.76}$$

and inserting it into Equation 2.75 yields following to expressions for the two coefficients:

$$C_1 = A\frac{(4\zeta^2 - 1)\xi^2 + 1}{\xi^4 + (4\zeta^2 - 2)\xi^2 + 1} \tag{2.77}$$

$$C_2 = A\frac{2\xi^3\zeta}{2\xi^2(2\zeta^2 - 1) + 4\xi^4 + 1} \tag{2.78}$$

The response amplitude therefore becomes

$$H = \sqrt{C_1^2 + C_2^2} = A\sqrt{\frac{4\zeta^2\xi^2 + 1}{\xi^4 + (4\zeta^2 - 2)\xi^2 + 1}} = A\sqrt{\frac{1 + (2\xi\zeta)^2}{(1 - \xi^2)^2 + (2\xi\zeta)^2}} \tag{2.79}$$

The amplitude gain for the forced oscillating syhstem with displacement input is therefore

$$G_{ampD} = \frac{H}{A} = \sqrt{\frac{1 + (2\xi\zeta)^2}{(1 - \xi^2)^2 + (2\xi\zeta)^2}} \tag{2.80}$$

Since it relates the output and the input quantity it is also the transmissibility for the displacement input. Note that this is the same Equation as for transmissibility in case of a force input.

$$T_{dispD} = G_{ampD} = T_{forceF} \tag{2.81}$$

The frequency ratio for peak transmissibility is therefore also calculated according to Equation 2.70. Rearranging for the inverse of Equation 2.70

$$\zeta(\xi) = \frac{\sqrt{2(1 - \xi^2)}}{2\xi^2} \tag{2.82}$$

and substituting ζ in Equation 2.80/2.68 gives an equation for peak transmissibility as a function of the frequency ratio:

$$T_{peak}(\xi) = \sqrt{-\frac{1}{\xi^4 - 1}} \tag{2.83}$$

Figure 2.6 shows transmissibility over frequency ratio for different damping ratios (coloured lines, Equations 2.80/2.68) and the function for peak transmissibility(Equation 2.83). It can be seen that with decreasing damping the frequency ratio for peak transmissibility is approaching 1. For increasing damping ratios ($\zeta > 1$) the peak is decreasing and moving towards $\xi = 0$:

$$\lim_{\zeta \to \infty} \xi_T^*(\zeta) = 0 \tag{2.84}$$
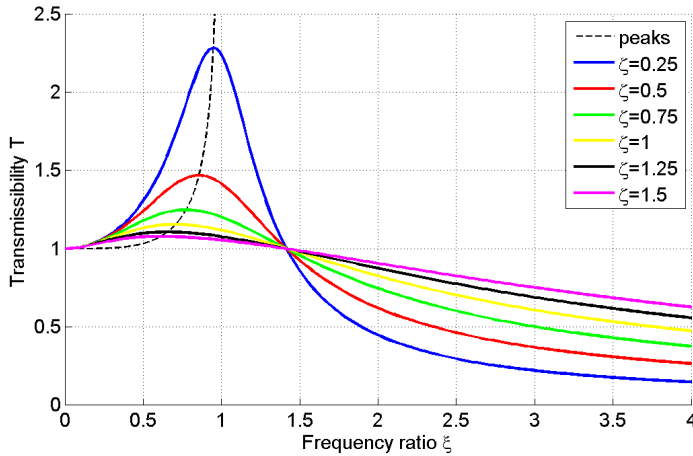
Figure 2.6: *Transmissibility as a function of frequency ratio with different amounts of critical damping*

2.1.5 Rotating half car model

Another interesting representation is to model the entire car body in two dimensions, letting one wheel axle pivot freely as can be seen in Figure 2.7. This model is useful since the 4-post shaker rig test is done by exciting only one axle at a time. The rotation is assumed to be around the rear tire contact point. This due to small excitation amplitudes and suspension friction which prevents any suspension movement of the non-excited axle. This creates a rotation of the body and is thus not equivalent to a one dimensional translating quarter car model using the static weights of the vehicle.
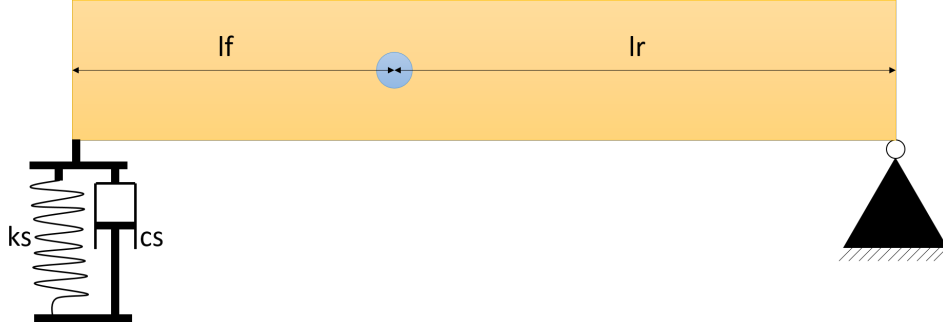
Figure 2.7: *Model of pivoting half car*

The transfer function for a model like this becomes similar to the transfer function one obtains for a similar one mass quarter car model (the difference is that this equation is dependent on inertia properties instead of mass). Doing a free body diagram and taking the moment equilibrium around the pivoting point you obtain Equation 2.85. Here the angular acceleration in the right hand side of the equation is substituted according $\dot{\omega} \approx \ddot{Z}_{sm}/L$ assuming small angles.

$$kL(Z_r - Z_{sm}) + cL(\dot{Z}_r - \dot{Z}_{sm}) - mgL_r = I\ddot{Z}_{sm}/L \tag{2.85}$$

Here $L = L_f + L_r$ and I is the pitch inertia with respect to the pivot point. Fourier transforming 2.85 we obtain the transfer function as Equation 2.86.

$$\frac{\mathcal{F}(Z_{sm})}{\mathcal{F}(Z_r)} = \frac{-k - i\omega c}{\omega^2 \frac{I}{L^2} + i\omega c + k} \tag{2.86}$$

To ensure that the result from this model would be comparable to a translating model, the pivoting car model is now compared to the translating one mass model. Using the transfer function for a translating one mass model[2] and the transfer function for the pivoting one mass model in Equation 2.86 we can derive an equation that needs to hold true, so that the rotational and translational model will yield the same result:

$$\left(\frac{\mathcal{F}(Z_{sm})}{\mathcal{F}(Z_r)}\right)_{rot} = -\frac{k + i\omega c}{\omega^2 \frac{I}{L^2} - i\omega c - k} \stackrel{!}{=} -\frac{k + i\omega c}{m_f \omega^2 - i\omega c - k} = \left(\frac{\mathcal{F}(Z_{sm})}{\mathcal{F}(Z_r)}\right)_{trans} \tag{2.87}$$

This can be simplified to:

$$I = m_f L^2 \tag{2.88}$$

Since the car is rotating around the rear axle, Steiner's principle needs to be used to calculate the Inertia ($I = I_{cm} + ml_r^2$). The mass of the front axle (m_f) is reformulated as $m_f = \frac{l_r}{L}m$ and the wheelbase L is expressed as $L = l_r + l_f$. With this the following relation can be obtained:

$$\frac{I_{cm}}{ml_r^2} = \frac{l_f}{l_r} \tag{2.89}$$

This means that the ratio, between the Inertia around the y-axis with respect to center of gravity of the car to the Steiner momentum[3], must be equal to the ratio, of front axle distance to center of gravity to the rear axle distance to the center of gravity. This derivation is only true for small angles. Using the values of Volvo Car B this equation is fulfilled with an error of 1.2%.

2.2 Suspension system components with respect to vertical vibration insulation

The primary objective of road car suspensions is to make the car travel comfortable and safe, with desirable handling characteristics according to the car type[4]. With regard to vertical dynamics, the main function of

---

[2]For this derivation the front axle is taken

[3]assuming small angles as in the model derivation

[4]There are different requirements for e.g. sports cars, limousines or SUV:s

springs is smoothing the chassis motion due to road input by absorbing abrupt increases in tire normal force. Dampers are added to the system to avoid large excitations of the chassis at road input close to the sprung mass (SM) and unsprung mass (UM) eigenfrequency. They also reduce the amount of energy stored (while compression) and released (while extension) of the spring when driving over a bump. Hence they help to maintain a controlled motion of the chassis in pitch, heave and yaw. When it comes to transmissibility at higher frequencies (vibrations/noise), the other connections between the wheel and the chassis need to be taken into consideration as well. To avoid transfer of disturbances from the wheel to the chassis, suspension pick-up points are designed as joints including rubber bushings, which act as isolators. The tire characteristics, especially the vertical stiffness, also influences the vibration insulation performance of a car. All these parts will be analysed in more detail in the next subsections.

2.2.1 Suspension layouts

The front axle from Volvo's SPA platform has a double A-arm suspension combined with a spring-damper strut (Figure 2.8 left side). The rear axle features a multi-link suspension with a transversely mounted composite leaf spring (Figure 2.8 right side).

Figure 2.8: *The Spa-platform used in the Volvo XC90, S90 and V90. Left: front suspension; Right: rear suspension*

As can be seen in the picture, the lower front suspension pick up points are connected to an axle carrier. All inner wishbone pick up points and the strut top mount contain rubber bushings to decouple the chassis from vibrations in the unsprung assembly. The same goes for the inner hardpoints in the rear. Additionally there are Anti-Roll Bars (ARB:s) in the front and at the rear. They are supported by mounts on the axle carrier which also include rubber bushings. The lower end of the damper in the front is attached with a fork to the lower control arm. The coil spring sits on the damper strut and is directly attached to the chassis at the top. The leaf spring in the rear is also attached to the lower control arm and is supported my two mounts at the rear wheel carrier. The damper in the rear is again mounted to the lower control arm at the bottom and attached to the chassis (with rubber bushing) at the top.

An important kinematic property of a suspension when it comes to stiffness and damping is the so called Motion ratio (MR). It is normally defined as:

$$r_m = \frac{\partial s_d}{\partial s_w} \approx \frac{l_d}{l_c} \cos(\alpha) \tag{2.90}$$

Where s_d is damper displacement and s_w is wheel displacement. Sometimes it is defined the other way around, so it should always be checked how it is implemented in a software or how the author of a book uses it. It should also be noted that the MR is not a constant and normally changes over suspension travel. This definition also assumes the tire as stiff. Figure 2.9 shows the geometrical relations needed to calculate the motion ratio. Even though the real case is more complex, this shows some of the most important aspects. The wheel rate, which is the effective stiffness at a wheel, is calculated as:

$$K_w = \frac{F_w}{s_w} = \frac{F_s r_m}{\frac{s_s}{r_m}} = K_s r_m^2 \tag{2.91}$$

And the effective damping rate is calculated as:

$$C_w = C_d r_m^2 \tag{2.92}$$

This means that with a decreasing ratio of l_d to l_c, or an increasing angle α, the motion ratio decreases and therefore a stiffer spring and more damping are needed to maintain the desired characteristics at the wheel.
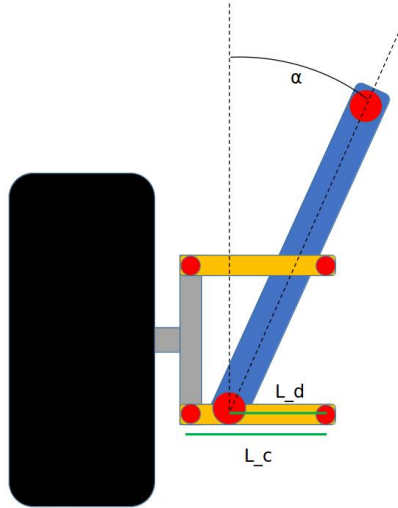
Figure 2.9: *Simplified model to calculate the motion ratio*

This explanation of the motion ratio assumes that the distance from the instantaneous center to the wheel center is roughly equal to the distance to the outer lower hardpoint and that therefore the aforementioned ratios of the distances at the lower control arm can be used. The problem also becomes three dimensional. In practice the motion ratio is calculated with the help of more advanced trigonometry. Usually this is solved using a multi-body simulation software. Further quantities that have an influence on the wheel rate are parasitic stiffness's from bushings and anti-roll bars, as well as the center of pressure position of the contact patch.

2.2.2 Bushings

In suspension systems bushings are used in joints to improve ride comfort. They act as isolators to reduce the transmission of vibrations and shocks from the unsprung part of the suspension to the chassis. When it comes to ride comfort the bushings should be soft and provide good damping (i.e compliant bushings). [HE11] However for handling it is usually desirable with stiffer bushings. This since the deformation of the bushings allow for relative movements of the connected parts, thus also affecting the suspension kinematics when the system is subjected to additional loads under cornering or braking. These so called elasto-kinematic effects are not necessarily unwanted from a handling perspective, nowadays they are effectively used to influence the dynamic behavior of modern vehicles. [Web09]. Figure 2.10 shows some different bushings that can be found in road car suspensions.

Figure 2.10: *Different bushings used in suspenion systems [HE11]*

The small bushings are the ones that are mainly used in the A-arms and other linkages. Figure 2.11 shows some different layouts. The different layouts are used to obtain different characteristics regarding directional stiffness, restricted motions and allowable displacements. The directional stiffness is the most important design criteria to obtain desirable elasto-kinematics.
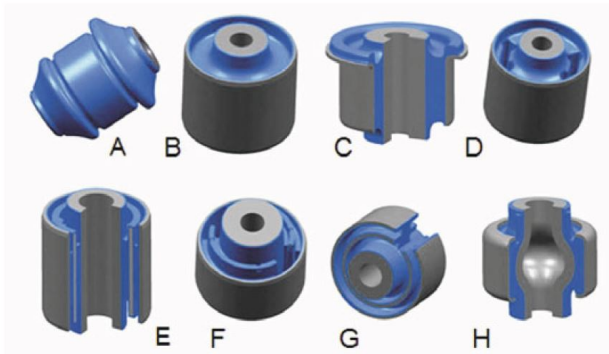
Figure 2.11: *Different bushings that are used in A-arms and other links [HE11]*

Bushings are not only used in the linkages but also in between the sub-frames and the chassis. The sub-frame is in most cases a free-formed metal frame to which all the suspension components are attached to. In this way the actual chassis manufacturing becomes less complex since it only needs to have interfaces to the sub-frame and not to all different suspension components. It also helps to improve the ride of a car since there can be used additional bushings between the sub-frame and the chassis. A selection of different sub-frame bushings is shown in Figure 2.12. The upper row shows different designs for pure rubber bushings, the bottom row shows solutions for hydraulically damped bushings. Hydraulically damped bushings are also commonly use to isolate engine mounts.
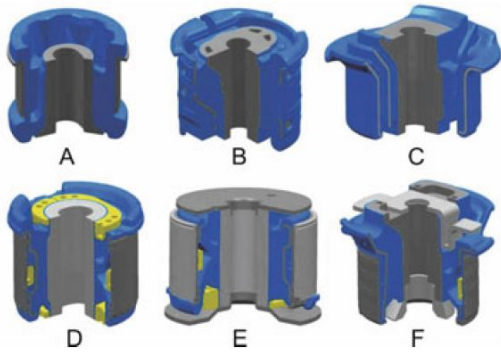
Figure 2.12: *Different bushings that are used to connect sub-frames to the chassis [HE11]*

Another type of bushing that is commonly used is the so called top mount bushing. It is located at the attachment point of the damper piston to the chassis. There are different designs of these bushings (Figure 2.13), some only transfer damper forces via the rubber, some have an extra rubber layer for the spring seat and some use the rubber combined for both.
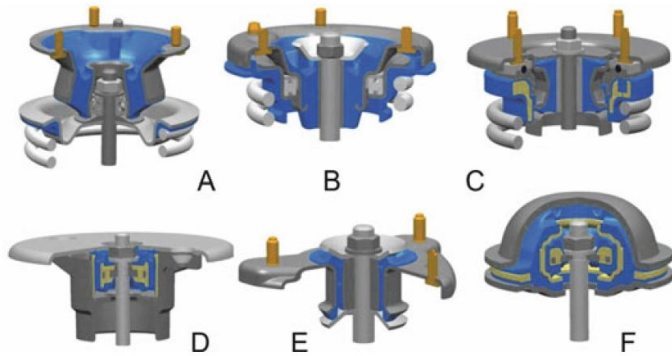
Figure 2.13: *Different bushings that are used in the strut top mount [HE11]*

2.2.3 Tires and unsprung mass

The probably most important component of a car suspension is the tire, since it is the only component that connects the vehicle to the road. In addition to this it is also one of the most complex ones when it come to simulations, because it has a highly nonlinear behavior. This behavior is mainly due to the fact that the tire consists out of rubber and is reinforced with different materials. There are however also nonlinearities when it comes to a non rolling tire. In general most of the literature is about the properties or rolling tires. Therefore it is not easy to find good information sources. Three papers were found that capture the dynamic stiffness of a non rolling tire. The first paper [PC75] is about general vibration properties of tires. An hydraulic shaker rig was used to oscillate tires and the dynamic stiffness of the tire was measured. The conclusion is that the tire acts as a stiff spring when excited at its first natural frequency. Results for Bias, Belted Bias and Radial tires can be seen in Figure 2.14.
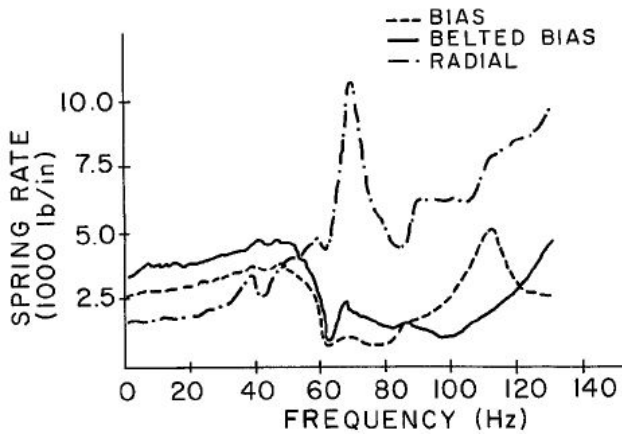
Figure 2.14: *Tire radial spring-rate over excitation frequency [PC75]*

Unfortunately the test set up is not precisely described and the study is 40 years ago. It is therefore hard to draw further conclusions from this. However, assuming that the tire was excited with a displacement input, the test shows that in the low frequency range (0-30Hz), the tire shows only a slight increase in dynamic stiffness due to increasing deformation velocity. The second paper [BCT07] is about determining tire radial stiffness and damping properties. To obtain the natural frequencies of a tire, accelerometers were placed on different positions of the tire and the tire was excited by hitting it with a hammer. The measured accelerations of the resulting decaying free oscillation of the tire was used to obtain the eigenfrequency and damping ratio of the tire. This test was done on different tires and also the normal load and therefore the static deflection was varied by adding additional weight to the tire/rim combination. Figure 2.15 displays the results for this in the plot on the left side. It shows the eigenfrequency over added mass in kilogram. It can be seen that all tires in general show an increased eigenfrequency with increased normal load. The third paper [TBS00] studied five different methods for measuring vertical stiffness of a tire. The first three methods were normal load-deflection (LD), non-rolling vertical free vibrations (NR-FV) and non-rolling equilibrium force-deflection. All of them were therefore measurements done on a non-rolling tire. The other two methods were rolling vertical free vibrations and rolling equilibrium load deflection. The results can be seen in Figure 2.15 on the right. The plot shows radial stiffness over deflection for the different measurements techniques. It becomes clear that the dynamic stiffness of a non-rolling tires seems to increase with increased deflection.
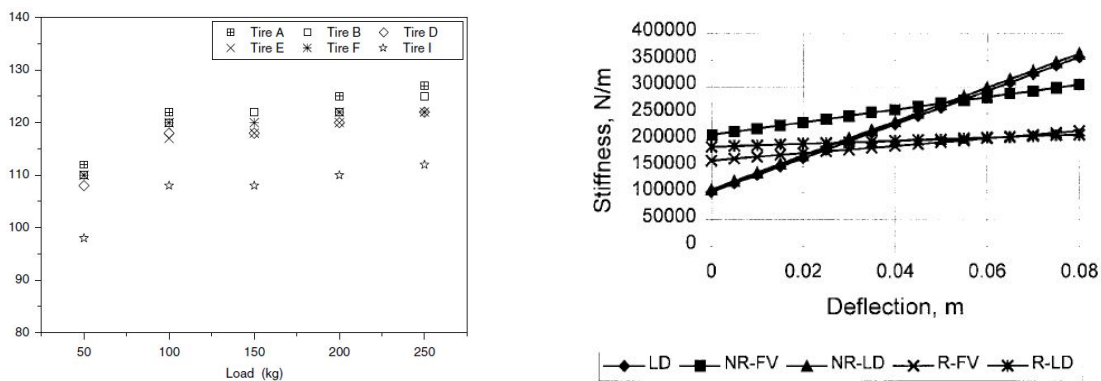
Figure 2.15: *Tire Eigenfrequency over normal load [BCT07] (right) and radial stiffness over deflection [TBS00] (left side)*

2.3 Modeling of suspension components

This section describes basic physical component behaviour and phenomenas occurring in a suspension system, i.e. it is treating dampers, bushings, tires and friction. All linkages etc. are assumed to be rigid and will not be treated in this thesis.

2.3.1 Dampers

The simplest representation of a damper is done by using a linear damping coefficient to characterise the damping-force/damper-velocity relationship. Figure 2.16 shows such a force-velocity plot of a linear damper. It can be seen that the damping coefficient c_d is constant over the whole operating range. That means it is independent of damper velocity and the same for bump and rebound damping.
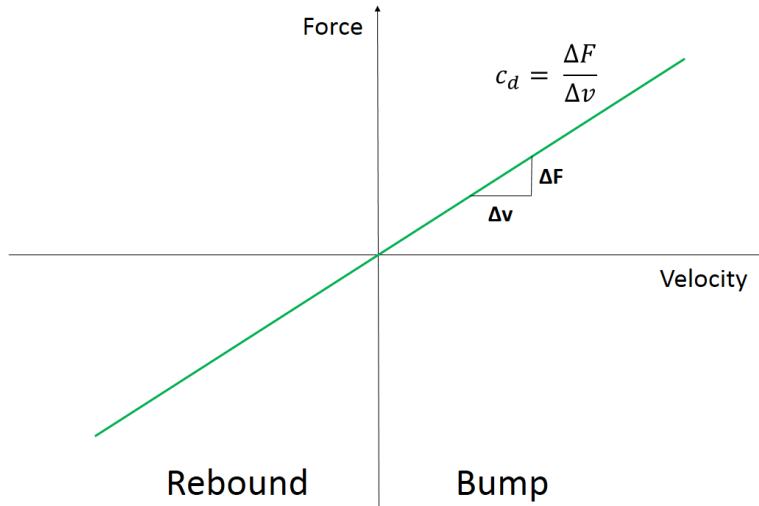
Figure 2.16: *Linear damping characteristics*

Despite the fact that this constantly linear damping behavior might be difficult to achieve in practice, it is also not desirable when it comes to ride comfort. As can be seen in Figure 2.6, below a frequency ratio of $\frac{\omega_{input}}{\omega_{eigen}} = \sqrt{2}$ damping reduces transmissibility. However, above this frequency it is increased, therefore it is desirable to have a damper which supplies high damping at low frequencies and low damping at high frequencies. One way to achieve this is to incorporate rubber bushes into the the damper mountings, which soften the effect of the damper for small amplitudes, which correspond to high frequencies. [Dix07] On top of this shock absorbers can also provide velocity dependent damping (Figure 2.17). These type of curves are mainly achieved by using spring pre-loaded valves that open up when the damping force increases and thereby generate the digressive force-velocity curves.
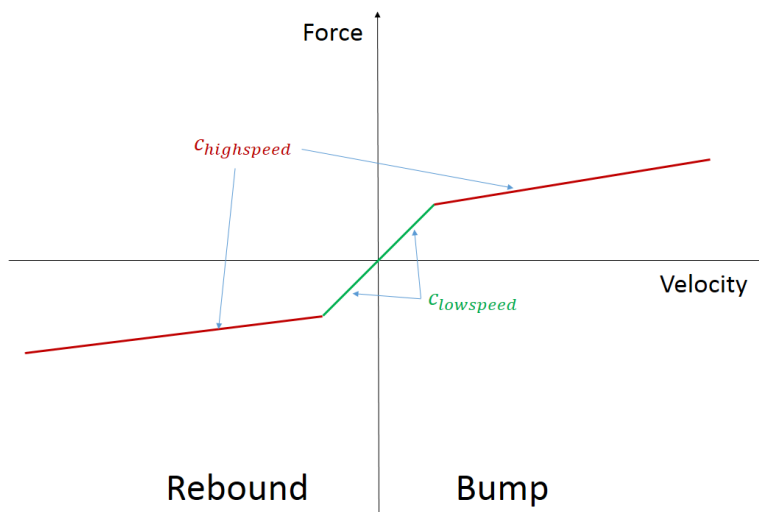
Figure 2.17: *Velocity dependent damping characteristics*

The point where the change from low speed damping ($c_{lowspeed}$) to high speed damping ($c_{highspeed}$) occurs is named the "knee" in the damper diagram. Modern dampers are also tuned in a way that they usually offer more damping in rebound than in bump, since the rebound damping needs to control the response of the "heavy" chassis to the released energy from the spring which was stored a bump input of the "light" unsprung mass. Also the position of the "knee" plays a part in the damper setup, in order to determine which movements are controlled by the high speed damping and which are controlled by the low speed damping.

All of these damper characteristics can be cover with the force-velocity relationship. However, this is sometimes not enough, this since dampers also have hysteretic and non-linear behavior which is acceleration, velocity and position dependent. Besides the asymmetric damping in bump and rebound the main source for non-linearities are friction, hysteresis due to compressibility and hysteresis due to backlash. [KM86] Also temperature has an effect on the damper characteristics. In everyday use, the increase in temperature due to energy dissipation (10W) is around 2K and can therefore usually be neglected. [Dix07] The temperature dependence should still be considered if the behavior of the system is of interests under extreme cold or hot conditions. Another factor that increases the hysteresis in the Force-Velocity diagram is the gas force. To compensate for the decrease in volume when the piston rod enters the cylinder in compression, dampers are filled with gas. This gas can compress and compensate the volume difference. To avoid cavitation of the fluid, this gas is set under pressure. The higher the pressure, the higher the spring rate of the gas force, and therefore the higher the hysteresis loop in the Force-Velocity curve. Figure 2.18 shows a representative force-velocity curve for a real damper. The shape of this curve changes if the same damper would be tested at another frequency, another position range, temperature or another peak velocity.
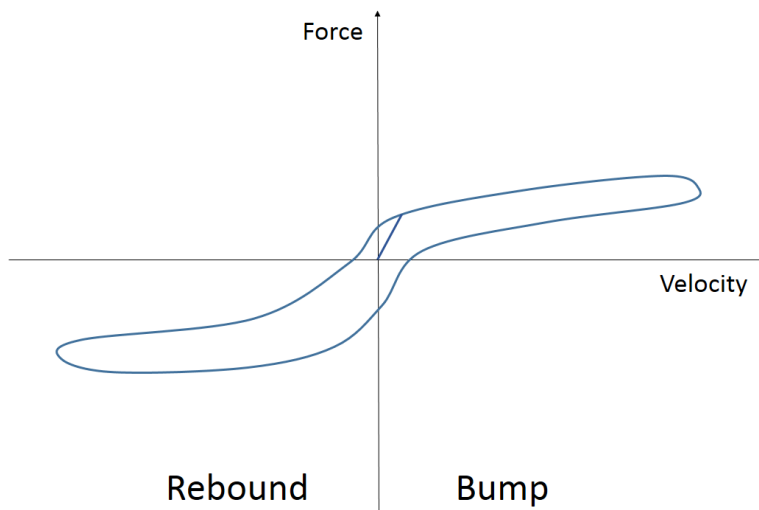
Figure 2.18: *Representation of a real force velocity trace*

It is difficult to capture the precise damper behavior in a model, but there are different approaches to build a more sophisticated damper model. In general they can be distinguished in black-box, grey-box and white-box models. Black-box models are pure empirical models which try to represent the behavior of a system without a "physical" connection to it. White-box models are purely based on the physics of the system which are assumed to be fully known. The equations are derived from mechanical principles. Grey-box models are a mixture of both, as the name already suggests. Different papers have been written about the behavior and modeling of dampers. One of them is [SL81] where dampers at high stroking frequencies where investigated. One of the main conclusions is that the increasing hysteresis loop with increasing frequency is induced by compressibility of the fluid and the existence of gas or vapor phase in the fluid during some parts in the cycle. This creates a delay in the build up of chamber pressures and therefore a phase delay between damper velocity and damper force. The paper [HG81] describes a physical damper model that takes the fluid flow through valves into account. It is shown that this can capture hysteresis loops but has room for improvement in modelling gas and vapor phases as the model shows partly a behavior that doesn't occur in real tests. Other physical models are presented in [Rey92], [LaJ96], [Bar93] and [Ben+13]. A model that captures the position dependence of a damper with a so called restoring force surface is described in [SWT92]. It basically characterises the damper with a 2D look-up table, dependent on velocity and displacement. Another paper suggests, that instead of a

velocity-displacement dependency for the force, a velocity-acceleration dependency should be used. [Duy97] The Force State Map method was also used to analyse the impact of sinusoidal, mixed and random input signals for parameter identification. [CWT95] It was concluded that random excitations yield better results with regard to the identified parameters. This conclusion is also drawn in [Kow+01]. Modeling damper behavior with the help of artificial neural networks is described in [Fas94]. It is a self learning black box model. The results show that this model can capture the amplitude dependency of a damper quiet accurately. A similar approach was used in [Bar00] where it was also extended on bushing modeling.

2.3.2 Bushings

Bushings usually consist out of a rubber compound that behaves visco-elastic. This means that it shows both viscous and elastic properties when deformed. A viscous material will exhibit a ongoing deformation over time when exposed to a constant stress. It's ability to resist this deformation is measured by the viscosity. An elastic material on the other hand will have a constant deformation for a constant stress, and regain its original shape when the load is removed. The response for different material types when exposed to a step in stress can be seen in Figure 2.19.
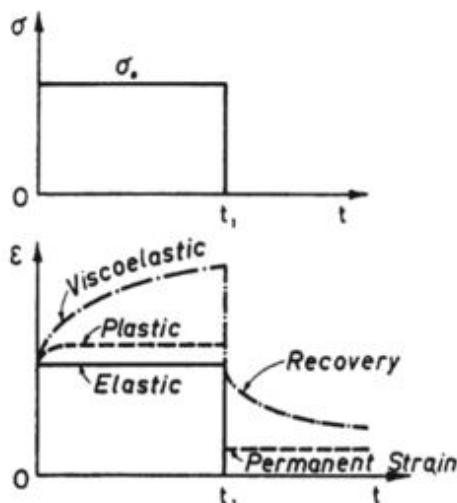
Figure 2.19: *Strain response to a constant load for different material types, [Fin89]*

Visco-elastics will also have creep and relaxation properties. Creep is described so that for a constant stress the strain will increase. Relaxation mean that for a change in strain, the stress will decrease over time. Bushings combine both the behaviours mentioned and can be hard to model because they show dependency to frequency, amplitude, pre-load, temperature and of course geometry. Due to the viscous behaviour of a bushing, energy will be lost during deformation (in contrast to a purely elastic material). This is called hysteresis and can be seen as the difference of the loading and unloading curve in a force displacement diagram, as shown in Figure 2.20. The area between the curves will be the total energy dissipated through one cycle.
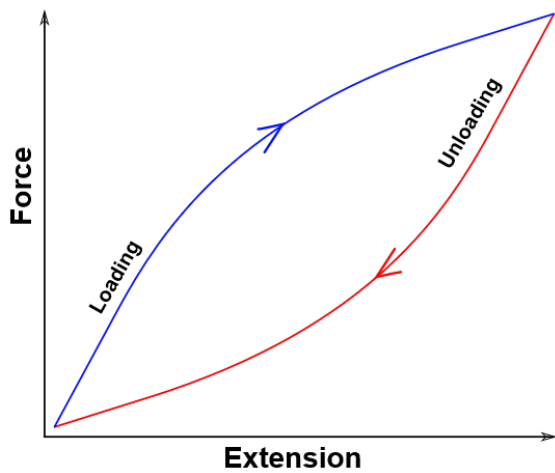
Figure 2.20: *Force deflection diagram for a viscoelastic material [com16]*

However, the behaviour as seen in Figure 2.20 is a linear behaviour, something that is often not true in automotive applications. The non-linearities can be induced either from non-linear elasticity or by frictional damping induced by the filler material in the rubber [KP03]. These non-linearities leads to a distortion of the hysteresis curve, as can be seen in Figure 2.21 (b).
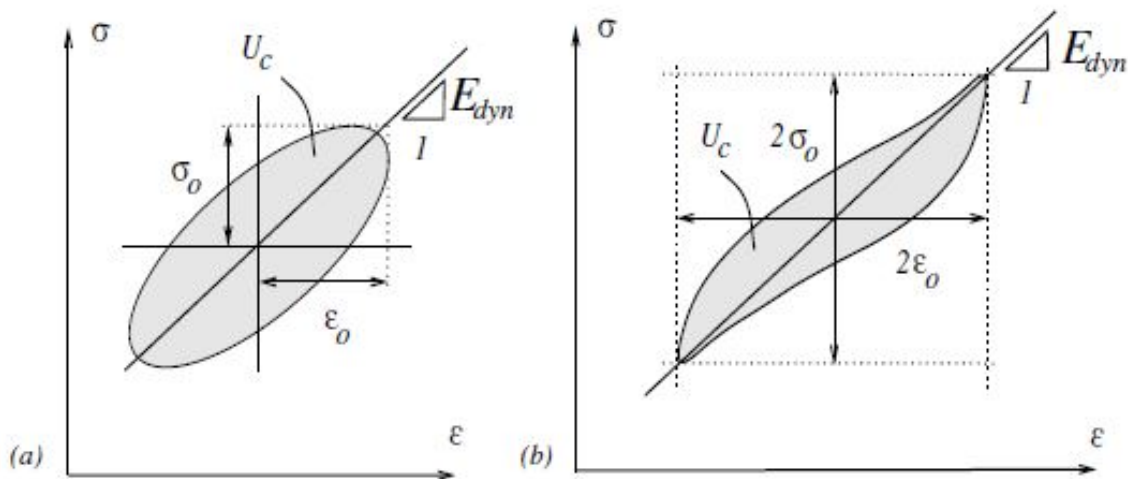
Figure 2.21: *Stress Strain diagram, linear visco-elastic (a), nonlinear visco-elastic (b), [KP03]*

One simple model for visco-elasticity is the Maxwell model as can be seen in Figure 2.22. This consists of a spring and a damper in series with each other.

Figure 2.22: *Maxwell model with damper and spring in series, [com16]*

In the Maxwell model the spring represents an elastic part and the dash pot represent the viscous component. In this model the strain will be given by $\epsilon = \epsilon_d + \epsilon_s$, and because the spring and damper are in series, the

24

stress will be equal in all parts $\sigma = \sigma_d = \sigma_s$. By time deriving the strain equation it is possible to relate the strain to the stress as in Equation 2.93

$$\dot{\epsilon} = \dot{\epsilon}_d + \dot{\epsilon}_s = \frac{\sigma}{\eta} + \frac{\dot{\sigma}}{E} \tag{2.93}$$

Here η is the coefficient of viscosity and E the elastic modulus. It can be seen in Equation 2.93 that this model will, for a constant stress σ, have a strain increasing linearly with time, i.e a constant strain rate. This also means that the stress is independent of the magnitude of the strain. This is usually not the case for a visco-elastic material, where the strain rate tends to decrease with time. The Kelvin-Voigt model takes this into account, since it consists of a spring and a damper in parallel as can be seen in Figure 2.23.
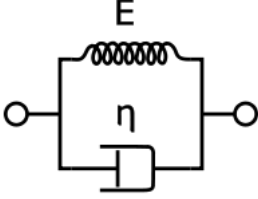
Figure 2.23: *Kelvin Voigt model, [com16]*

In this model the strain is the same for both parts $\epsilon = \epsilon_s = \epsilon_d$ and the stress is, since the elements are parallel, $\sigma = \sigma_s + \sigma_d$. Expanding the relationship between the stresses, a relationship between strain and stress can be obtained, this can be seen in Equation 2.94.

$$\sigma = \sigma_s + \sigma_d = E\epsilon + \eta\dot{\epsilon} \tag{2.94}$$

However, as can be seen in Equation 2.94 the Kelvin-Voigt model does not take the stress relaxation into account. To solve the issues with the Maxwell and Kelvin-Voigt models, a spring in parallel with the Maxwell model above can be used, as can be seen in Figure 2.24. This model is called the "standard linear solid" model, and considers both, stress relaxation and creep/recovery behaviour.
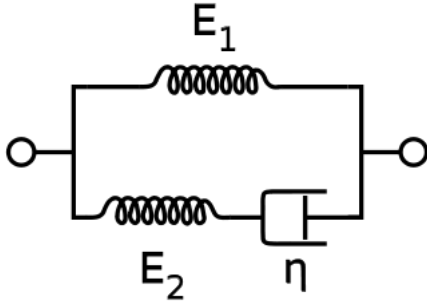
Figure 2.24: *The Standard Linear Solid model, [com16]*

Here the total stress is $\sigma = \sigma_{maxwell} + \sigma_{s1}$ and the total strain is $\epsilon = \epsilon_{maxwell} = \epsilon_{s1}$. The Maxwell subscript indicates the lower part of the diagram, i.e the spring and damper in series, and $s1$ is the top spring in parallel with the Maxwell model. By time derivating the strains and using this relation we obtain

$$\dot{\epsilon} = \dot{\epsilon}_{maxwell} = \dot{\epsilon}_{s1} \tag{2.95}$$

Where

$$\dot{\epsilon}_{maxwell} = \frac{\sigma_{maxwell}}{\eta} + \frac{\dot{\sigma}_{maxwell}}{E_2} \tag{2.96}$$

$$\dot{\epsilon}_{s1} = \frac{\dot{\sigma}_{s1}}{E_1} \tag{2.97}$$

Using Equation 2.96 and the relationship between the stresses and Equation 2.97, we obtain a relation between total stress σ and total strain ϵ in Equation 2.98

$$
\begin{aligned}
\dot{\epsilon} &= \frac{\sigma - E_1\epsilon}{\eta} + \frac{\dot{\sigma} - E_1\dot{\epsilon}}{E_2} \\
&= \frac{\frac{E_2}{\eta}(\sigma - E_1\epsilon) + \dot{\sigma}}{E_1 + E_2}
\end{aligned}
\tag{2.98}
$$

All these models are linear and do not capture the distortion as seen in Figure 2.21(b) caused by nonlinearities.

2.3.3 Tires

There are many ways to model tires and the models range from physical models (e.g. brush tire model) to semi-empirical models such as the Pacejka Magic Tire Formula. Some of the tire models models are designed to, or can be extended to capture all the dynamics of a tire, e.g. lateral, longitudinal and vertical dynamics. In this thesis only the vertical dynamics are of interest, thus a simple spring and damper in parallel could be used. This is also how the vertical characteristics are modeled in the Pacejka model in ADAMS Car (Use Mode 0). Additionally this model features a Maxwell element that can be used to capture the dynamic behavior of a non rolling tire (see Figure 2.25).
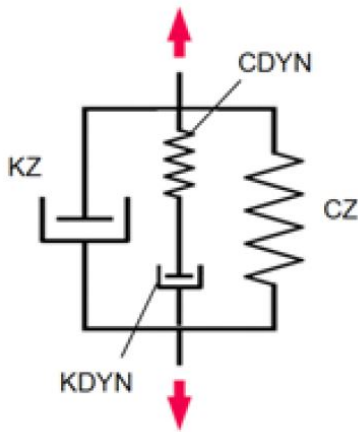
Figure 2.25: *Pacejka non rolling tire ADAMS Car*

The Pacejka model can not capture amplitude dependent effects and the effect of the additional lateral stiffness for a non rolling tire. A model that is able to capture these effects is the Ftire model (Flexible Structure Tire Model). The basic set-up of this model is a flexible belt that consists out of different belt elements, that are connected to each other with springs that determine the stiffness of the tire in different directions. Figure 2.26 shows the four main characteristics in a simplified manner.
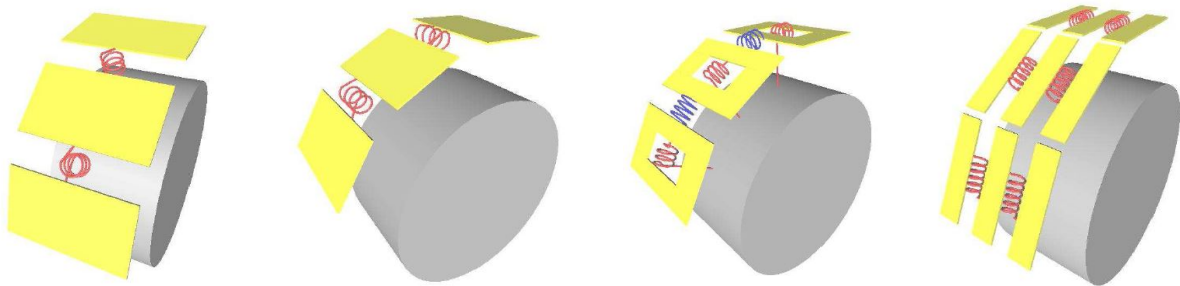
Figure 2.26: *Simplified representation of the Ftire model. Form left to right: Out of plane bending stiffness, In plane bending Stiffness, Circumferential torsion and twist stiffness, Lateral bending stiffness. [Sof14]*

Each belt element itself inherits a number of thread elements which themselves have stiffness and damping characteristics. The model is parametrized with the help of the first six eigen-modes (Figure 2.27) of the tire/rim combination and additional physical tests as stiffness, damping, friction and wear. Also other parameters as tread-pattern, inflation pressure, mass, inertia, etc. need to be specified. An advantage of this model is that it is representing the tire in a complete physical manner and the model therefore doesn't need to be change for a rolling or a non-rolling case. It should also be able to capture most of the tire non-linearities in both cases.
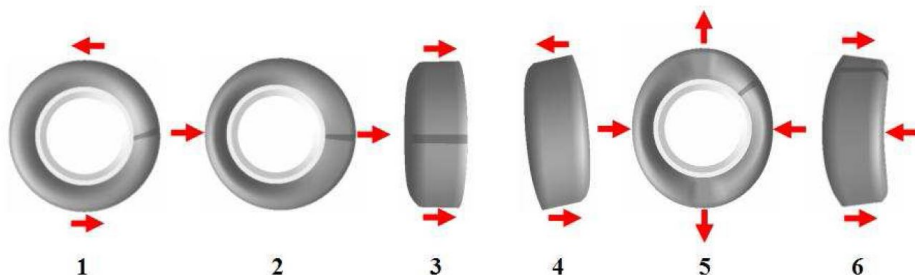
Figure 2.27: *First six tire eigen-modes[Sof14]*

2.3.4 Friction

Friction is a part of tribology, which is the science of the mechanisms of friction, lubrication and wear of interacting surfaces that are in relative motion. [Alt99]. There are different types of friction that can be categorized according to the present interaction form, see Table 2.2

Table 2.2: Different surface interactions for friction

Interaction	Friction type
Solid — Solid	dry-, lubricated friction
Solid — Fluid	skin friction
Fluid — Fluid	viscous friction
Solid deformation	internal friction

For suspension systems the Solid-Solid interaction type is predominant. Skin friction can be neglected because the influence is small compared to the dry and lubricated friction. Viscous friction is the basic principle modern shock absorbers are based on. Also hydro bushings make use of viscous friction. Internal friction occurs in any solid material under strain. Especially in elastomeric materials this plays an important role, as it results in an internal damping and creates hysteresis. [Bes+10](see also Section 2.3.2) For other materials such as metal, internal friction can be neglected as it is very small. Figure 2.28 shows a body sliding with a certain velocity over a surface. The surface-body combination has a friction coefficient μ which is assumed constant. This is the simplest form of dry friction and part of the Coulomb friction model. In this situation, the body would be decelerated to stand still by the friction force. As it is commonly known and can be verified in simple experiments, the body will stay at rest, once its velocity is zero and no other force is acting on it. Therefore the friction force needs to be zero when the velocity is zero, because otherwise the body would start to move into the opposite direction. While the body is moving, the friction force is counteracting the motion and acting in opposite direction to the velocity.
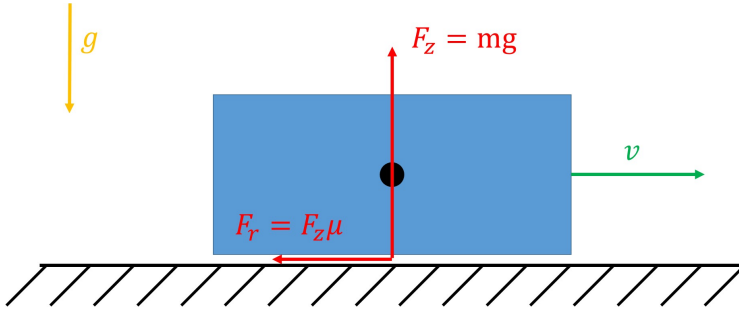
Figure 2.28: *Free body diagram for moving body with Coulomb friction*

Considering now that a external force F_{ext} is acting on the body at rest, a new problem becomes evident. When the external force is smaller than the friction force F_r the body will not move. In case an external force is acting on the body, the friction force can also not be larger than the acting force, because otherwise the body would start to move in opposite direction to the acting force. Additionally, two solid surfaces have a static μ_{st} and a dynamic friction coefficient μ_{dyn} according to the Coulomb friction model. To be able to solve these type of problems mathematically, the following set of equations is used to calculate the friction force F_r:

$$F_r = 0 \qquad\qquad if \quad v = 0 \quad \wedge \quad F_{ext} = 0 \tag{2.99}$$

$$F_r = F_{ext} \qquad\quad if \quad F_{ext} \leq F_z \mu_{st} \tag{2.100}$$

$$F_r = F_z \mu_{dyn} \qquad if \quad F_{ext} > F_z \mu_{st} \quad \vee \quad |v| > 0 \tag{2.101}$$

This set of equations can be used to solve simple problems analytically, but if they are used to solve problems numerically as in multi body simulations, problems will occur and the simulation might not converge. This is due to the fact that these equations introduce discontinuities in the equations of motion. As a consequence really small time steps and special solvers (e.g. HHT) are needed. With increasing complexity of the simulated models the solution is likely to not converge. Because of this friction is often modeled with the help of one ore more continuous functions. The same applies to lubricated friction. The only difference in terms of mathematical representation between dry and lubricate friction is, that in case of lubricated friction, the coefficient of friction decreases after stiction to a certain value and then increases with velocity because of viscous friction. This behavior is the so called Stribek effect.
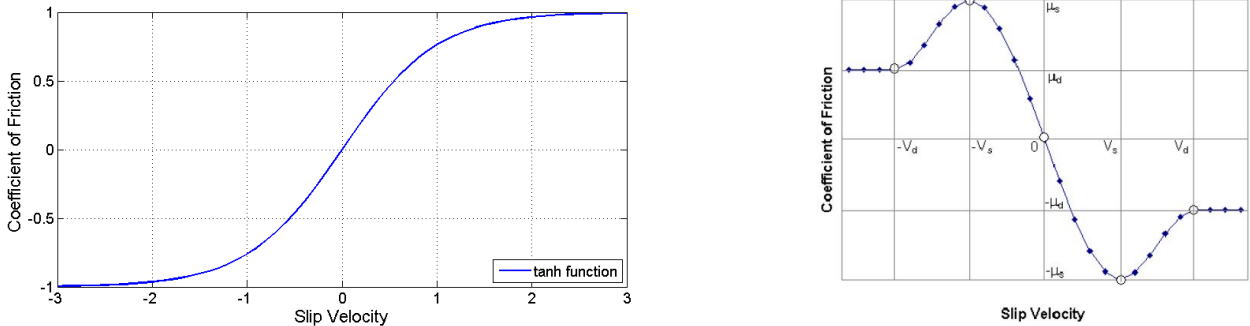
Figure 2.29: *Left:* tanh *friction model; Right: ADAMS friction model*

Figure 2.29 shows two different solutions to represent friction. On the left side is a qualitative representation of the tanh representation for friction. It is a smooth and continuous function and therefore better suited to be solved numerically. A drawback is that it can't capture the difference between static and dynamic friction. A more detailed version of this is used in ADAMS, where the curve is separated into 5 different parts. The borders are characterised by the static friction transition velocity (absolute peaks where $\mu = \mu_{st}$) and the dynamic friction transition velocity (defining the point after which $\mu = \mu_{dyn}$). This representation is a compromise between the tanh approach and Coulomb friction model. However, it might also give problems with convergence. Convergence can be improved by increasing the transition velocities as well as the gap between them. This will

28

result in a less physical system.

2.4 Physical testing of suspension systems and components

This section will shortly cover the different test machines that where used during this work. The machines are not explained in detail, as this is out of the scope for this thesis.

2.4.1 Damper tests

As already described in Chapter 2.3.1, Dampers are characterized by their force velocity curve. In order to obtain these curves, dampers are tested separately in damper test rig (Figure 2.30). These machines can oscillate the damper according to predefined input signals. Normally dampers are tested with sinusoidal input at a fixed Amplitude. The frequency is then varied in order to obtain the characteristic force-velocity curve. It is also possible to use an input signal consisting out of multiple overlaid sine waves or random input signals. More advanced testing machines also allow to test the dampers under side load and at very small amplitudes with very high frequencies.

Figure 2.30: *Damper test rig [MTS16]*

2.4.2 SPMM

A suspension parameter measurement machine (SPMM) consists of a large moving base to which the vehicle chassis is attached, the position and angles of the chassis are measured. Additionally four plates, which measure forces and moments, are placed under the wheels. These plates can be freely floating or fixed. If they are fixed then additional forces are created due to wheelbase and trackwidth change during chassis movement. At the rims there are position and angle sensors attached. With this machine it is possible to measure elasto-kinematics, compliance, spring rates, wheel rates, moments of inertia etc.

Figure 2.31: *A car placed on a SPMM*

2.4.3 4-post shaker rig

A 4-post shaker rig (SR) consists of 4 pillars which can be moved in a predefined axial movement. In a standard SR test for determining eigenfrequencies and transmissibility at Volvo Cars, one axle is excited at a time. The input signal has a fixed maximum velocity and the amplitude is changed for each sweep step in order to obtain test results from $0.5 - 30Hz$. It is a also possible to use random input signals or real road data. The SR of Volvo Cars at Hällered can be seen in Figure 2.32. By placing accelerometers on e.g. pillars, rims and body it is possible to relate these and create transfer functions for the different test conditions. Usually a frequency sweep is done and the transmissibility is presented in a bode-plot. Thus it can be seen how a certain road input affects the sprung mass or the unsprung mass or whatever is being measured.

Figure 2.32: *A car placed on a 4-post shaker rig*

3 Method

The method chapter will describe the tests performed that were needed to obtain knowledge about subsystems or entire systems. This is followed by a linear quarter car model that was used for a parameter sensitivity study. A non linear quarter car is then introduced, where the non-linearities are introduced and explained in turn. Finally a complete multi-body vehicle model (developed in Adams by Volvo) is introduced and explained. The focus lies in finding and understanding the cause of discrepancies in the current models, and understanding the level of complexity needed to accurately predict the vertical response of the suspension system. Therefore models of different complexity, ranging from linear quarter cars to full multi-body vehicles, where used. Note that two cars were used during this thesis, Car A and Car B. Car A was used for different physical tests, however some of the standard tests are also available for Car B. Further, bushing data is available for Car B, therefore the different models introduced in this section are parametrized and compared to this car.

The key areas that where identified during the pre-study are shown in Figure 3.1. Masses of components are assumed to be known accurate enough. Since the frequencies that are investigated during shaker tests are in the range of $0 - 20 Hz$, it was also assumed that eigenfrequencies of rigid parts can be neglected. Looking at a simple quarter car model, it becomes clear that the reason for different results must be somewhere in the damper modeling, bushing modeling, the friction in the system or the tire modeling. It was also concluded that it is more than likely that it will be a combination of them.
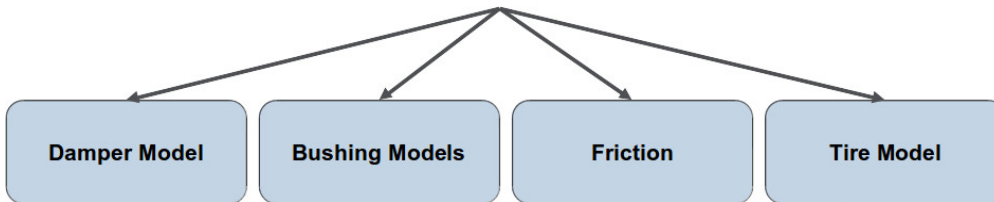
Figure 3.1: *Identified key areas for correlation work*

In Volvos Adams model that was previously used to simulate the shaker rig test, dampers where modeled with a normal Force-Velocity curve (no hysteresis), suspension bushings with linear stiffness/damping and no friction was implemented. Pacejka and FTire where used as tire models. These areas where then investigated for possibilities of refining the representation. Friction on it's own needed to be investigated. In general it was thought that it creates a stick-slip behavior in the whole system as well as it influences bushing and damper characteristics. With regard to tires represented as a spring and damper (Pacejka), it was concluded that tire damping, a frequency dependency and eventually an effective moving mass of the tire can influence the results. All this is summarized in Figure 3.2
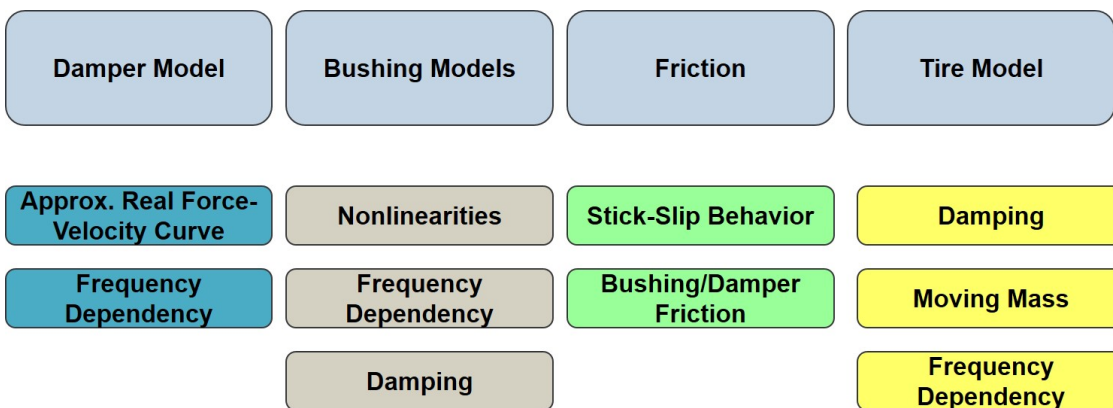
Figure 3.2: *Each key area was further divided into sub-areas*

After background knowledge was gained and the different parts where investigated from the theoretical side, a plan was made to further investigate the problem with the help of physical testing and simulations. Figure 3.3 gives an overview over the different physical tests that have been conducted. The test can be divided into three

different areas, the Shaker Rig (SR 10), the the Suspension Parameter Measurement Machine (SPMM) and the Damper Test Rig (D-Rig). On the SR 10, the standard test was conducted, as well as tests with different peak velocities of the input signal and test where maximum input acceleration was held constant instead of maximum input velocity. On the SPMM, the wheel rates, tire rates and hysteresis was measured. Dampers where measured at different amplitudes with different frequencies. Also a friction test was conducted for the dampers.
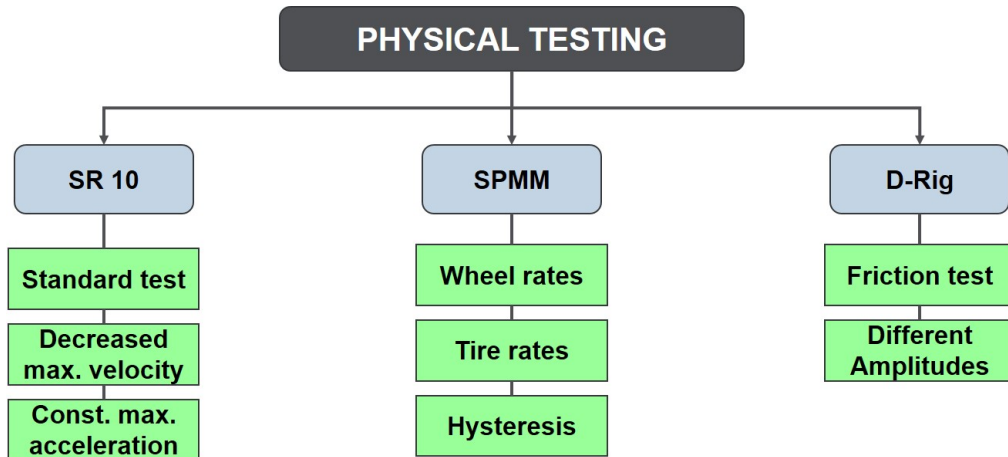
Figure 3.3: *Overview about the physical testing*

Figure 3.4 gives an overview about the different models that where used for simulations. They can also be divided into three areas, MATLAB, Dymola and Adams. In MATLAB the work was started by modeling a linear quarter car model in state space representation. Later, Dymola was used to implement non-linearities and more advance sub-models for dampers and engine bushings. Also Adams was used later to redo the shaker rig simulations, investigate the influence of tire models and see the impact of friction on a full car scale.
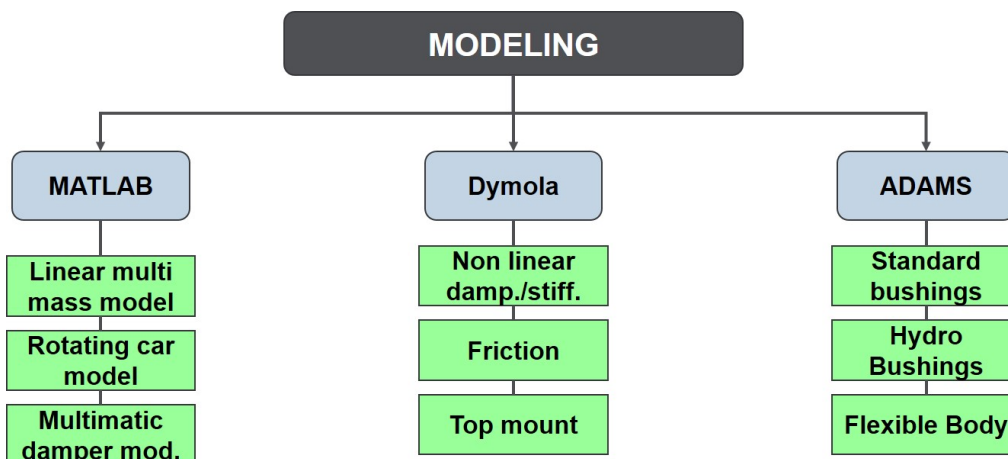
Figure 3.4: *Overview about the CAE modelling*

One of the main aims of this work was to properly investigate the correlation and not just tweak simulations in order to achieve "good" results. As a consequence parameters for the models where chosen on test data and physical reasoning rather than for best correlation. Figure 3.5 shows a small flow chart of the general process that was applied.
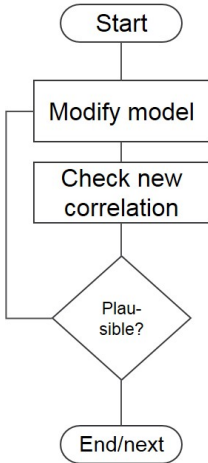
Figure 3.5: *Flow chart of the applied process*

3.1 4-post shaker rig tests

The test procedure consists of a continuous sweep from 0.5 Hz up to 30Hz, lasting for around 1200s. The input signal consists of a time vector and the four different pillars corresponding position at that time. The input signal is created with a 1000Hz resolution. The tests were performed similar for the front and the rear axle. For the front axle, this was done by exciting the front axle only, leaving the rear axle still. The accelerometers used are one axle accelerometers that where glued to the part that was being measured. The accelerometers where placed at the pillars, at the rims and at the body (in the wheel arches). Additional accelerometers where placed at the damperstrut and the damperpiston to be able to measure the damper movements. In this case they where mounted parallel to the axis of the damper.

3.1.1 Standard test - Car A

The standard shaker rig test is done with a peak input velocity of $X\frac{mm}{s}$ which is kept constant over the whole frequency range. Starting with an amplitude of Xmm at $0.5Hz$ the amplitude is decreased in steps in order to obtain a frequency sweep up to $30Hz$ without change of peak frequency. This test was performed with accelerometers only at the pillar, damperstrut and damperpiston to see the damper movement.

3.1.2 Constant peak velocity - Car A

For a linear system the input velocity will not affect the transfer function, however, since a suspension system is nonlinear, different peak velocities were tested with. Because the accelerations are smaller for a lower velocity, the forces will be smaller as well, and with a constant friction coefficient this should affect the dampertravel. Thus smaller input velocities were used to study the effect of damper sticking and dampertravel but also to study how the response changed due to other non-linearities. The tests with constant peak velocity that where conducted can be seen in 3.1

Table 3.1: Tests conducted with constant peak velocity

Peak pillar velocity mm/s	Test notes
X	Standard test. Accelerometers on pillar, damperstrut and damperpiston
60	Accelerometers on pillar, rim, body, damperstrut and damperpiston
20	Accelerometers on pillar, rim, body, damperstrut and damperpiston
5	Accelerometers on pillar, rim, body, damperstrut and damperpiston

3.1.3 Constant peak acceleration - Car A

The idea to do constant peak acceleration tests, was to keep the force acting on the suspension more constant to be able to pin point the sticking behaviour and therefore see if it could be associated with a specific acceleration of the pillar. The different tests conducted can be seen in Table 3.2

Table 3.2: Tests conducted with constant peak acceleration

Peak pillar acceleration mm/s^2	Test notes
314	Accelerometers on pillar, rim, body, damperstrut and damperpiston
157	Accelerometers on pillar, rim, body, damperstrut and damperpiston
62.8	Accelerometers on pillar, rim, body, damperstrut and damperpiston
15.7	Accelerometers on pillar, rim, body, damperstrut and damperpiston

3.2 Damper tests Car A

To characterize the dampers, one of the front dampers where tested in a damper rig. The rear dampers where not tested since the quarter car models only where parametrised for the front axle. The procedure was to measure the force and displacement/velocity at different operating points. The standard test is conducted at fixed amplitude and for seven different frequencies. Additional tests with other amplitudes where conducted as well. The different tests performed are summed up in Appendix D.

The missing values in the table are due to that the damper rig could not obtain the demanded frequency. The asterisk marked values where attempted, however due to test rig limitation the desired velocity was not obtained, this due to amplitude and frequency not reaching the demanded value. On top of this friction tests where run. They consist of one cycle with 10 mm amplitude at 0.04 Hz.

3.3 Suspension Parameter Measurement Machine (SPMM) tests Car A

Attempts to measure friction and other dynamic characteristics where made with the help of an SPMM machine. The tests performed where of vertical nature, since it is possible to measure wheel forces in relation to position of wheels and body etc. the idea was to capture as much of the static and dynamic behaviour as possible. The measurements performed are listed in Table 3.3. The two last tests where performed with altered tire pressures to see its influence on the tire stiffness.

Table 3.3: Vertical tests performed in the suspension parameter measurement machine

Test number	Description	Amplitude [mm]	Cycle time [s]
1	Vertical Bounce at 2.5 bar	72.5	300
2	Vertical Bounce at 2.5 bar	72.5	180
3	Vertical Bounce at 2.5 bar	72.5	90
4	Vertical Bounce at 2.5 bar	72.5	45
5	Vertical Bounce at 2.5 bar	22.0	10
6	Vertical Bounce at 2.5 bar	12	1
7	Vertical Bounce at 2.5 bar	3.4	0.33
8	Vertical Bounce at 2.95 bar	72.5	90
9	Vertical Bounce at 2.15 bar	72.5	90

3.4 Linear quarter car model

MATLAB was used to create a simple linear three mass model. This was due to the model simplicity, ease of parameter sweeps and speed of simulations. This model was used for a sensitivity study, where each parameter was changed and the response compared. The model can be seen in Figure 3.6. This model was judged to be

comparable with the physical test procedure, due to the fact that the rotational 1-DOF model seen in 2.1.5 closely matched the translational 1-DOF model.
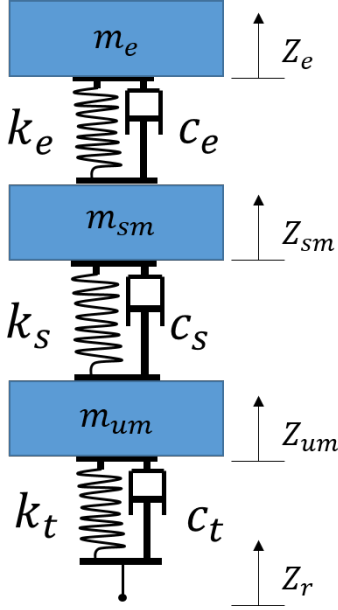
Figure 3.6: *Linear three mass model used for parameter sensitivity study*

With a free body diagram we obtain the following equations of motion for the engine, sprung mass and unsprung mass in Equation 3.1, 3.2 and 3.3 respectively.

$$k_e(Z_{sm} - Z_e) + c_e(\dot{Z}_{sm} - \dot{Z}_e) - m_e g = m_e \ddot{Z}_e \tag{3.1}$$

$$k_s(Z_{um} - Z_{sm}) + c_s(\dot{Z}_{um} - \dot{Z}_{sm}) - k_e(Z_{sm} - Z_e) - c_e(\dot{Z}_{sm} - \dot{Z}_e) - m_{sm} g = m_{sm} \ddot{Z}_{sm} \tag{3.2}$$

$$k_t(Z_r - Z_{um}) + c_t(\dot{Z}_r - \dot{Z}_{um}) - k_s(Z_{um} - Z_{sm}) - c_s(\dot{Z}_{um} - \dot{Z}_{sm}) - m_{um} g = m_{um} \ddot{Z}_{um} \tag{3.3}$$

This in matrix form can be seen in Equation 3.4.

$$
\begin{aligned}
& -\begin{bmatrix} m_e & 0 & 0 \\ 0 & m_{sm} & 0 \\ 0 & 0 & m_{um} \end{bmatrix} \begin{bmatrix} \ddot{Z}_e \\ \ddot{Z}_{sm} \\ \ddot{Z}_{um} \end{bmatrix} + \begin{bmatrix} -c_e & c_e & 0 \\ c_e & -c_s - c_e & c_s \\ 0 & c_s & -c_s - c_t \end{bmatrix} \begin{bmatrix} \dot{Z}_e \\ \dot{Z}_{sm} \\ \dot{Z}_{um} \end{bmatrix} \\
& + \begin{bmatrix} -k_e & k_e & 0 \\ k_e & -k_e - k_s & k_s \\ 0 & k_s & -k_s - k_t \end{bmatrix} \begin{bmatrix} Z_e \\ Z_{sm} \\ Z_{um} \end{bmatrix} - \begin{bmatrix} m_e \\ m_{sm} \\ m_{um} \end{bmatrix} g = -\begin{bmatrix} 0 \\ 0 \\ C_t \end{bmatrix} \dot{Z}_r - \begin{bmatrix} 0 \\ 0 \\ k_t \end{bmatrix} Z_r
\end{aligned}
\tag{3.4}
$$

Or equivalent using $\boldsymbol{Z} = [Z_e Z_{sm} Z_{um}]'$ and removing the static mass.

$$\boldsymbol{M}\ddot{\boldsymbol{Z}} + \boldsymbol{C}\dot{\boldsymbol{Z}} + \boldsymbol{K}\boldsymbol{Z} = \boldsymbol{C_t}\dot{Z}_r - \boldsymbol{K_t}Z_r \tag{3.5}$$

Here $\boldsymbol{M}$ is the mass matrix, $\boldsymbol{C}$ is the damping matrix, $\boldsymbol{K}$ the stiffness matrix and $\boldsymbol{C_t}$ and $\boldsymbol{K_t}$ are the tire damping and tire stiffness. The gravity will only effect the system with an offset, so the response will be identical regardless of g, therefore the term is removed completely. Fourier transforming this matrix form and rewriting it as in Equation 3.6 we have obtained the transfer functions for the three masses respectively.

$$\begin{bmatrix} \mathcal{F}(Z_e) \\ \mathcal{F}(Z_{sm}) \\ \mathcal{F}(Z_{um}) \end{bmatrix} \frac{1}{\mathcal{F}(Z_r)} = (\omega^2 \boldsymbol{M} + i\omega \boldsymbol{C} + \boldsymbol{K})^{-1}(-i\omega \boldsymbol{C_t} - \boldsymbol{K_t}) \tag{3.6}$$

Equation 3.6 was then used with a set of reference parameters that where obtained from the Adams model. Note that to average the left and right wheel parameters (mass, stiffness etc.), the values of the left and the right side were lumped together. In reality this is equivalent to a half car. Since the suspension acts in parallel with each other, the values are simply doubled compared to a quarter car.

Here the amplitude is calculated as in Equation 3.7 and the phase shift as in Equation 3.8.

$$\mid H_{Z_r \to Z_{sm}} \mid = \sqrt{Re^2 + Im^2} \tag{3.7}$$

$$\phi = \arctan\left(\frac{Im}{Re}\right) \tag{3.8}$$

To more accurately represent the system without using a too complex model, actual measurement data from the SPMM was partly used. The value of the spring rate K_s is the actual measured wheel rate, this means that it contains the vehicles actual spring stiffness including motion ratio, as well as parasitic stiffness from bushings. The tire rates where also obtained from the SPMM. Each of these parameters where in turn varied from 75% to 125% of its original value. Bode plots where generated where the amplitude response was calculated as in Equation 3.7 and the phase angle as in Equation 3.8. This was done for all three of the transfer functions in Equation 3.6. A parameters particular impact on the amplitude response was measured with RMSD (Root Mean Square Deviation), where the deviation was calculated with respect to the reference response. The deviation was calculated for the responses from road to unsprung mass and road to sprung mass. The result was used as a guidance to where accurate modeling was needed due to a high parameter sensitivity, i.e where a small deviation had a large impact on the amplitude response. The RMSD between the two data series was calculated as in Equation 3.9, where x_1 and x_2 refers to the two different data series between which the deviation is calculated.

$$RMSD = \sqrt{\frac{\sum_{t=1}^{N} (x_{1,t} - x_{2,t})^2}{N}} \tag{3.9}$$

3.5   Non-linear quarter car model

Dymola was used to introduce non linearities and still quickly be able to simulate and evaluate model and parameter changes. The results were post-processed in MATLAB where the transfer functions were calculated using the MATLAB function *tfestimate*. This method was validated by comparing the response obtained from the linear three mass model to the response obtained from Dymola and using the *tfestimate* function. The initial model was a simple quarter car model seen in Figure 3.6, and on from this one more complexity was added to be able to see the influence of modeling a certain component or phenomena. Certain components where also modeled in different ways, i.e three different ways of modelling the friction was used. A schematic of the final Dymola model can be seen in Figure 3.7.
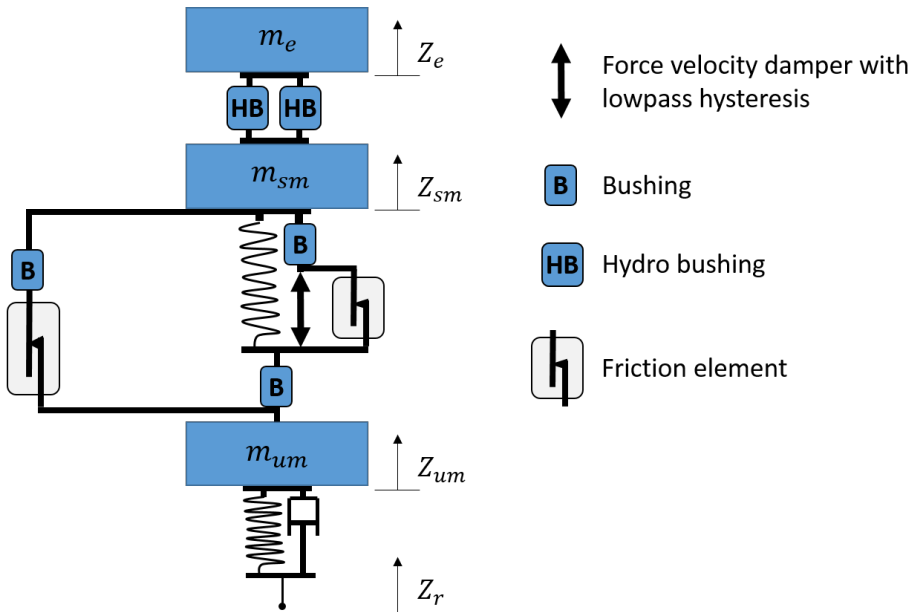
Figure 3.7: *Schematic diagram of the resulting Dymola model*

The parameters for the models were obtained to an extent by measurement data. The spring rate is simply the measured wheel rate and the tire rate is directly measured in the SPMM. Using the measured wheel rates leads to that all the parasitic stiffness from bushings etc. are included in the Dymola model. The bushing measurements available for Car B also suggested that the dynamic stiffness is close to the static stiffness. This is the reason that the wishbone bushings etc. are left out in this model. The Coulomb friction level was calculated by using SPMM measurements. Heave tests as described in Table 3.3 where conducted and the slow cycle times where used for friction estimation. Here a slow cycle time is needed so that the damping force becomes minimal. The measured wheel forces were plotted against the wheel displacement (seen in Figure 4.1). For a frictionless system one single trace is expected, however the friction adds a hysteresis loop, where the friction value was calculated as the difference in force (vertical height of the loop) divided by two. The friction force in parallel with unsprung and sprung mass is to represent the friction force occurring in the joints in the knuckle. If sticking occurs in the knuckle the suspension system will be locked. However relative movement will occur due to the vertical deflection of the inner bushings in the wishbones. Thus a bushing is put in series with the friction element to represent the equivalent vertical stiffness of the inner wishbone bushings. Note that this model was parametrized and compared with Car B.

3.5.1 Non-linear quarter car model - Velocity dependent damping

The Dymola model started out as the linear model in Figure 3.6, but with nonlinear damping between the unsprung and sprung mass. Since the Dymola model is a purely translating one dimensional model, the motion ratio between wheeltravel and dampertravel will be equal to one. This is not the case for the real vehicle, thus the damper curves generated from measurement data needs to be scaled to account for the motion ratio that exists in the real vehicle. This is done by multiplying the force column with the motion ratio and divide the velocity column with the motion ratio, in accordance to Equation 2.91 and 2.92 in the theory chapter.

The force velocity model built in Dymola consists out of a force element that was controlled with a simple look-up table. The velocity over the force element was measured and the relative velocity was used as an input to a look-up table. There, from the force velocity diagram, the corresponding force was output into the force element. A schematic can be seen in Figure 3.8
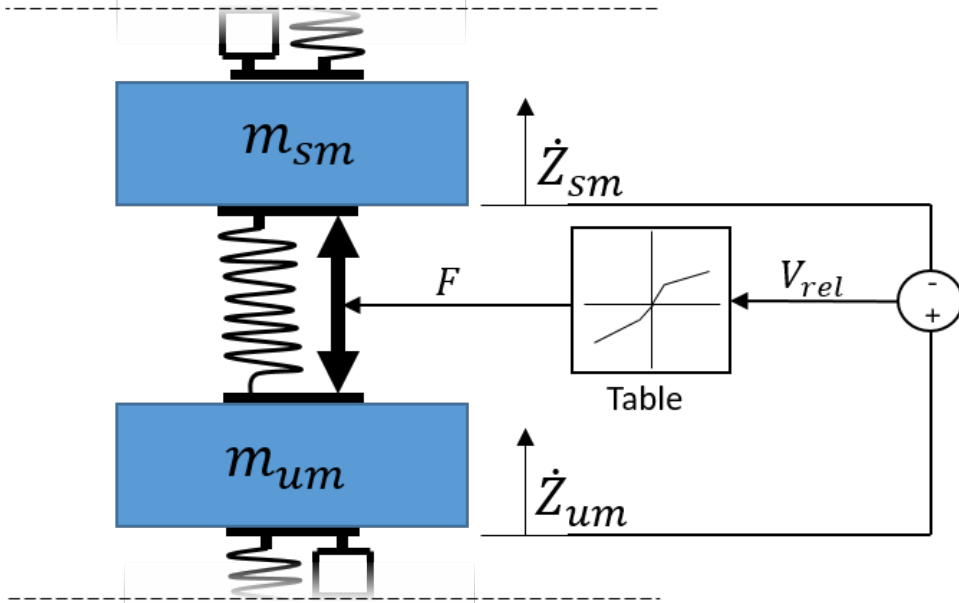
Figure 3.8: *Schematic of a look up table based force velocity damper model implemented in a quarter car model.*

Note that here rebound is defined negative in both velocity and force. Thus positive force is in the direction of the arrows in the force element seen in Figure 3.8. This model was parametrised with force velocity curves for the Car B dampers that where already available.

3.5.2 Non-linear quarter car model - Hydroenginemount

Since the engine mounts need to both absorb vibrations and both be "stiff" to improve driveability they act differently than the other bushings. Thus the models mentioned in Theory were not considered good enough for hydro bushing modeling. This because they show a strong amplitude dependency, for larger amplitudes the dynamic stiffness increases after a certain frequency, something the linear models mentioned above cannot handle. A hydro bushing model containing a non linear spring in parallel with a hydraulic chamber was implemented.

3.5.3 Non-linear quarter car model - Topmount and lower damper bushing

The topmount was modeled as a linear spring and damper in parallel, which was placed in series with the damper and the sprung mass. At the same time the lower bushing that connects the lower part of the damper strut to the wishbone was modeled, however this bushing only exists on the Car B and not in Car A with McPherson suspension. These bushings where only modeled in the axial direction. The topmount has a quite constant dynamic stiffness in the lower frequencies ($< 30Hz$) with a linearly increasing phase shift. The measurement data also suggested, that in the lower frequencies there was no significant amplitude dependence. Therefore a linear model is enough to capture this bushings dynamic stiffness behaviour in the axial direction. The problem however is that the phase shift will start at zero for zero hertz and then increase linearly.

By doing a free body diagram and Fourier transforming the equations of motion for the bushing models mentioned in the theory (Section 2.3.2), we can obtain the transfer functions between the input displacement and the output force in the frequency domain. Representing these transfer functions in Bode plot we obtain the gain which in this case is equivalent to the dynamic stiffness. The transfer function for the Kelvin Voigt model becomes as in Equation 3.17. However, instead of using strain and stress as in the theory section, we use displacement and force. A free body diagram of the Maxwell model (as seen in Figure 2.22) gives the following equations

$$F = c(\dot{Z}_1 - \dot{Z}_2) \tag{3.10}$$
$$F = kZ_2 \tag{3.11}$$

By Fourier transforming both equations we obtain

$$\mathcal{F}(F) = iwc\mathcal{F}(Z_1) - iwc\mathcal{F}(Z_2) \tag{3.12}$$

$$\mathcal{F}(F) = k\mathcal{F}(Z_2) \tag{3.13}$$

Rewriting 3.13 and inserting $\mathcal{F}(Z_2)$ in Equation 3.12 and rewrite this equation on output/input form we obtain the transfer function for the Maxwell material as in Equation 3.14.

$$H_{Z \to F} = \frac{\mathcal{F}(F)}{\mathcal{F}(Z)} = \frac{kjwc}{k + jwc} \tag{3.14}$$

For the Kelvin Voigt model seen in Figure 2.23, the free body diagram yields Equation 3.15

$$F = Zk + \dot{Z}c \tag{3.15}$$

By Fourier transforming this we obtain

$$\mathcal{F}(F) = \mathcal{F}(Z)k + iwc\mathcal{F}(Z) \tag{3.16}$$

And writing this on output/input form we obtain the transfer function for the Kelvin Voigt model as in Equation 3.17.

$$H_{Z \to F} = \frac{\mathcal{F}(F)}{\mathcal{F}(Z)} = k + jwc \tag{3.17}$$

And for the generalized Maxwell with one element

$$H_{Z \to F} = \frac{\mathcal{F}(F)}{\mathcal{F}(Z)} = k_0 + \frac{kjwc}{k + jwc} \tag{3.18}$$

Where k_0 is the stiffness of the spring in parallel with the Maxwell part. In Figure 3.9 the gain and phase for the three different transfer functions are presented. Here with the parameters $k = 200$, $k_0 = 200$ and $c = 1$.
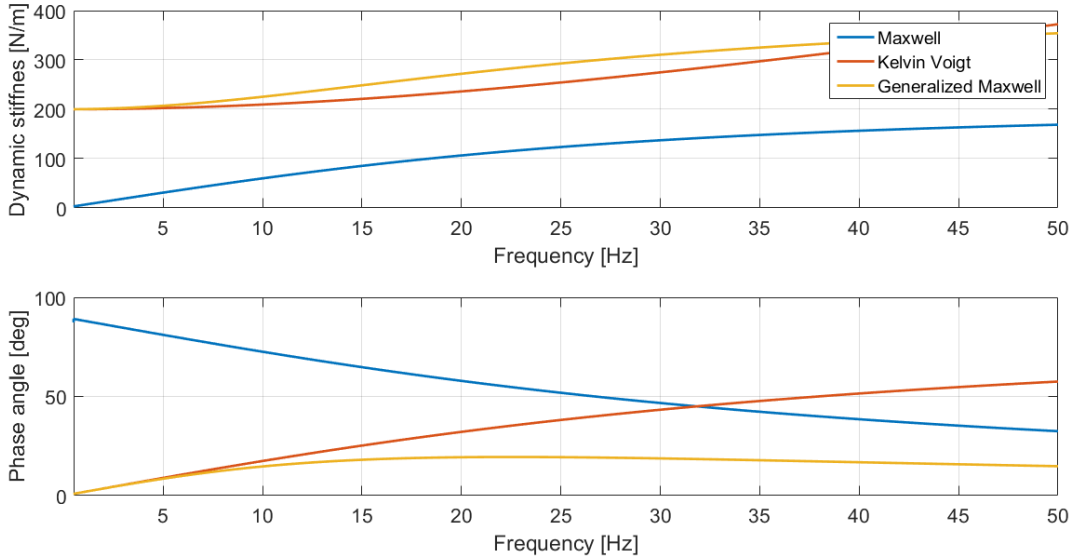
Figure 3.9: *The response and phase for the three different transfer functions mentioned*

It can be seen that the Maxwell models dynamic stiffness starts at zero and the phase angle at $90°$, as the frequency goes up the dynamic stiffness approaches the value of k and the phase approaches $0°$. However in the Kelvin Voigt model the parallel damper adds a phase delay and additional dynamic stiffness as the frequency goes up, thus the phase delay will approach $90°$ and the stiffness will continue to rise with frequency. With the

generalized Maxwell model it is possible to have both, a constant (or shaped) stiffness and phase delay over a wide frequency range, which is dependent on how many parallel Maxwell elements there are in parallel with the spring k_0. The transfer function for the general form of the Maxwell model with N elements can be seen in Equation 3.19

$$H_{Z \to F} = \frac{\mathcal{F}(F)}{\mathcal{F}(Z)} = k_0 + \sum_{j=1}^{N} \frac{k_j i w c_j}{k_j + i w c_j} \tag{3.19}$$

It was concluded that a generalized Maxwell element with three elements was to be used for the top mount. This was deemed to be enough to keep a somewhat constant phase shift and constant dynamic stiffness over the frequency range of interest. When introducing the topmount and lower damper-mount the spring stiffness was increased so that the wheel rate was held the same with and without bushings.

3.5.4 Non-linear quarter car model - Damper hysteresis

Since a force velocity representation of a damper only captures what happens in the middle point of the oscillation, which is the force obtained at peak velocity, only a small part of the damper behaviour is caught. This can be seen in Figure 3.10 where a force velocity diagram is fitted to two sets of measurements in the low speed region. Note that the offset from zero in the measurement data is due to the gas force in the damper.
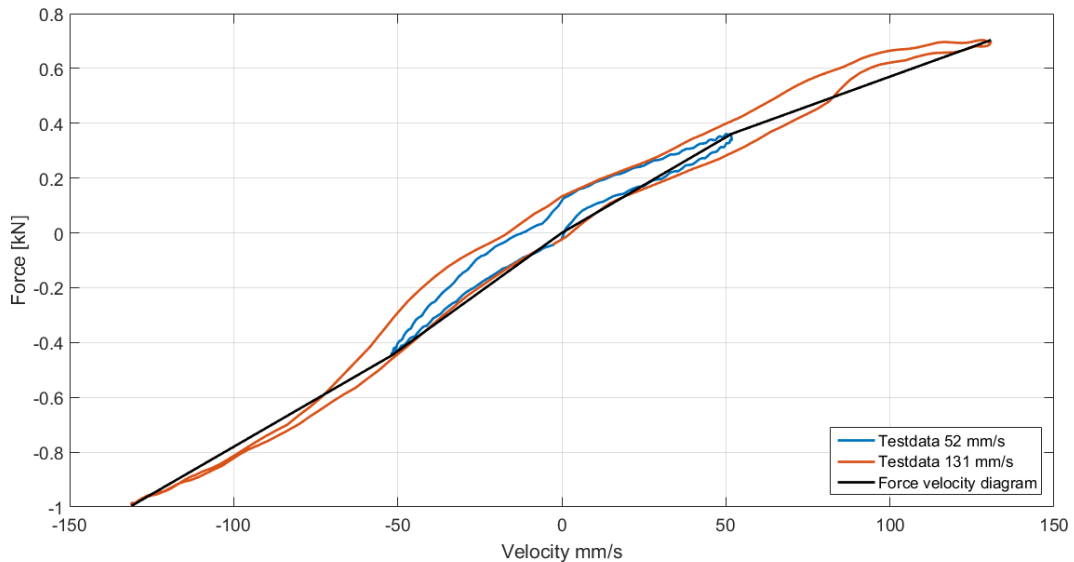
Figure 3.10: *Example of the simplifications made in a force velocity diagram*

With a force velocity representation the force will always be zero at zero velocity, something that is not necessarily true as can be seen in Figure 3.10. It is also impossible to capture the hysteresis loop with a force velocity diagram, something that is created by the time delay between the velocity and force. This phenomena creates a hysteresis loop which shape varies with the dampers operating conditions. It was seen in the measurement data that the delay was mainly frequency dependent, with a longer delay at lower frequencies and a shorter delay at higher frequencies. Therefore a second order Butterworth low-pass filter with a variable cut-off frequency was used. The cutoff frequency, f_c, was determined by Equation 3.20, where $w = 2\pi f$ is the angular velocity input, k a constant scale factor and o a constant offset.

$$f_c = (w + o)k \tag{3.20}$$

In Dymola a Butterworth filter already existed, this was modified to accommodate an extra input for the variable cutoff frequency. The higher the frequency the higher the cut off frequency needed. By lowering the cutoff frequency a larger time delay between velocity and force is created. A damper rig was constructed in Dymola that imitated the test procedure. A displacement element, connected to a sinusoidal input, excited the

damper under the same conditions as in the actual damper tests, i.e the same amplitude over seven frequencies. The damper velocity was then input into the the Butterworth filter together with the excitation frequency and filtered accordingly. The output from the filter is the time delayed damper velocity, which is then input in the force velocity table, before being input in the force element.

The low pass filter was parametrised to fit the hysteresis from the damper data obtained from the measurements mentioned above. Since the data was processed it was not possible to obtain the time series of the data, therefore it was parametrised visually to match the size of the hysteresis loop in the force velocity trace. Since only the Car A dampers where physically tested, the hysteresis behaviour was assumed to be similar in the Car B damper, thus the same filtering properties where used for Car A and Car B.

3.5.5 Non-linear quarter car model - tanh friction

A continuous friction model consisting of the tanh function was implemented to model Coulomb friction, this was due to simplicity and for fast simulations. To faster build up the full friction a factor of 100 was used for the relative velocity, this leads to the response as seen in Figure 3.11. The output from the tanh function was then multiplied with the desired Coulomb friction value and connected to a Dymola force element. The drawback with this model lies in the transition phases where the velocity is low. Since the function (and thus the friction) is zero at zero velocity, there will be no modeling of sticking behaviour or the transition phase.
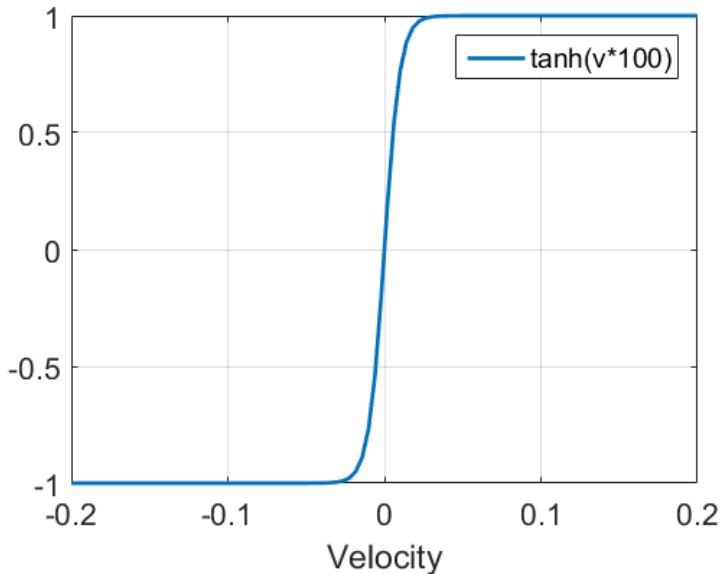
Figure 3.11: *Coulomb friction as a function of relative velocity using tanh*

3.5.6 Non-linear quarter car model - Friction by hybrid modeling

Hybrid modeling is described in [OEM99] as models that in a time instant become a mix of a continuous and discreet set of equations. This is used to be able to model the friction force in the sticking phase, because the friction force is a function of the relative velocity when sliding occurs, but not during the sticking phase. Here the friction force is instead equal to the exerted force, until the exerted force becomes larger than the static friction force and sliding starts again (and thus friction force becomes a function of velocity again). This is modeled by introducing a "mode" which simply is an integer that translates into whether the part is sliding forward, backward or if it is stuck. Similarly the Booleans $Startforward$ and $Startbackward$ are introduced to switch between set of equations that needs to be solved (i.e for the transition between sticking and moving). Note that the bold symbols are Dymola commands, where $\boldsymbol{pre}$ is the previous value $(n-1)$.

$$Startforward = \boldsymbol{pre}(mode) == Stuck \; \boldsymbol{and} \; s_a > 1 \tag{3.21}$$

$$Startbackward = \boldsymbol{pre}(mode) == Stuck \; \boldsymbol{and} \; s_a < -1 \tag{3.22}$$

$$a_{rel} = \textbf{\textit{if}} \; \textbf{pre}(mode) == Forward \; \textbf{\textit{or}} \; Start forward \; \textbf{\textit{then}} \; s_a - 1 \; \textbf{\textit{else}} \tag{3.23}$$

$$\textbf{\textit{if}} \; \textbf{pre}(mode) == Backward \; \textbf{\textit{or}} \; Startbackward \; \textbf{\textit{then}} \; s_a + 1 \; \textbf{\textit{else}} \; 0 \tag{3.24}$$

$$f = \textbf{\textit{if}} \; \textbf{pre}(mode) == Forward \; \textbf{\textit{or}} \; Start forward \; \textbf{\textit{then}} \; f_0 \; \textbf{\textit{else}} \tag{3.25}$$

$$\textbf{\textit{if}} \; \textbf{pre}(mode) == Backward \; \textbf{\textit{or}} \; Startbackward \; \textbf{\textit{then}} \; -f_0 \; \textbf{\textit{else}} \; f_0 * s_a \tag{3.26}$$

Where $mode$ is determined by

$$mode = \textbf{\textit{if}} \; (\textbf{pre}(mode) == Forward \; \textbf{\textit{or}} \; Start forward) \; \textbf{\textit{and}} \; v_{rel} > 0 \; \textbf{\textit{then}} \; Forward \; \textbf{\textit{else}} \tag{3.27}$$

$$\textbf{\textit{if}} \; (\textbf{pre}(mode) == Backward \; \textbf{\textit{or}} \; Startbackward) \; \textbf{\textit{and}} \; v_{rel} < 0 \; \textbf{\textit{then}} \; Backward \; \textbf{\textit{else}} \; Stuck \tag{3.28}$$

This means that if $\textbf{pre}(mode) == Stuck$ (i.e change of direction) then $a_{rel} = 0$ until the exerting force f exceeds the Coulomb friction force level f_0, when this happens the curve parameter s_a becomes larger than one and the part will start forward and switch back to $f = f_0$, i.e applying the full Coulomb friction at the flange. This method will thus switch between calculating the force equilibrium when keeping the relative acceleration zero, to comparing the acceleration and applying the force f_0.

This method for friction modeling is already implemented in Dymola in the form of a sliding mass, however there the friction force is between the mass and fixed ground. Therefore the element was modified with an friction surface velocity input, so that the friction force could be calculated in relation to other elements than fixed ground. An attempt to implement the friction method above with an element with a variable flange length was made, however since it did not work reliable it was not used. The consequence is that this method was only used as a friction element in parallel with the damper, not in parallel with the unsprung and sprung mass. For more about this method see [OEM99] and the Dymola documentation.

3.5.7 Non-linear quarter car model - Lund Grenoble Friction

A friction model called Lund Grenoble was implemented as a Dymola model. This method models the friction phenomena as bristles in contact, where a differential equation determines the deflection of the bristles, which in turn determines the friction force. The implementation was based on the paper ''Modeling Friction in Modelica with the Lund-Grenoble Friction Model'' [AO02]. The average bristle deflection is denoted z and the bristle deflection velocity $\dot{z}$ is written as

$$\dot{z} = v_{rel} - |v_{rel}| \frac{z}{g} \tag{3.29}$$

Where the function g relates the relative surface velocity (v_{rel}) to the bristle deflection.

$$g = \frac{1}{\sigma_0}(\mu_c + (\mu_s - \mu_c)e^{(-\frac{v_{rel}}{vs})^2}) \tag{3.30}$$

Here μ_c is the Coulomb friction level, μ_s is the static friction level and μ_v is the dynamic friction level. v_s is the Stribeck velocity which describes the friction force in relation to the relative velocity in a lubricated system. The friction force f is then calculated as in Equation 3.31.

$$f = \sigma_0 z + \sigma_1 \dot{z} + \mu_v v_{rel} \tag{3.31}$$

Where σ_0 is the stiffness of the bristles and σ_1 is the bristle damping. To further improve the the reliability and accuracy of solving the friction model the auxiliary Boolean Equation 3.5.7 was introduced to trigger an event at sign change of the velocity as suggested by [AO02].

$$\dot{z}_{change} = \begin{cases} true & \text{if } \dot{z} < 0 \\ false & \text{otherwise} \end{cases}$$

This is to avoid problems around the brake away force when using solvers with variable step size. This code was implemented in a Dymola model where the flange interaction was made by extending the model to the predefined partial model called ''PartialCompliant'' for the connecting flange interfaces.

3.6 Full car multi-body model

Adams is one of the vehicle dynamics simulation tools used by the Volvo Car Company. It is a full multi-body simulation environment with the capability of creating and solving very complex models in great detail. However, the more detail that is added to the model, the longer time it takes to perform simulations with it. Especially in comparison to the quarter car model in Dymola, the simulations in Adams are taking 10 to 1000 times longer depending on both model complexities. The advantage is that it is possible to look for example at force that are acting at specific sub-parts as dampers, which makes it for example possible to get an estimation for the bending moment and side force acting in the damper. Also specific deflections, as for example in bushings, can be evaluated and then used to decide which bushings may need to be modelled in greater detail. During this thesis work, the already existing model of Car B was used and modified. Main focus was the implementation of friction and the influence of the tire model. It was also investigated if a flexible body chassis could be used in the shaker rig simulations. The shaker rig simulations are done with the help of an Volvo specific ADAMS environment which features and self developed shaker rig model. It can be used and controlled in the same way as the real test rig. All simulations where done with discreet test procedure. According to Volvo the test procedure itself has no influence on the simulation results, as they have done simulations with both setups. The continuous setup was therefore not used. Post-processing of the results was done with an already existing MATLAB routine that calculated the transfer functions and filled an Excel template with the data to generate plots. During the work with the Adams model it became obvious that there were unexpected oscillations for the results of the transmissibility of road to rim. Since the results for the transmissibility road to body did not show any oscillations at all, and an analysis of the simulation results with the Adams post processor also couldn't show anything unusual, it was suspected that it was an error that was generated by an sensor in Adams that was used to calculate the transfer function. Further investigation yielded that there where spikes and oscillations in the sensors on the wheel assembly which could not be explained. These sensors where then replace by new defined sensors which reduced these oscillations significantly. For that reason some of the simulation data for the unsprung mass of simulations with the Ftire model can't be used. The rest of the results however doesn't seem to be effected.

3.6.1 Initial Model

The Car B model which was developed by the CAE department of Volvo is, as the real car, based on the SPA platform which is also used for the XC90 and V90. The sub-frame as well as the suspension control arms and uprights are modelled as flexible bodies. Suspension bushings are implemented and feature linear stiffness and damping characteristics. The engine mount bushings are modelled in greater detail with the help of the PIANO bushing model. Figure 3.12 shows the graphical representation of the model in ADAMS car. This model was used to repeat the already conducted Shaker Rig simulations and investigate the influence of the solvers GStiff and HHT on the results.
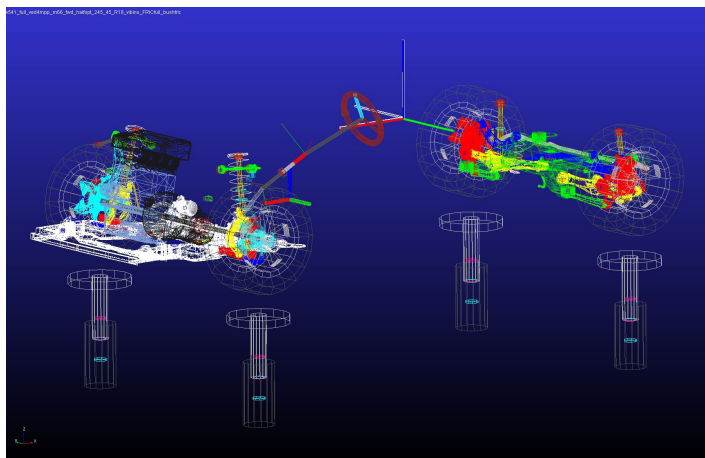

Figure 3.12: *Picture of the ADAMS model of Car B*

3.6.2 Stick-Slip Friction

After the initial simulations had been done, friction was added to the model. At the beginning, this was only done at the front axle in the the cylindrical joint of the damper. It is possible to use a pre-load to generate a constant static and dynamic friction. Reaction forces and moments can also be taken into account. The values for initial overlap ($140mm$) and the behavior of the overlap (*increase*) where taken from a previous investigation of Volvo on damper friction. The friction coefficient where kept at 0.5 static and 0.3 dynamic. These values correspond to the general assumption for steel on steel contact. Even though that might not be true, especially in the damper, it was decided to be kept like this as no other data could be obtained. Figure 3.13 shows the Adams configuration interface for friction in a cylindrical joint.
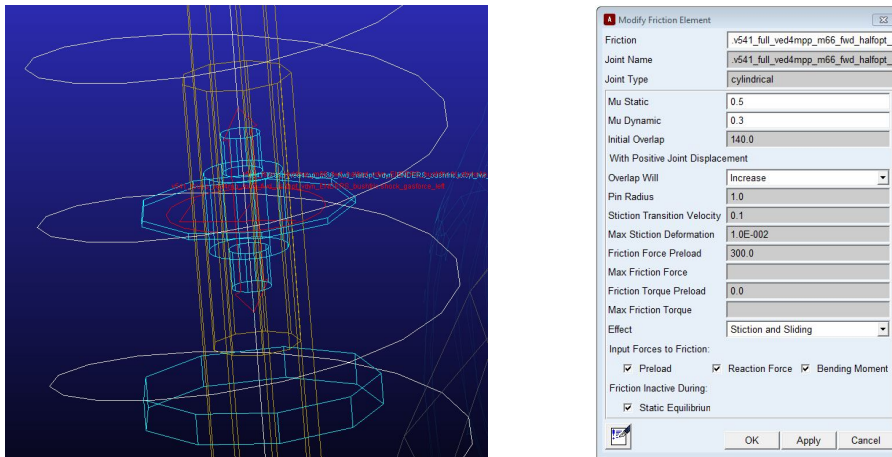
Figure 3.13: *Friction implementation in the damper*

With the friction implemented at the front axle different simulations where done. First, data from the SPMM test of Car A was analysed. Although it was not possible to exactly determine the static or dynamic friction force, it could be conclude that it will be around $50N$ to 150 of friction force at the wheel. More information about the SPMM test results can be found in Section 4.1. As a starting value $200N$ of static friction force was used in the damper and $120N$ of dynamic friction force. The dynamic force was a result of aforementioned friction coefficients for a pre-load of $400N$. It should be noted that this corresponds to $126N$ static friction force and $76N$ of dynamic friction force at the wheel, taking a motion ratio of 0.63 into account. The friction of the Car A and the Car B will be different, therefore this was chosen as a reasonable starting point and varies to investigate the influence. It was also investigated how the results change if only reaction force and torque are used without pre-load. The next step was to implement the friction also at the rear axle in the damper joint.

Figure 3.14: *Friction implementation in the ball joints*

After simulations where conducted with friction at the rear axle, friction was added in all ball joints at the front and rear axle. This was done because it was concluded that it would make a difference which joints remains in stiction. 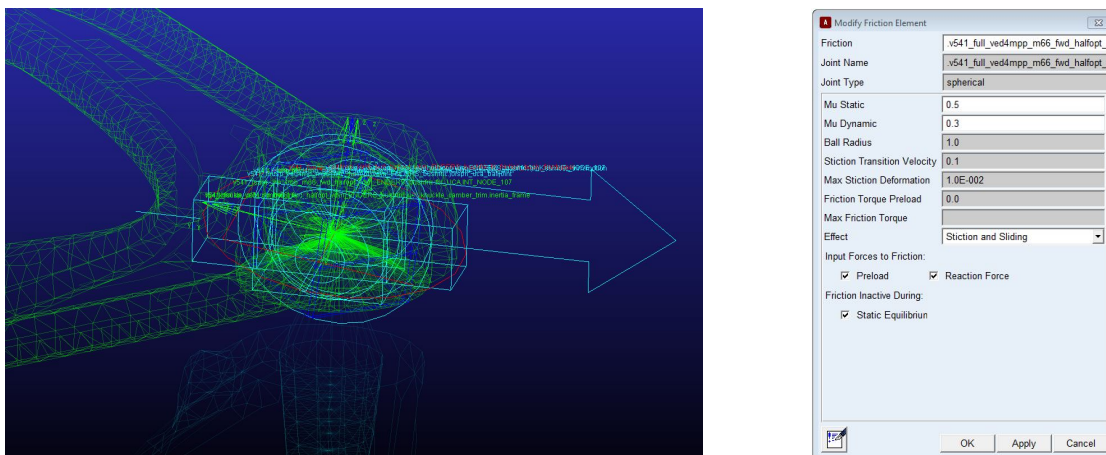If the damper is sticking and the ball joints can move, the "spring" of the chassis is the main suspension spring together with the damper top mount in parallel. If one of the ball joints locks up and the damper can move, the effective "spring" of the chassis will be all suspension bushings excluding the top mount. If both, the damper and a ball joint lock, then the effective "spring" will be all suspension bushings and the damper top mount in parallel. For all ball joints no pre-load was used and instead only reaction forces/moments with the friction coefficients of 0.5 static and 0.3 dynamic. The reasoning is the same as for the damper joint, the only difference is that this assumption is likely to be closer to reality than in case for the damper.

3.6.3 Different Tire Models

Also the two existing tire models for vertical vibration insulation where used and evaluated. The Pacejka model has the advantage of a faster computation time. The disadvantage of it comes with its simplicity. As described in Section 2.3.3, the Pacejka model for vertical dynamics (Use Mode 0) is in general only a simple spring and damper. Therefore it is less accurate compared to the Ftire model. Especially the capability of capturing frequency dependent behavior and characteristics of an non-rolling tire were deemed to be important for this type of simulations. To investigate the influence, simulations where done and compared where only the tire model was changed. Also the dynamic part of the Pacejka model (Maxwell element in parallel to the spring and damper) was used and analysed.

3.6.4 Flexible Body Chassis

Another thing that was taken into consideration was the possibility that the stiffness of the chassis might influence the shaker rig test. As stated earlier, the existing Adams model for shaker rig simulations has flexible parts for most of the suspension components. The chassis of the car however was rigid. For SPMM test in Adams there is also a model with a flexible chassis. The idea was to use the flexible chassis and implement it in a new assembly for shaker rig simulations. This was possible after the communicators for the SPMM attachments where deleted as they attached to ground in the assembly with a shaker rig. A problem was that the mass of the flexible chassis assembly was not correct any more. The flexible chassis sub-assembly only contains the Modal Neutral File (MNF) of the car body, but no interior and other parts. Therefore the mass was $680kg$ too low. Due to time constraints it was not possible to further develop the flexible body assembly. Instead an additional mass of the missing weight was attached to the old SPMM attachment points. The center of gravity and inertia properties where then tuned with the help of the Adams setup tool in order to obtain the weight distribution and inertia values of the real car. Figure 3.15 shows the shaker rig model with a flexible chassis.
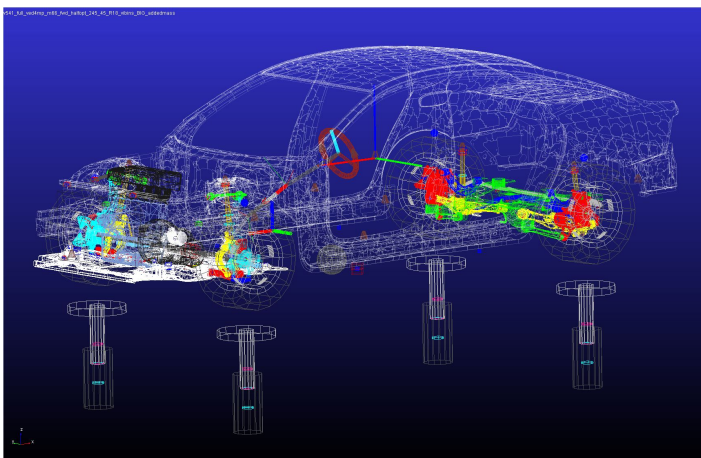

Figure 3.15: *The Car B model with a flexible body*

4 Results

In this chapter the results of tests and simulations will be presented. The first section shows results from SPMM and Shaker Rig tests, followed by damper tests. Finally the results from the linear and non linear quarter car models are presented followed by the full car model.

4.1 SPMM test Car A

Since Car B was not available for testing, Car A was used for shaker rig and SPMM tests. The SPMM tests where conducted in order to see if it is possible to get a good estimation for the static and dynamic friction in the suspension system. The idea was that when the test is conducted very slow, it should be possible to see at which force the system breaks loose and starts to move. The threshold would then be the static friction force. In Figure 4.1 the wheel rates (wheel force versus wheel to body displacement) for the three vertical bounce tests at different cycle times ($300s$,$180s$,$90s$) are shown. No threshold can be identified for the static friction force, but what can be seen is that curve looks the same for all three tests. This implies that the all three test where done slow enough and the damper force did not influence the measured force at the wheel. From this it can be followed that when looking in the linear range of the curve, half of the off-set between the two lines is the dynamic friction force. In this case this is roughly $100N$ per wheel. The non-linear increase in bump travel (right side) is cause by spring progressiveness and the bump stop. The sharp fall of in rebound travel (left side) is generated when the suspension hits the rebound stop and only the "tire spring" is loaded and unloaded.
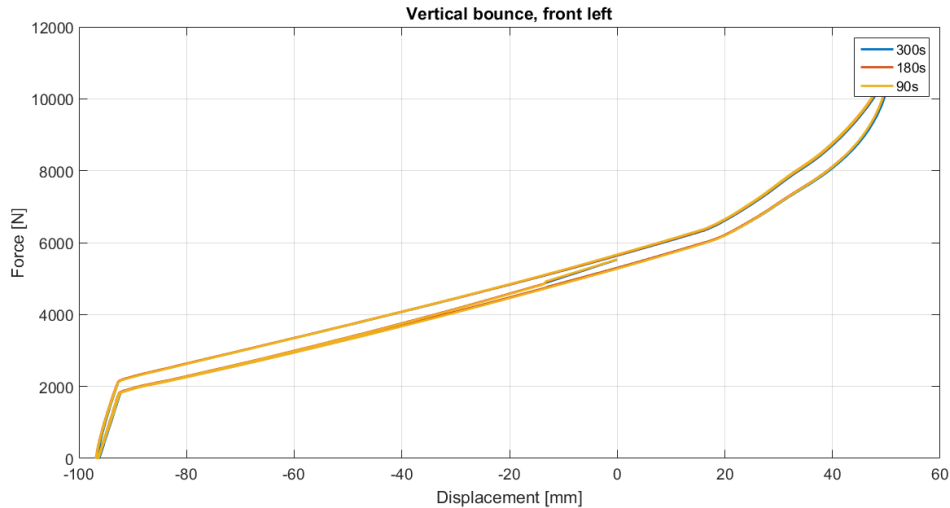
Figure 4.1: *Measured force against wheel to body displacement, cycle times 300s, 180s and 90s*

In Figure 4.2 the wheel rates for the faster cycles times are shown. It can be seen how the hysteresis loop increases due to the damper force which is now apparent in the force-deflection diagram. It can also be seen that the shape of the look changes quiet significantly. This is due to the different amplitudes and frequencies that occurred during these test. The test with a cycle time of $1s$ had an amplitude of $12mm$ and therefore a peak velocity[1] of $75\frac{mm}{s}$. The test with a cycle time of $0.33s$ had an amplitude of $3mm$ and a peak velocity of $57\frac{mm}{s}$. These values can be converted to the values at the damper with the help of the motion ratio (see Section 2.2.1).

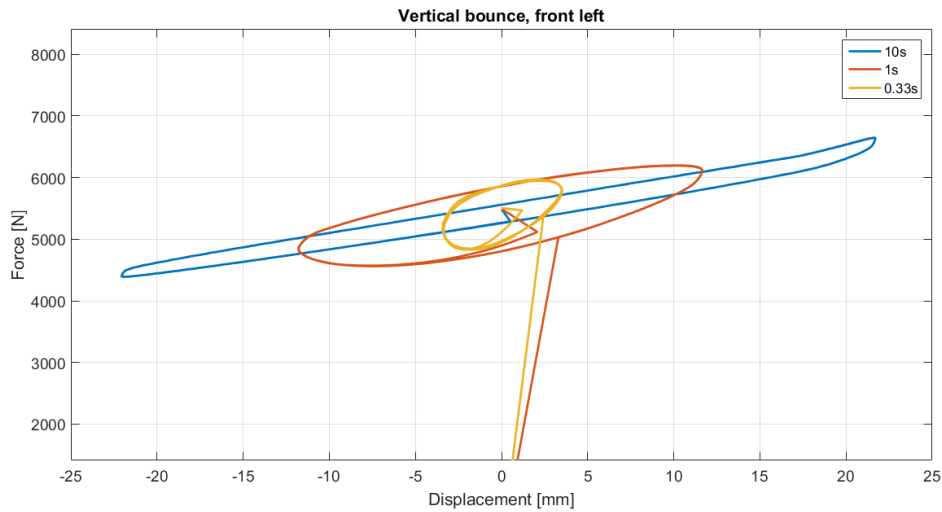[1]can be calculated as $v = \frac{2\pi}{T_{cycle}} * A$

Figure 4.2: *Measured force against wheel to body displacement, cycle times 10s, 1s and 0.33s*

Figure 4.3 shows the tire rates (wheel force versus tire compression) for different vertical bounce tests. For the 90s cycle the curve shows hysteresis which is caused by tire damping. This vanishes for the faster cycle times. It can also be seen that the dynamic stiffness of the tire, which is the inclination of the curve in this force-displacement graph, changes for the different tests.
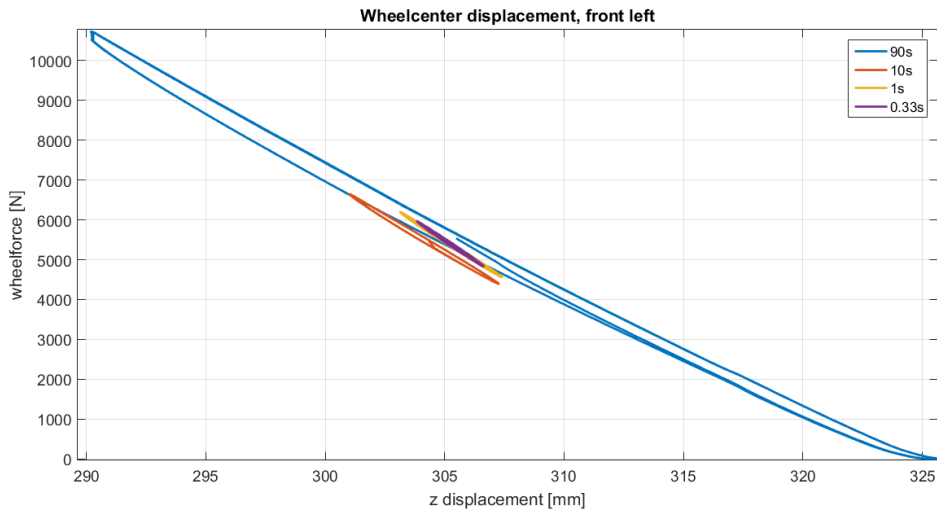
Figure 4.3: *Measured force against tire displacement, cycle times 90s, 10s, 1s and 0.33s*

4.2 Shaker rig measurements Car A

The constant peak velocity result can be seen in Figure 4.4. A can be seen the results differ significantly for the different inputs. This hints to nonlinearities in the system, as for a linear system it would not change for the changed inputs. With decreased maximum input velocity, the transmissibility and the eigenfrequency increases for the sprung mass peak. Between the orange and the purple curve there is a relatively small change. For the blue curve the eigenfrequency drastically increased up to around 4Hz, while for the other two it lies around 2Hz. At the second peak the eigenfrequency decreases with increased input velocity.

Figure 4.4: *Measured transfer functions, response for road to sprung mass*

In Figure 4.5 the transfer function from road to unsprung mass is presented. The behavior is very similar to the one for the unsprung mass. While the purple curve shows transmissibility continuously around 1, the slower test result in different curves. The orange curve shows a different behavior at all frequencies above $5Hz$. For the blue curve the diffe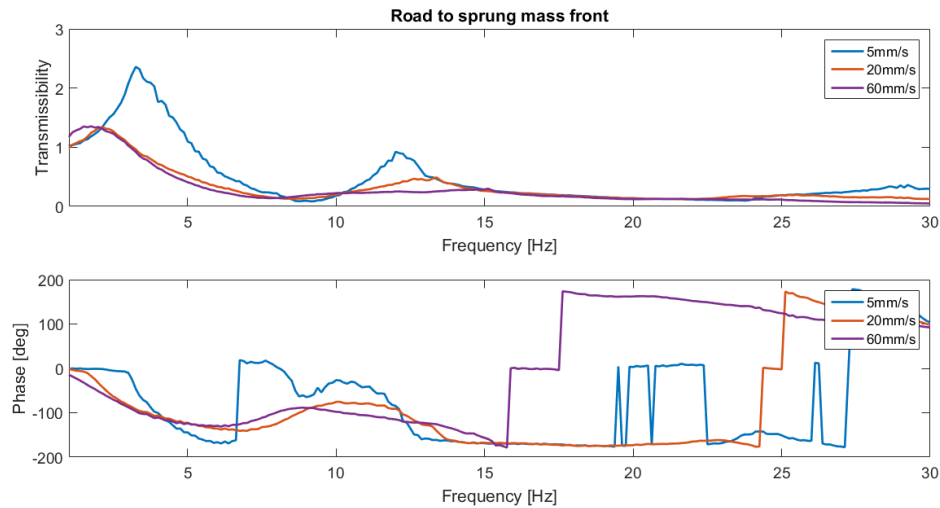rent behavior starts around $2Hz$, where the two others have the sprung mass peak. For both, the sprung and unsprung part, the difference can equally be seen in the phase plots (lower plots in both Figures). Also note the increasing transmissibility for small inputs occurring above 25Hz.
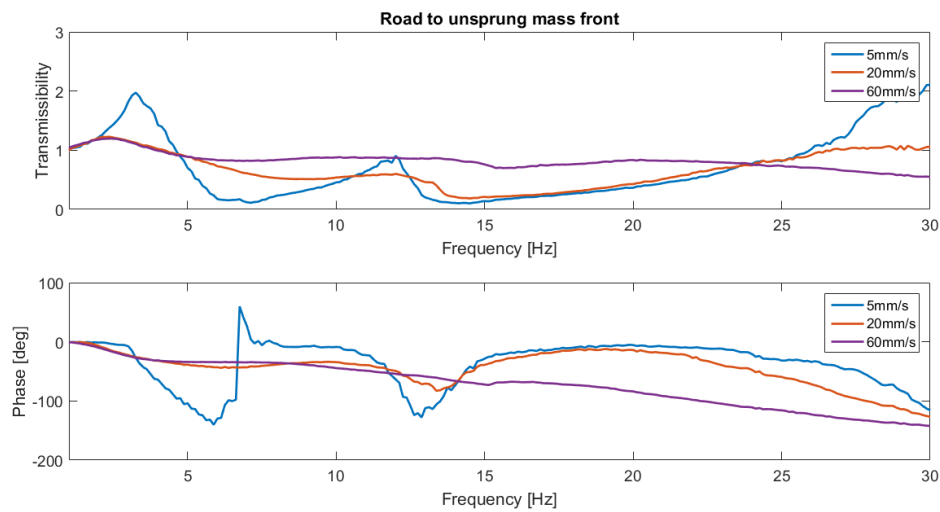
Figure 4.5: *Measured transfer functions, response for road to unsprung mass*

The transfer function from unsprung to sprung mass was calculated as well. The results can be seen in Figure 4.6. It can be seen that when the car is excited with the $5\frac{mm}{s}$ peak input velocity the gain in completely different around $7Hz$. The blue curve shows a clear spike whereas the other curves have a transmissibility closer to zero. Note that the response in the figure are for the left wheel, and that the $5mm/s$ test for the right wheel differs significantly, with its peak at 6 Hz and a gain of 6.7.
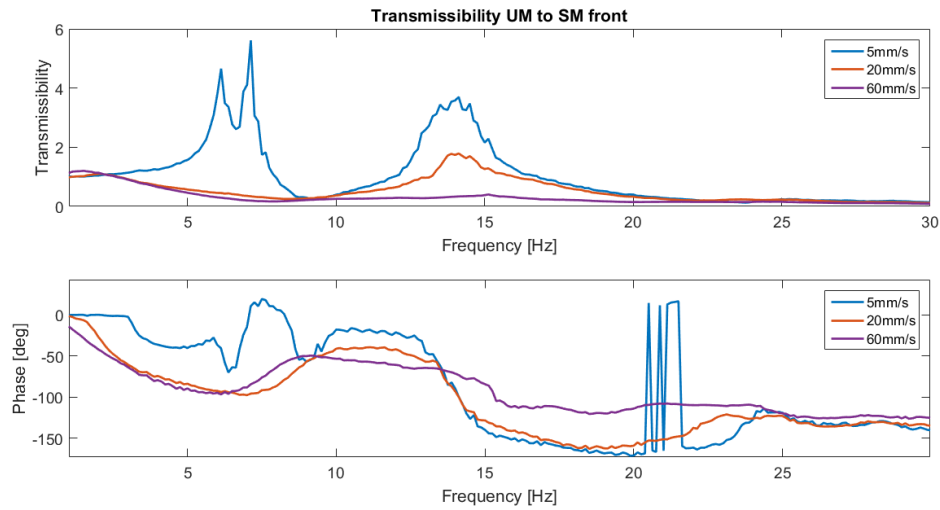
Figure 4.6: *Measured transfer functions, response for unsprung to sprung mass*

The results for the damper travel (measured with the two accelerometers at the damper) are shown in Figure 4.7. More precisely this is the gain and phase for the transfer function between the lower and upper part of the damper. A transmissibility of 1, combined with a phase angle of 0 means that the top and bottom point of the damper have the same relative motion. This is only possible if the damper is not working, more precisely, when the damper is stuck and does neither extend nor compress. For the low velocity input this is true for almost the entire measured frequency range. For the other tests the damper was active over most of the frequency range. The phase angles for the damperstrut (lower point) and damperpiston (upper point) in relation to the road can be seen in the Appendix *("Shaker rig measurements", Figure 6.5).*
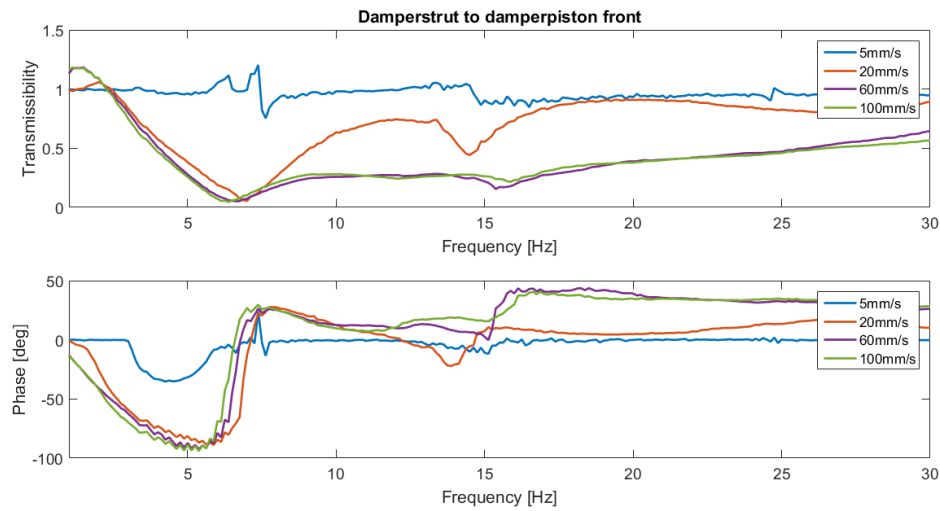
Figure 4.7: *Measured transfer function, from damperstrut to damperpiston*

Further investigation of the dampertravel where made in the time domain. In Figure 4.8 accelerometer data from the damper strut and damper piston are shown for the three different tests with peak pillar velocity of 5, 20 and 60 mm/s. The time series data is taken at the $5Hz$ range seen in Figure 4.7. Again the damperstrut curve is from the lower accelerometer placed close to the control arm, and the damperpiston curve is from the upper accelerometer located close to the topmount. The curves for the $5\frac{mm}{s}$ input show a similar shape of the two measured accelerations, however since the magnitude of the accelerations are small the noise becomes more apparent. For higher velocities the difference becomes larger between the signals, with very apparent spikes in

the damper piston data. These points are equivalent to the end points of the damper travel. It is very likely that these spikes in accelerations are created when the damper sticks and breaks loose.
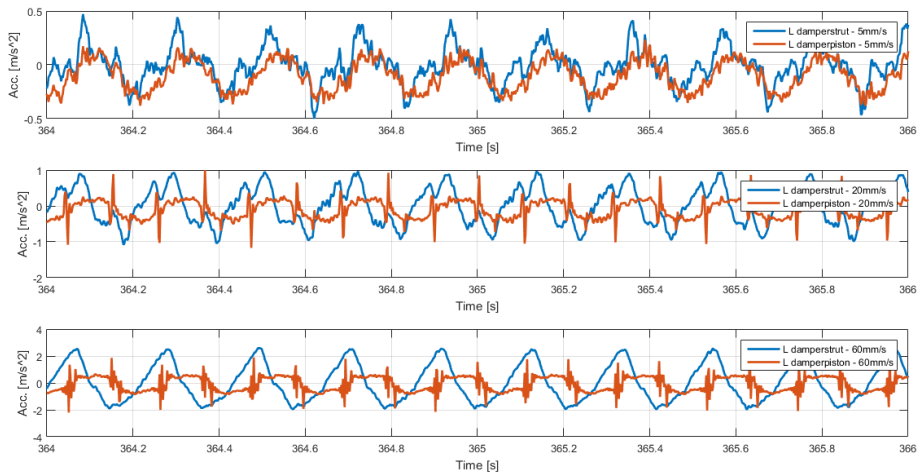
Figure 4.8: *Accelerometer data captured at 5 Hz pillar input*

Note how the spikes in the piston accelerometer data reaches the same value as for the damperstrut, and how they follow each other a short while before the acceleration spikes in the opposite direction. This is especially clear in the 20mm/s data.

4.3 Damper measurement Car A

The measurements done on the damper test rigs show some very interesting insights into the actual behavior of dampers under varying conditions. Figure 4.9 shows data recorded at $131\frac{mm}{s}$ peak velocity for different amplitudes. The upper plot shows the force-velocity diagram, the lower one shows the corresponding force-displacement diagram. Remembering that the standard (simplified) representation of a damper in the force-velocity diagram is a simple line, it can be seen that with decreasing amplitude (and increasing frequency and peak acceleration) the real behavior deviates more and more.

Figure 4.9: *Results for peak velocity of 131mm/s, from test number 2,3,6,7 and 8*

For high peak velocities and large enough amplitudes this behavior is less severe (Figure 4.10). What is still clearly visible is that the force-velocity curve shows a hysteresis loop in the low speed range. Accordingly the force-displacement curves are slightly skewed and not symmetric to a vertical line at zero displacement.
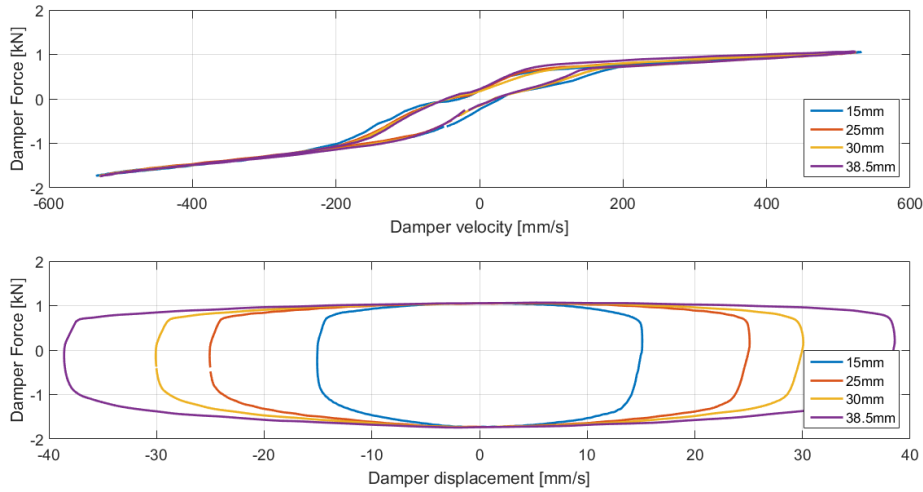
Figure 4.10: *Results for peak velocity of 525mm/s, from test number 2,3,4 and 5*
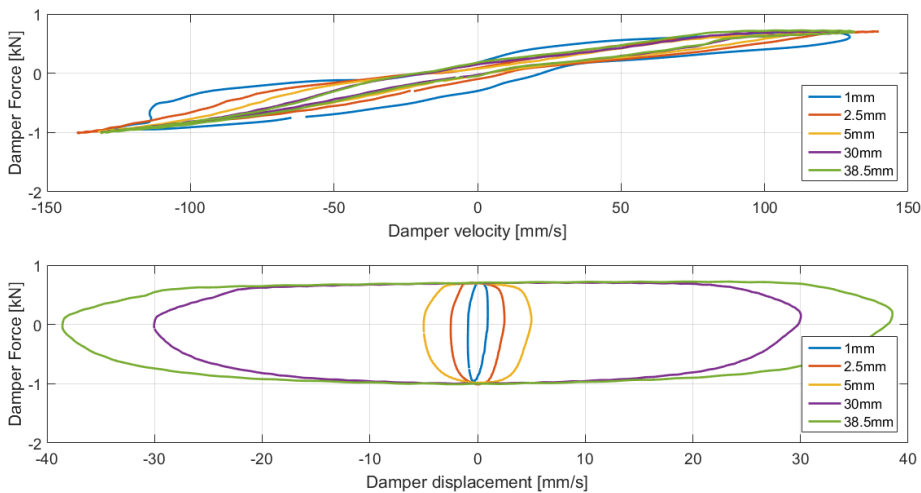
Figure 4.11 shows force-velocity curves for different speeds at small(er) amplitudes. It can be seen that the curves also get out of shape with increased speed at a certain amplitude, something that is true especially for all the shown smaller amplitudes. It is also verified that the behavior of loosing shape with decreased amplitude is true for a wide range of velocities. A similar behavior is still seen for the larger amplitudes for which the plot can be found in the Appendix *("Damper measurements and modeling", Figure 6.6)*. The only difference is that for the large amplitudes velocities need to get very high so that the curve gets out of shape. These velocities above $500\frac{mm}{s}$ are rarely seen under normal operating conditions.
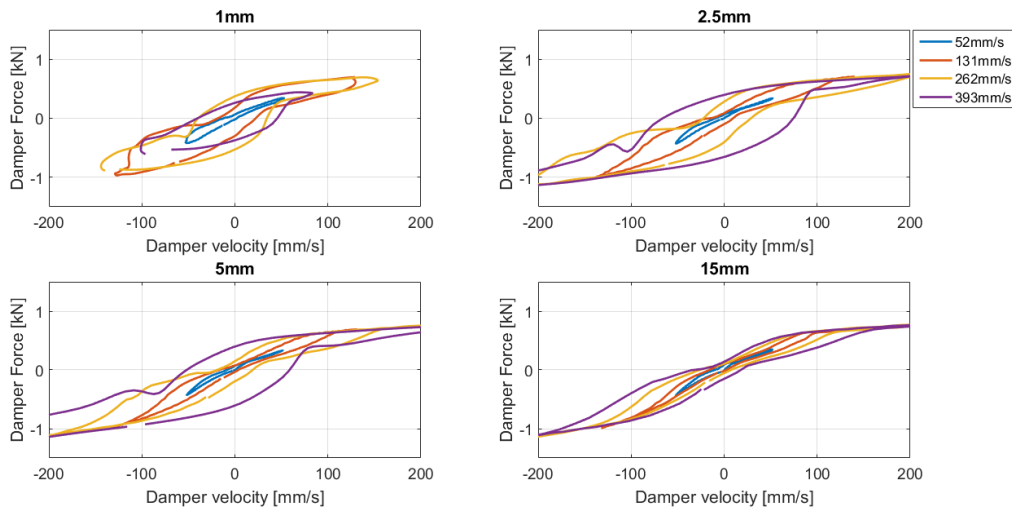
Figure 4.11: *Force velocity traces for smaller amplitudes*

Since at all different amplitudes the same variety of velocities was tested, it was possible to generate the normal force-velocity curves for the different amplitudes. From the different values of "force at peak velocity" the normal force velocity curve is generated. As the damper shows different behavior at different velocities, it would have been expected that the standard force-velocity curves deviate from each other. This is not the

case, as can be seen in Figure 4.12. Except a minimal difference in behavior around the knee of the curve, the different tests all deliver the same curves.
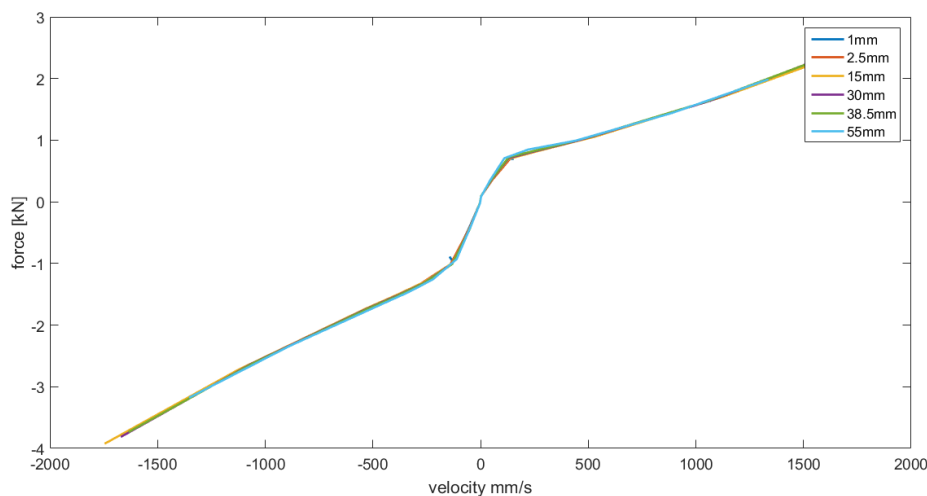
Figure 4.12: *Force velocity curves created from test 1 to 8*

To also compare damper data from different tests in the time series, other measurement data used, where the time series of the test was available. The time series was analyzed and the time delay between force and velocity at the endpoints was calculated, i.e. how large the delay is, between the point when the velocity reaches zero to the point when the force reaches zero. The time delay is the counterpart to the hysteresis loop in the force-velocity diagram. The time delays for the test data can be seen in Table 4.1. It shows again that real damper behavior is highly complex, and that no general coherence between the time delay and velocity, amplitude or frequency can be found. The time delay is different at the same frequency ($30 Hz$), the same velocity ($0.754 \frac{mm}{s}$) and the same amplitude ($8mm$, $15mm$, $45mm$).

Table 4.1: Time delays between velocity and force for a damper at different operating points

Frequency	Amplitude	Velocity	Time delay
30 Hz	2mm	0.377 m/s	0.0018 s
30 Hz	4mm	0.754 m/s	0.0015 s
15 Hz	8mm	0.754 m/s	0.0024 s
10 Hz	15mm	0.9425 m/s	0.0030 s
6 Hz	15mm	0.5655 m/s	0.0037 s
5 Hz	8mm	0.2513 m/s	0.0068 s
3 Hz	45mm	0.8482 m/s	0.0050 s
1 Hz	15mm	0.0942 m/s	0.0114 s
0.5 Hz	45mm	0.1414 m/s	0.0290 s

4.4   Linear quarter car model - parameter sensitivity study

Only primary effects (what happens when one parameter is changed) from the linear quarter car response were analysed. Secondary effects, so called correlations (what happens when a parameter is changed when another parameter is also set to a lower or higher value) where neglected. The effect of the parameters on the sprung mass response is presented in Table 4.2, sorted with the most sensitive parameter to the left. The change in response is presented in root mean square deviation (RMSD). As can be seen, the spring stiffness (K_s) has the largest influence on the body transmissibility. It is followed by the sprung mass (m_s) and the suspension damping (C_s). Also the engine mass (m_s) does effect the results for body transmissibility. Tire stiffness (K_t) and engine mount stiffness (K_e) have a smaller impact on the results. The influence of the unsprung mass (m_{um}), the engine mount damping (C_e) and the tire damping (C_t) is almost negligible.

Table 4.2: Result of parameter sensitivity analysis, sprung mass

Parameter	K_s	m_{sm}	C_s	m_e	K_t	K_e	m_{um}	C_e	C_t
RMSD	0.065	0.049	0.048	0.033	0.02	0.019	0.009	0.008	0.002

In Table 4.3 the effects on the unsprung mass response is presented. Here, the tire stiffness has the biggest influence. It is followed by the suspension damping and the unsprung mass. A smaller influence is shown by the spring stiffness, the tire damping, the engine mount stiffness and the engine mass. The engine mount damping is almost negligible for the linear model.

Table 4.3: Result of parameter sensitivity analysis, unsprung mass

Parameter	K_t	C_s	m_{um}	K_s	C_t	K_e	m_e	m_{sm}	C_e
RMSD	0.151	0.101	0.086	0.02	0.016	0.015	0.015	0.015	0.006

4.5   Non-linear quarter car model

In this section results from different Dymola models are shown. All of them where quarter car models. The results are presented in the same order as the model was developed. First, results are shown for a three mass model where hydro engine mounts and velocity dependent damping was implemented. Second, results from a model which also features a damper top mount and damper strut bushings. Third, the results of a model with the low pass filter hysteresis damper model are shown. Finally, the full model with different friction models is evaluated.

4.5.1   Engine bushings and velocity dependent damping

The results of the model[2] after engine bushings and velocity dependent damping was added can be seen in the following two figures. Figure 4.13 shows the transmissibility and phase from road to sprung mass. In both, the transmissibility and the phase, the biggest difference can be seen in the frequency range from $4 - 14Hz$. The second peak is shifted to a lower frequency. There is also a small, almost not noticeable difference around the first peak.

---

[2]The linear three mass model used for the parameter sensitivity study in MATLAB (Figure 3.6)

Figure 4.13: *Sprung mass response for a Dymola model with velocity dependent damping and engine bushings (blue) and a linear 3 mass model (red) and measurements (yellow).*

Looking at the transfer function from road to unsprung mass in Figure 4.14, the same change is observed. The second peak is shifted to a lower frequency and the range in which the models differ is from $4 - 14Hz$.
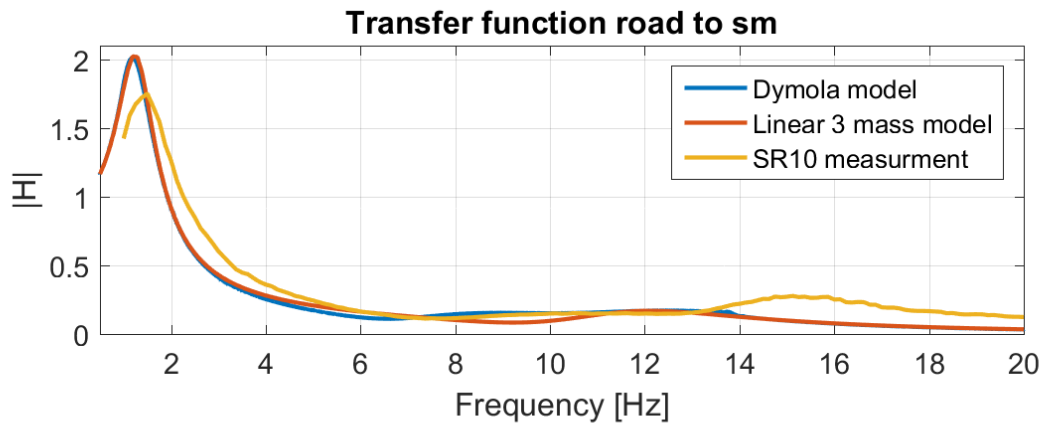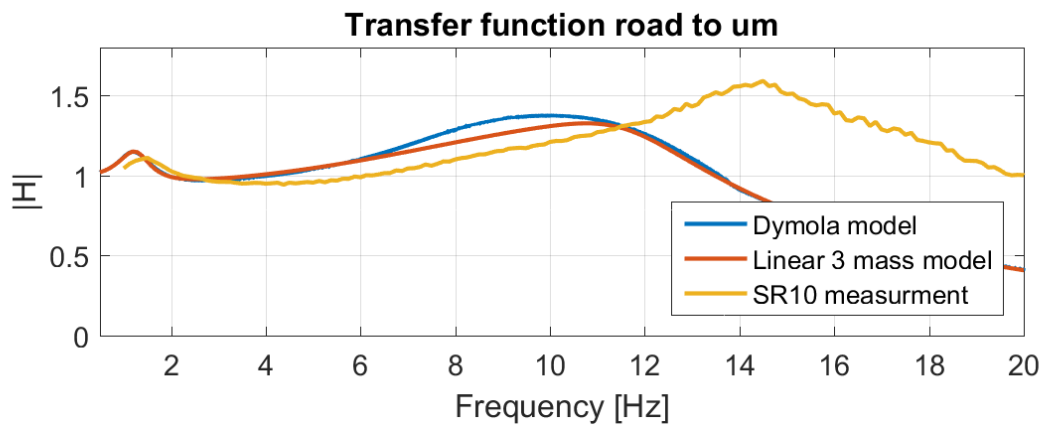

Figure 4.14: *Unsprung mass response for a Dymola model with velocity dependent damping and engine bushings (blue) and a linear 3 mass model (red) and measurements (yellow).*

4.5.2   Topmount and lower damper strut bushings

In Figure 4.15 the results (sprung mass) for the model where topmount and lower damper strut bushings have been added to the model from the previous section. They are compared to measurements and the Dymola model above. For this model the first peak increased slightly in transmissibility and eigenfrequency. The higher frequency range remains fairly unchanged, only at frequencies above $12Hz$ the results differ.

Figure 4.15: *Sprung mass response for a Dymola model with velocity dependent damping, engine bushings, top mount and strut bushings (blue) against the Dymola model above (red) and measurements (yellow).*

Figure 4.16 shows the results for the unsprung mass. The slight shift for the first peak can be seen there as well. More significantly the second peak is also shifted to a higher frequency with lower transmissibility, a behavior that is also visible in the sprung mass.
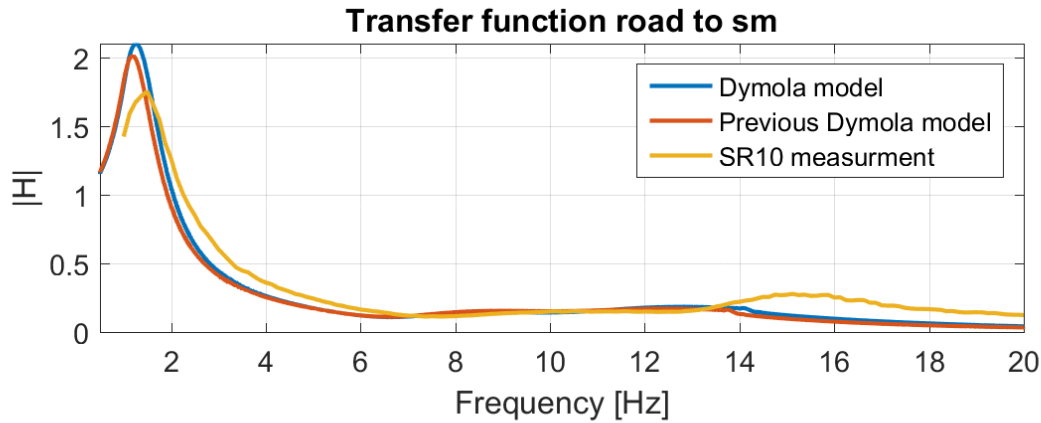

Figure 4.16: *Unsprung mass response for a Dymola model with velocity dependent damping, engine bushings, top mount and strut bushings (blue) against the Dymola model above (red) and measurements (yellow).*

4.5.3 Damper model with hysteresis

In the same way as before, now the results for adding hysteresis to the damper model are presented. Here using the parameters $k = 3$ and $offset = 0.5$ for the low pass filter. The dampermodel using these parameters are compared with damper test data in appendix A. Figure 4.17 shows the results for the sprung mass. Same as for the introduction of velocity dependent damping, the results did not really change.

Figure 4.17: *Sprung mass response for a Dymola model with velocity dependent damping with hysteresis, engine bushings, top mount and strut bushings (blue) against the previous Dymola model above (red) and measurements (yellow).*

In the results for the unsprung mass the model change became only apparent in the frequency range above $10Hz$. A small offset in phase and transmissibility can be seen there. The rest of the curve remained almost unchanged.
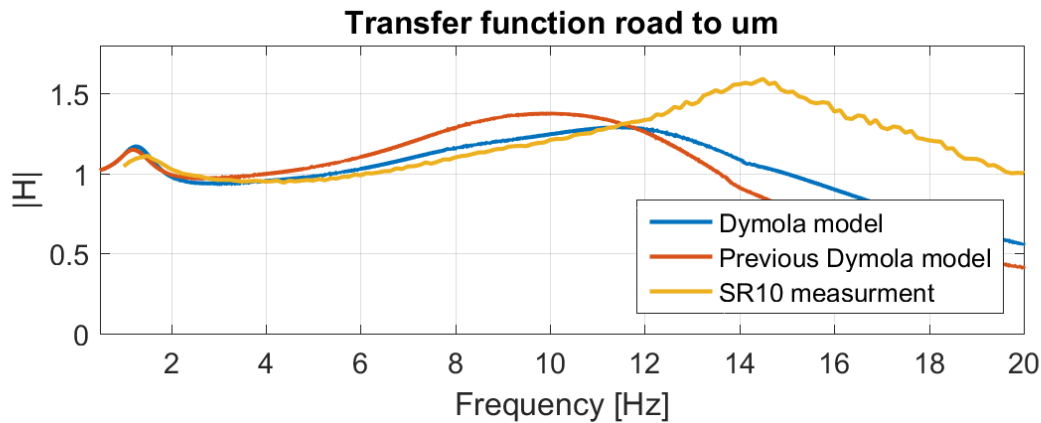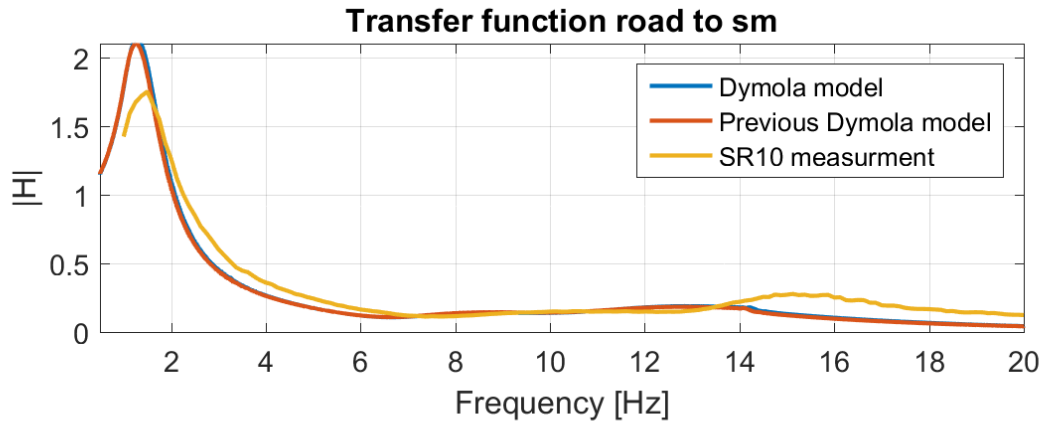

Figure 4.18: *Unsprung mass response for a Dymola model with velocity dependent damping with hysteresis, engine bushings, top mount and strut bushings (blue) against the previous Dymola model above (red) and measurements (yellow).*

4.5.4 Different friction models

All the friction models are parametrized to give 200N of Coulomb friction (for the entire front axle, i.e 100N per wheel). No difference between static and dynamic friction has been made. The response obtained by adding different friction models in parallel with the sprung and unsprung mass can be seen in Figure 4.19. Both, the normal LuGre model and the tanh model show good correlation around the first peak and up to $12Hz$. The LuGre model with decreased bristle stiffness shows too high transmissibility at the first peak and too low after the first peak. For the frequency range above $9Hz$ the three models show no real difference in transmissibility.
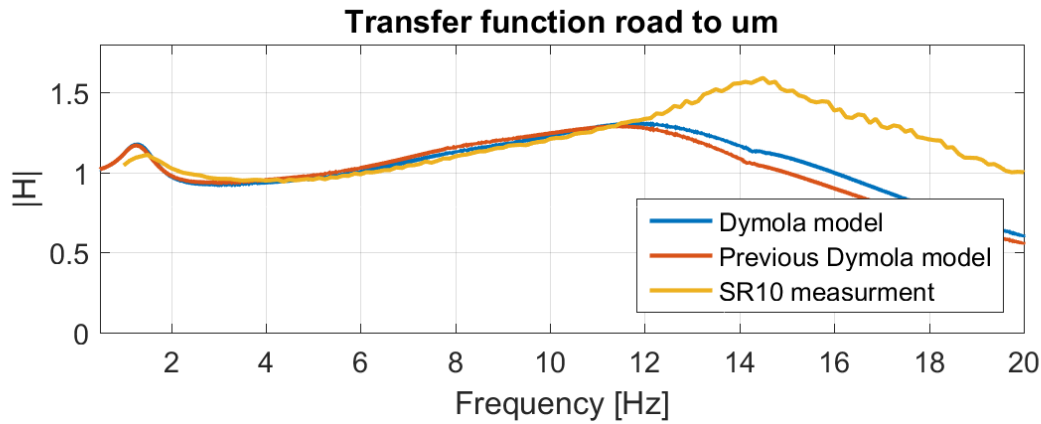
Figure 4.19: *Sprung mass response for a Dymola model with velocity dependent damping with hysteresis, engine bushings, top mount, strut bushings and different friction types between sprung and unsprung mass (blue, red, yellow) and measurements (purple).*

In the results for the unsprung mass (Figure 4.20) a larger deviation between the friction models and test data can be seen. All friction models over-predict transmissibility at the first peak and under-predict the eigenfrequency by a small amount. Above $4Hz$ the decreased LuGre model shows best correlation, but under-predicts the second peak in transmissibility and frequency. The standard LuGre and the tanh model show poor correlation at frequencies above $4Hz$ respectively $6Hz$.

Figure 4.20: *Unsprung mass response for a Dymola model with velocity dependent damping with hysteresis, engine bushings, top mount, strut bushings and different friction types between sprung and unsprung mass (blue, red, yellow) and measurements (purple).*

The response to sprung mass for adding different friction models in parallel to the damper can be seen in Figure 4.21. Here the hybrid and the tanh model show the best results. The hybrid model shows especially good behavior around the first peak. The second peak is still not captured correctly by any of the models.
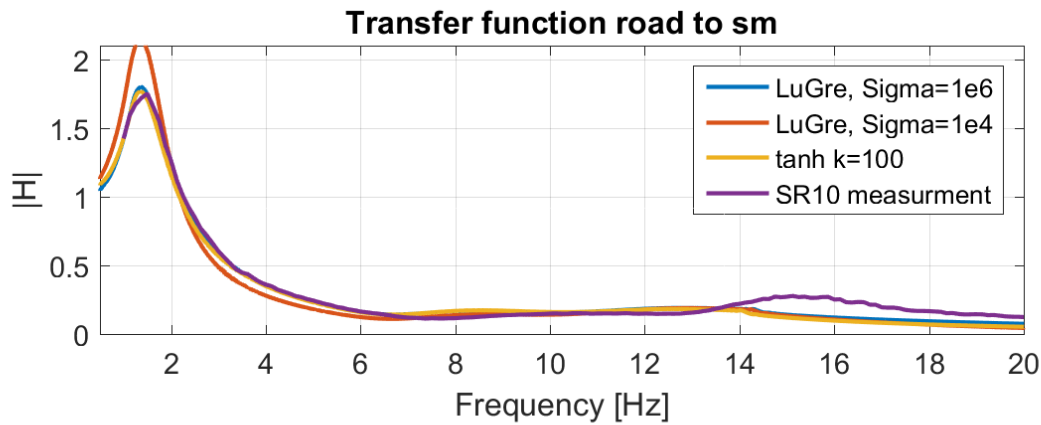
Figure 4.21: *Sprung mass response for a Dymola model with velocity dependent damping with hysteresis, engine bushings, top mount, strut bushings and different friction types across the damper (blue, red, yellow) and measurements (purple).*

Figure 4.22 displays the results for the unsprung mass. Up to $6Hz$ the hybrid model shows the best behavior. The tanh model also seems to correlate relatively good up to $4Hz$. At the higher frequencies it fails to capture the second peak and follow the test data. The decreased LuGre model correlates between $4-11Hz$. All models still under-predict the second peak in frequency and transmissibility.
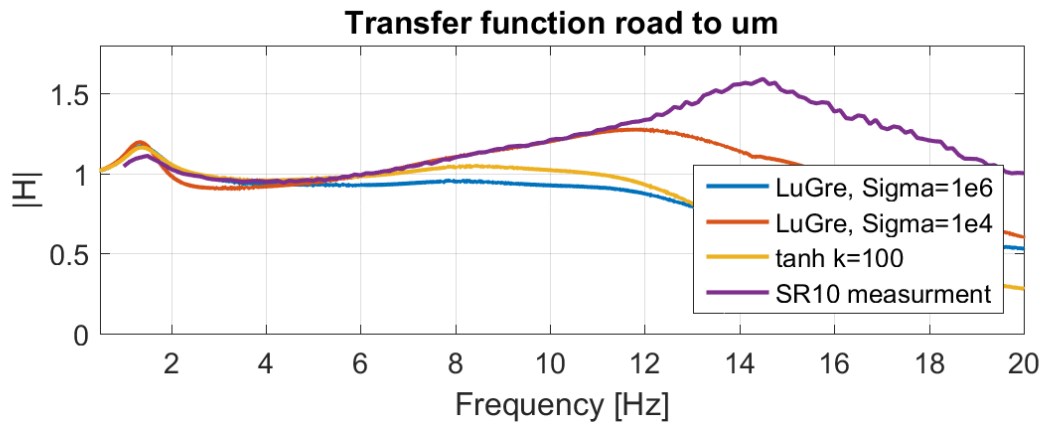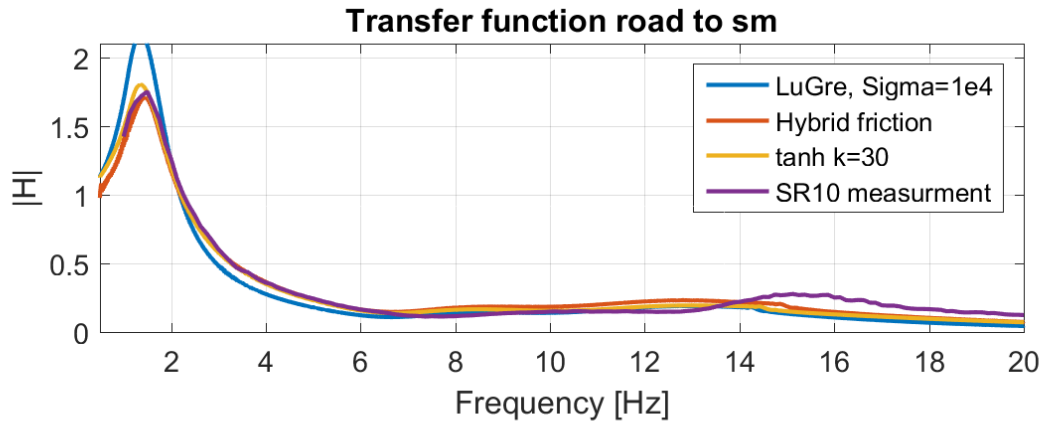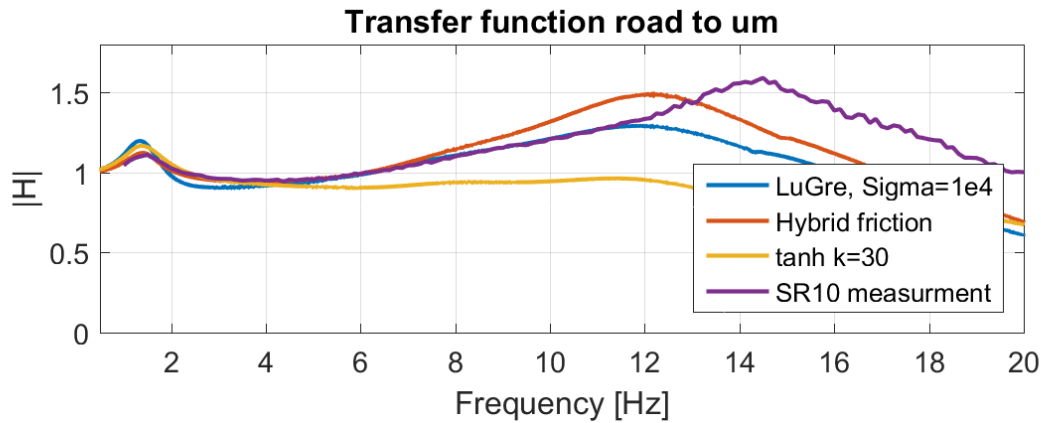

Figure 4.22: *Unsprung mass response for a Dymola model with velocity dependent damping with hysteresis, engine bushings, top mount, strut bushings and different friction types across the damper (blue, red, yellow) and measurements (purple).*

4.5.5 Varying the damper hysteresis

Since the damper hysteresis was parametrized for the damper on Car A, while the test data was compared to Car B with an unknown damper hysteresis behaviour, the filter parameters were varied to see the impact from the size of the hysteresis loop. For this the Dymola model from section 4.5.4 with LuGre friction between sprung and unsprung mass was used. The response obtained by varying the damper delay by changing the gain parameter k in Equation 3.20 can be seen in Figure 4.23. For low values of k the transmissibility and frequency at the first peak become to high.
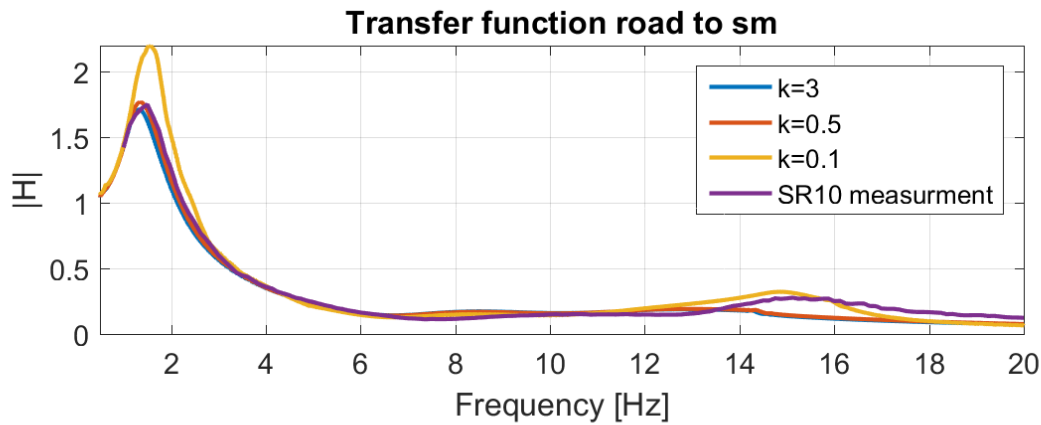
Figure 4.23: *Sprung mass response for different damper hysteresis.*

Figure 4.24 shows the results for the unsprung mass. The low k hysteresis models shows a spike that is too high in transmissibility and also at a too high frequency. This is the reason for the better correlation around 15Hz in Figure 4.23.
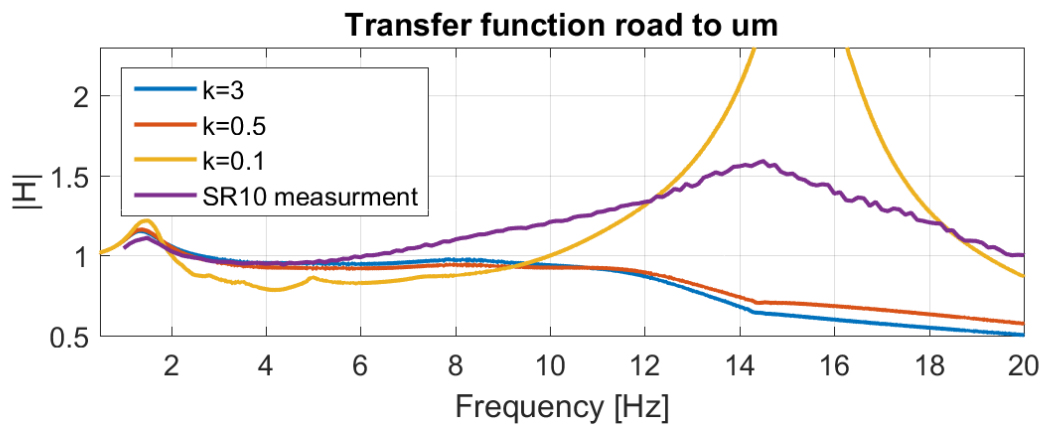
Figure 4.24: *Unsprung mass response for different damper hysteresis.*

4.5.6 Varying the peak pillar velocity - Car A

Finally in Figure 4.25 we can see the response for different input peak velocities. Note that this is Car A measurements compared with a Dymola model only partly parametrized to Car A. This since no bushing measurements where found for this vehicle. However, the general trend captured with friction can be seen, as an decrease in input velocity yields and increase in sprung mass eigenfrequency and transmissibility. Also the increase in transmissibility in the high frequency range is apparent, but at a lower frequency and with smaller magnitude.
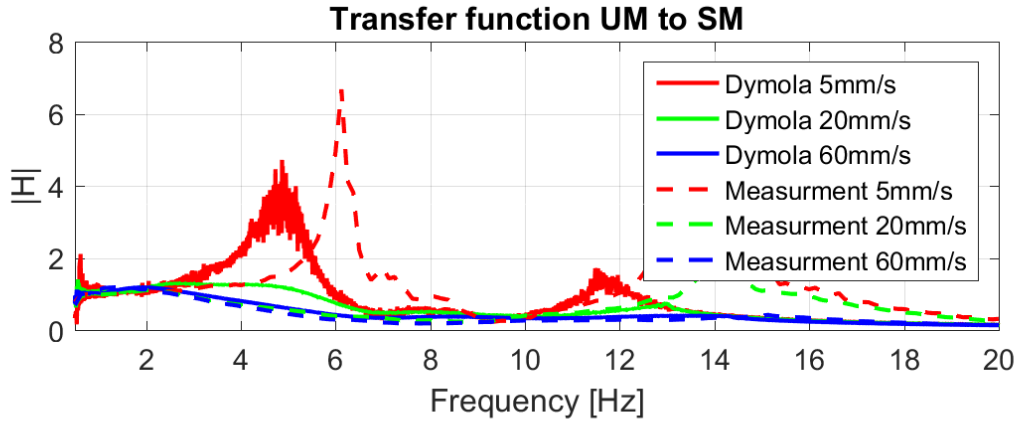
Figure 4.25: *UM to SM response for different peak velocities (Car A). Hybrid friction across the damper.*

4.6 Full car multi-body model

The following subsection contain selected results from the Adams simulations. In the beginning results from the initial model are shown and described. After this results from models with friction are presented. Included in this are comparisons of the two tire models and simulations with different amount of friction. The simulations with the initial model could be done without any issues. The computation time was also rather short, ranging from 4 hours with the Pacejka model (run local on a mobile workstation) to 8 hours with the FTire model (run on a cluster). When friction was implemented convergence problems occurred. For one full shaker rig analysis, $2*21$ simulations need to be done for the low frequency range of $0-3Hz$ (front & rear axle). $2*35$ simulations need to be done for the high frequency range ($3-20Hz$). With implemented friction it became impossible to get convergence with the GStiff solver. Instead the HHT solver had to be used. Even then, single simulations did not converge so that the data obtained was often incomplete. That especially occurred when friction was implemented in the ball joints. It could be observed that it was easier to achieve convergence when the axle the car was pivoting around[3] had low values of static and dynamic friction implemented.

Table 4.4: Solver settings for Adams simulations (HHT)

Parameter	Adams variable name	Value
Max. allowed error	ERROR	$5.0*10^{-5}$
Initial time step	HINIT	$8.0*10^{-5}$
Max. time step	HMAX	$2.0*10^{-4}$

Table 4.4 shows the solver settings that have been found to work best with friction implemented in dampers and ball joints. Even with theses solver settings it was not possible to solve all single simulations when friction with high values was implemented (reaction force friction in ball joints and more that 100N of static friction force due to pre-load in the dampers). As the default result the transmissibility from road to sprung mass will be displayed in the following. Results for road to unsprung mass and the rear axle are mainly found in the appendix. All results are taken for the left side of the car, as no difference could be seen between left and right side in all simulations.

4.6.1 Simulations with the initial model

The initial Adams model was used to redo the already done simulations at Volvo to confirm that the model is the latest version that was worked with in the department. Additionally the HHT solver was compared to the GStiff solver. Figure 4.26 shows the transmissibility from road to body at the front axle. The dashed line is the result of the real shaker test. The blue line (GStiff) and the green line (HHT) are simulation results. It can be seen that both solvers deliver the exact same results. The simulation is over-predicting the transmissibility

---

[3]For a shake on the front axle the pivoting axle would be the rear axle

with 2 compared to 1.75 from the test. The body eigenfrequency is under-predicted with ($1.2Hz$) compared to $1.5Hz$ from the test. It can be seen that in the range of $6Hz$ to $16Hz$ the test data has two local peaks that are connected to the engine-shake ($10Hz$) and the peak of the unsprung mass ($15Hz$). In the simulation data the engine peak is not really detectable. The tire peak (unsprung mass) is under-predicted in transmissibility (0.3 compared to 0.6) as well as in frequency ($13.75Hz$ compared to $15Hz$). Especially in the higher frequency range the transmissibility becomes even more under-predicted. The behavior that was described for the high and low body plots is analogously be seen in the plots for the transmissibility to unsprung mass (Appendix E).
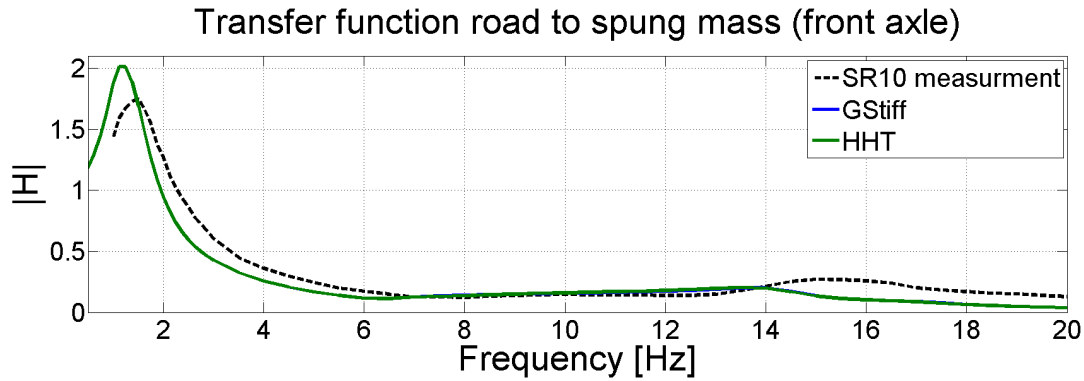
Transfer function road to spung mass (front axle)

Figure 4.26: *Transmissibility (0 − 20Hz front) road to body for the initial model with different solvers*

The transmissibility for the low frequency on the rear axle can be seen in Figure 4.27. Compared to the front axle (Figure 4.26) it can be seen that the eigenfrequency is again under-predicted with $1.5Hz$ compared to $1.75Hz$ from the shaker test. The peak transmissibility is nevertheless almost the same for simulation and test with 1.7. Also the shapes of the curves are similar so that it looks as if in the low frequency range the complete curve for the simulation is shifted slightly the left from the test results. The test curve as well as the simulation curves show good correlation in the high frequency range. Only in the highest range above $17Hz$ the curves start to deviate a bit from each other. For the transmissibility from road to rim the curves show no correlation at all, see Appendix E. The test curve is after an initial dip constantly increasing up to 1.5 at a frequency of $19.75Hz$. This peak in transmissibility is generated by the unsprung mass. The simulation results do not capture this behavior, instead the transmissibility becomes even lower than 1.

Transfer function road to spung mass (rear axle)
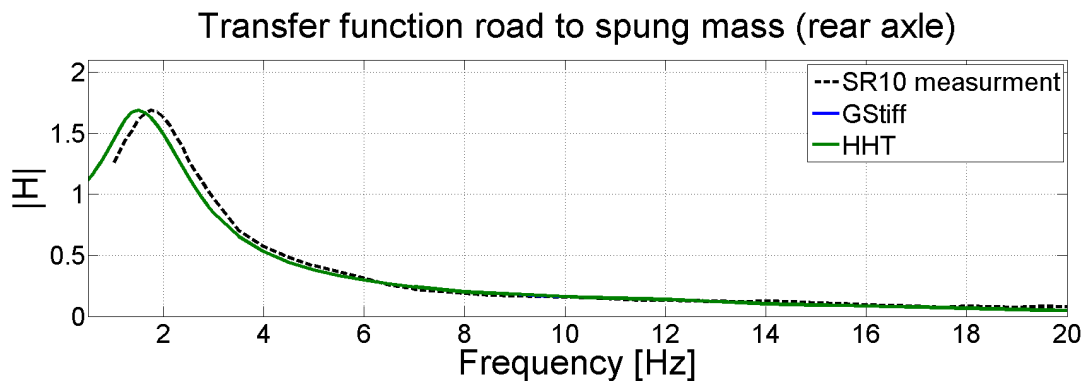
Figure 4.27: *Transmissibility (0 − 20Hz rear) road to body for the initial model with different solvers*

4.6.2 Simulations with friction in the damper struts at the front axle

The results for simulations with friction implemented in the damper joint at the front axle are presented below. as a reference the results from the initial model are also included in the plots (green line). The test results are again shown as dashed line (black). Two different simulations with friction are compared to them. The blue line shows the results for a simulation when $200N$ of static friction and $150N$ of dynamic friction force was implemented per wheel. The other set-up (red line) shows results for a simulation when no pre-load was used

and instead the reaction forces and moments in the damper joint. All following simulations where done with the Pacejka tire model.

Figure 4.28 shows the results for road to body. It can be seen that the reaction force friction (red) shows almost no difference to the simulation without friction (green). The pre-load friction simulation (blue) shows decreased transmissibility (1.7) and an increased eigenfrequency ($1.6Hz$). Especially below $1.6Hz$ the curve correlates better to the test results. Also above $1.6Hz$ an improvement in correlation can be noticed.

Transfer function road to spung mass with friction in the front (front axle)

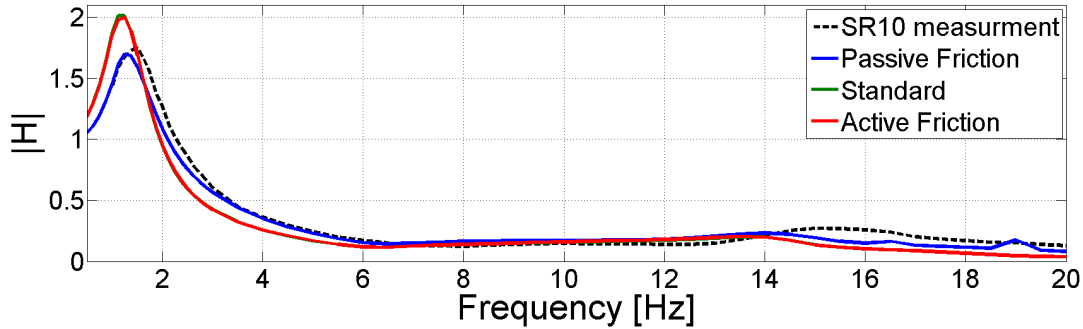Figure 4.28: *Transmissibility ($0 - 20Hz$ front) road to body for a model with friction in the front damper struts*

In the high frequency range a similar behavior can be observed. The active friction shows no difference to the simulation without friction. The pre-load friction curve shows better correlation to the test results. The eigenfrequency ($14Hz$) as well as the transmissibility ($-13dB$) are higher and also in the frequency range of $3Hz - 6Hz$ better correlation can be seen. Around $12Hz$ the friction doesn't have an effect on the results, as all curves lie close together. When friction is implemented, the transmissibility from road to rim (Appendix F) is drastically decreased in the high frequency range. Also the peak transmissibility occurs on a different frequency ($11.5Hz$) than it is seen in the sprung mass ($14Hz$).

4.6.3 Simulations with friction in all damper struts (front & rear)

The following figures show results for simulations where frictions was implemented at the front and the rear axle in the dampers. The results from the intial model are kept once again as a reference (green line). The blue curve is a simulation where the Pacejka tire model was used. $200N$ static friction and $150N$ dynamic friction. The purple curve represents a similar simulation, but in this case also the reaction forces where taken into account for the friction force. The red curve represents the same friction set-up as the blue curve, but instead the FTire model was used. Test results are as before shown as a dashed black line. The plots for the rear can be found in Appendix G. As the transmissibility in the rear is too low with these friction values, it is suspected that there is less friction in the rear suspension, which could be due to the fact that the damper is mounted separately and therefore not exposed to a bending moment.

Figure 4.29 shows similar results to the simulations where friction was only implemented at the front axle. The friction on the other (rear) axle doesn't seem to influence the results. The simulation where additionally the reaction forces where taken into account shows slightly higher transmissibility in the frequency range of $0.5Hz$ to $1.5Hz$. The difference between the two tire models is almost negligible in the low frequency range. Only between $0.8Hz$ to 1.3 the model with the FTire model shows a slightly lower transmissibility by 0.05.
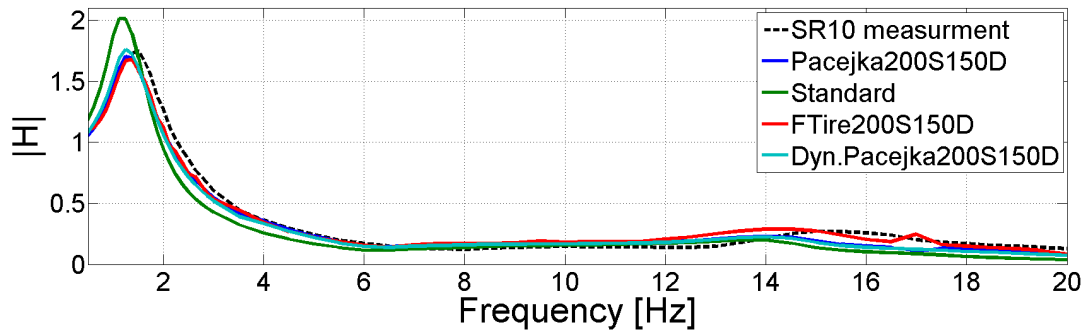
Figure 4.29: *Transmissibility (0 − 20Hz front) road to body for the model with friction implemented in all damper struts*

In the high frequency range the difference between the two tire models becomes more visible. The unsprung mass peak is at a higher frequency (14.5*Hz*) and shows higher transmissibility than the simulations with the Pacejka model, where for both version the eigenfrequency is at 14*Hz*. Some of the curves show local spikes, which are due to single simulations at a specific frequency which where erroneous. Compared to the test results, the eigenfrequency of the unsprung mass is still under-predicted and the transmissibility is to high in the frequency range from 6*Hz* to 15*Hz*.

Figure 4.30 shows the results for transmissibility from road to rim. Also here the difference between the FTire and the Pacejka model can be noticed. in comparison to the Pacejka simulations with friction, the FTire model shows again increased transmissibility around the unsprung mass eigenfrequency. The curve has a waved shape with some local spikes. Therefore no clear peak can be identified. The Pacejka curves again drift into the transmissibility region below 1 and shows a peak that doesn't match the peak in the body transmissibility as it is seen for the test data.
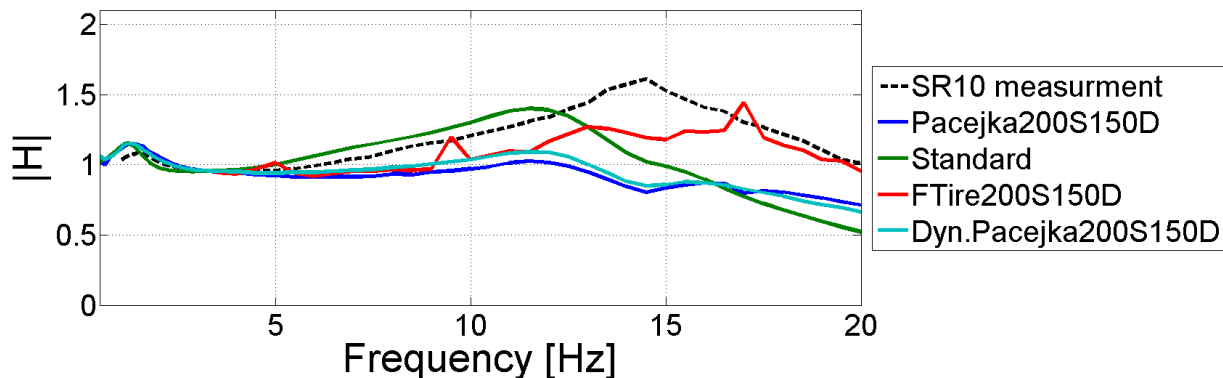

Figure 4.30: *Transmissibility (3 − 20Hz front) road to rim (front) for the model with friction implemented in all damper struts*

4.6.4 Simulations with friction in the ball joints

The results for simulations where friction was implemented in all dampers as well as all ball joints are presented in this section. For theses simulations it was in general hard to obtain converged results. Especially when the pre-load friction in the dampers was increased convergence problems occurred. It was nevertheless possible to obtain two almost complete shaker rig simulation results with different set ups. The green and dashed-black lines are as before the initial model and shaker test results. The blue lines represent the results of a simulation with the Pacejka tire model where 200*N* of static friction and 120*N* of dynamic friction where used in the dampers (front & rear). The reaction forces in the damper joint where also taken into account for the friction force. The red curves are from a simulation done with the FTire model. In the front 150*N* of static and 100*N* of dynamic friction where used. For the rear axle these values where decreased to 50*N* static and 30*N* dynamic friction. For all dampers the reaction forces where taken into account as well.

In the low frequency range (Figure 4.31) the single simulation results where obtained almost everywhere for the model with lower friction (red). Only around $2.3Hz$ to $2.5Hz$ some simulation didn't converge. The general shape of the curve can still be clearly seen and the sprung mass peak is visible as well. The simulation with more friction (blue) has two gaps, one from $1.6Hz$ to $1.9Hz$ and one from $2.4Hz$ to $2.7Hz$. Also here the shape is clearly identifiable with all necessary information. The blue curve shows the lowest transmissibility (1.59) and has the eigenfrequency at $1.4Hz$. The red curve has the same eigenfrequency but a slightly higher transmissibility of 1.68. Both simulations under-predict eigenfrequency as well as transmissibility compared to the test results. From $2.2Hz$ to $3Hz$ both curves show good correlation with the test results.

In the high frequency range (Figure 4.31) the good correlation continues up to $6.5Hz$. Between $6.5Hz$ up to $14.5Hz$ transmissibility is to high compared to the test. The unsprung mass peak is in both simulations at a little bit lower frequency. Both simulation show the peak at $14.5Hz$ (compared to $15Hz$). The model with low friction and the FTire model is over-predicting transmissibility slightly again. The high friction model with the Pacejka tire model is under-predicting transmissibility with $12.25Hz$.
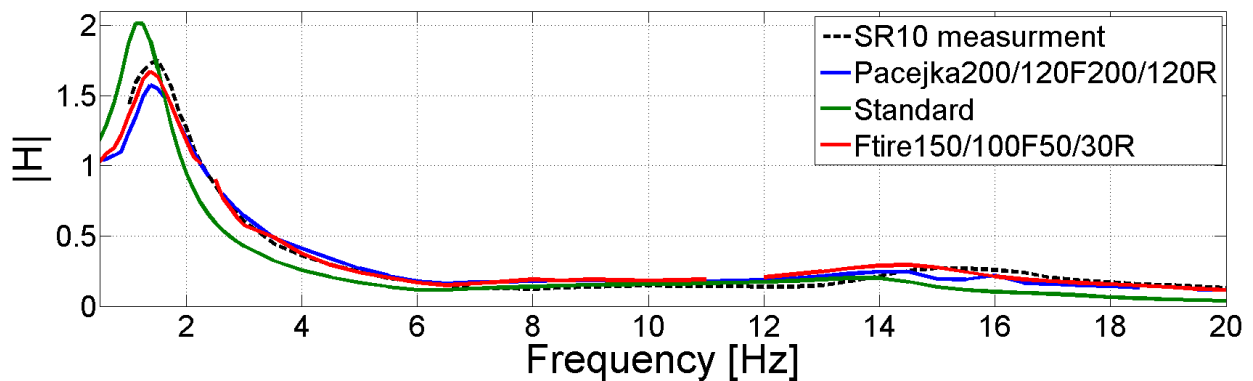

Figure 4.31: *Transmissibility $(0-20Hz$ front) road to body for the model with friction implemented in all dampers and ball joints*

4.6.5 Simulations with a flexible body chassis

The model for shaker rig simulations where a flexible body was used as chassis was not possible to analyse during this thesis work. As described in Section 3.6.4 it was tried to add the missing mass to the chassis by attaching to the floor in the region of the B-pillars. As can be seen from Figure 4.32 the results for this model are still implausible. It was not further investigated why this is the case. In any case it is clear that the missing weight is large and that attaching it just to one point on the chassis will have an impact on the results, because a large mass is connected on an arbitrary point to a flexible body.
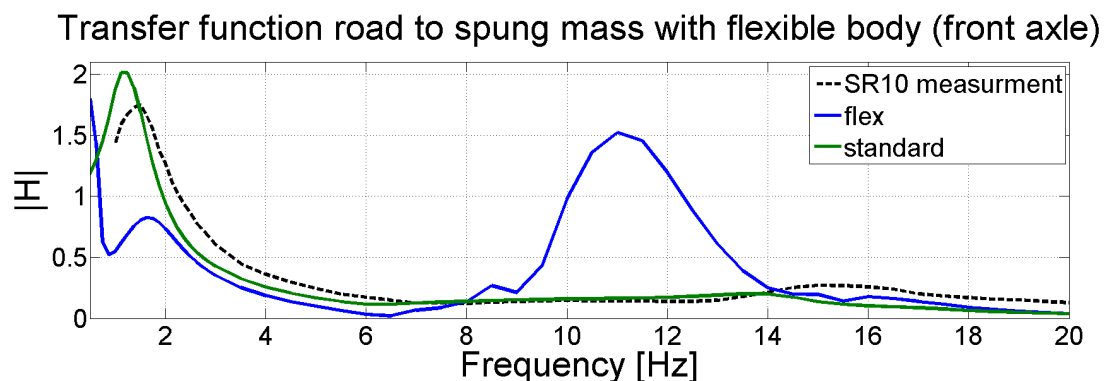

Figure 4.32: *Low frequency transmissibility to body results for the front axle of the model with a flexible body chassis*

4.7   Model comparison

Finally all the models are compared. In Figure 4.33 the low frequency range is shown and in Figure 4.34 the high frequency range[4]. Here "best Adams model" is with F-tire and 150N static and 100N dynamic friction in each damper, and additional friction from the reaction forces in the ball-joints in the spindle. The Dymola model is with 200N of "Hybrid friction" force across the damper (representing both wheels since it is parametrized as a half car).

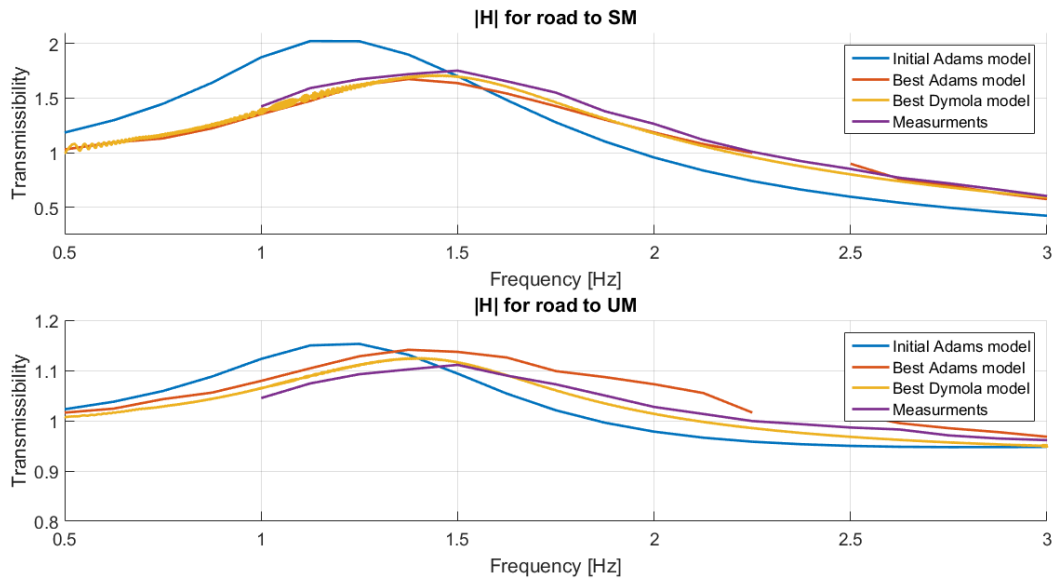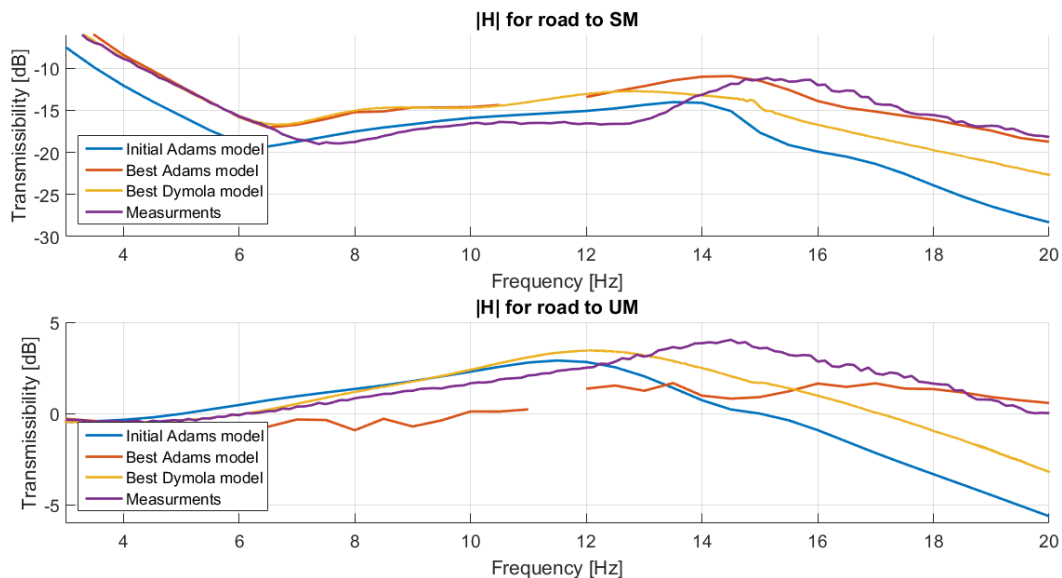Figure 4.33: *Low frequency transmissibility for different models*

Figure 4.34: *High frequency transmissibility for different models*

---

[4]note that the scale is in *dB* for the high frequency range in order to see differences more clearly

5 Discussion

The discussion of the results will be done in the same order as they where presented in the previous section. The parameter sensitivity study which was done with the linear three mass model in MATLAB shows the results as root mean square deviation. This gives a good overview about which parameters will have an large effect on the results. The influence of the parameters will however change when a more complex model is analyzed. For example the linear damping of the engine bushings has only a small impact on this model. When hydro engine bushings where used in Dymola simulations, this observation was not valid any more. Nevertheless some general insights could be gained, as for example that the tire stiffness has a large impact on transmissibility to unsprung mass and that the wheel rate has a large impact on sprung mass. Also the damping of the suspension has a big influence on sprung and unsprung mass responses. Thus it is important to model bushings that changes dynamically, since they both contribute with stiffness and damping.

In the slow vertical bounce SPMM tests no difference can be seen between the sticking friction force and the dynamic friction force. What can be seen is, that the dynamic friction force is roughly equal over the entire wheel travel. The test was done with the tires resting at pads that can float in the lateral direction. In the shaker rig the tires are resting on laterally fixed posts, this means that the friction force could be changing more over wheel travel due to lateral forces induced by the suspensions track width change. In Figure 4.2 it can also be seen that the wheel rate is changing dynamically, thus the dynamic stiffness is changing for Car A. The hysteresis also changes due to damping forces.

From the shaker tests it is obvious that there are large non linearities in the system, because the transmissibility changes for different peak input velocities. This large non linearity are coupled to a large change in the transfer function gain for the damper travel. This suggested friction forces in the suspension partly or fully locking the suspension system, leading to a stiffer system. It also shows very fast transients for the damper piston (high acceleration peaks occurring during stick slip friction). This is a damper operating condition that was not investigated. It also suggests that the top mount needs to be modeled for higher frequencies than the actual frequency input from the pillar. This might be reasons for why the accelerometer data of the damperstrut and the damperpiston looks very different in the simulations compared to the test data.

The measurements of the dampers show hysteresis loops in the force velocity diagram which are changing with input amplitude as well as peak velocity. Especially for high velocities at low amplitudes these loops become very large. A large loop in the force velocity diagram means that the damper is more acting like a spring than a damper and that effective damping is decreased. It is assumed that this behavior is caused by compressibility of the damper fluid, cavitation and backlash. Note that the force velocity diagrams generated from the different tests (generalized force-velocity curves) look more or less identical, when the actual measured response differs widely, which means that a standard force-velocity curve cannot capture important characteristics of a damper.

Adding a non linear damper model (force velocity diagram) to the linear quarter car model in Dymola made no major difference to the response, this is since the damper velocities are small and in the fairly linear range. However, the hydro engine bushings make a significant difference compared to the linear bushings, mainly in the frequency range of 4 to $14Hz$. Adding the top mount and the damper strut bushings made a large difference in response with regard to the unsprung mass, correlating more to the measurements. The response from road to sprung mass remained fairly unchanged.

The damper hysteresis model also didn't effect the results noticeably. However, neither test data from the damper in Car B, nor test data at very small amplitudes was available. The low pass filter model used gave good correlation considering the low complexity, but for very small amplitudes and high velocities the measured curves loose their shape and have a lot of hysteresis, something that could not be modeled without changing the filter parameters. More complex models, either based on fluid flow and valve properties, or more advanced empirical models might be able to deliver even better results. It might also be possible to capture this behavior to a certain extent by characterising the damper force as a function of velocity and acceleration. However the necessity for a more accurate damper model for vertical vibration insulation can be questioned. As can be seen in Figure 4.23 shows a very large hysteresis loop which increases eigenfrequency and transmissibility, thus for higher damper speeds it becomes important to model the hysteresis effects. It is also possible that other dampers shows a larger delay than the ones tested.

Friction models in general lead to slow simulations, especially when parametrised physically. Both the *LuGre* model and the tanh model become tedious to solve when parametrised more physically. The *LuGre* model can be parametrised with less stiff bristles, to make it easier for the solver. However this leads to an unphysical large phase shift between force and velocity, resulting in a stiffer system. The result of this can be for example seen in Figure 4.19, using $sigma = 1e4$. A stiffer and more physically correct bristle stiffness (i.e

$sigma = 1e6$) instead leads to slower simulations. The same goes for tanh friction, having a steep slope leads to very slow simulation times. The $LuGre$ model and the tanh model were especially problematic for the solvers when placed in parallel with the damper. When the friction is modeled stiff the solvers will give errors, which is why different parameters were used for the friction parallel to the damper, in comparison to parallel with unsprung (UM) and sprung mass (SM). Friction by hybrid modeling however worked very reliable across the damper. At higher frequencies there is a larger difference between the friction models. When the $LuGre$ and tanh friction tends to lower the transmissibility for the unsprung mass, the hybrid friction instead brings the transmissibility up. This can be seen in Figure 4.22. At the low frequencies all friction models behave similar, regardless if placed in parallel with SM and UM or parallel with the damper. Since dynamic friction acts like velocity independent damping during relative movement, it will lower the transmissibility, but due to stick-slip friction during the end point of the wheeltravel, the suspension system will be momentarily stiff, bringing the eigenfrequency up. Note that in the Dymola simulations the dynamic friction force is as big as the static, this is usually not the case. By lowering the dynamic friction force the system will see less damping, while still having similar stick slip behaviour. Thus lowering the dynamic friction should bring both the transmissibility and eigenfrequency up. If the friction force is higher than the applied force, i.e. the suspension is stuck during the entire excitation, both eigenfrequency and transmissibility will be much higher, as the damping ratio is decreased due to a non working damper. This since stiffness is increased due to the top mount bushing being an additional parallel spring. This scenario is seen in the measurement data in Figure 4.6. In Figure 4.25 the same scenario is simulated, and similar trends can be seen. However the correlation is not good. This could be due to no proper parametrisation in bushings (same as Car B is used, due to no measurements for Car A). The tire characteristics also become more important with respect to the transmissibility to sprung mass when the suspension is locked.

Friction implementation in the Adams model was a little bit more problematic than in Dymola. As the model complexity in Adams is higher with regard to degrees of freedom, part properties and test procedure implementation (modelled shaker rig), the simulation times where significantly larger than in Dymola. Also the implementation of non inbuilt features like other friction and damper models is not trivial. Since with Dymola a tool was available where this was done more easy, plus that time was a limiting factor in this investigation, non of this was done. As mentioned above, the Dymola model showed that the influence of damper modeling was rather small on the overall results, the standard force-velocity model in Adams was used as before. Friction was added to the model by using the inbuilt friction routine in Adams. As in Dymola this resulted in convergence problems. Therefore the friction was implemented in different steps. With the full implementation in dampers and ball joints, simulation time increased up to 4 days running on 8 cores on the Volvo cluster. Therefore Adams was not perfectly suited to investigate changes in the results due to changed friction parametrisation. Instead some selected parametrisations based on knowledge from the physical test and Dymola simulations where used to see the impact on the most complex simulation level and compare them to each other. Comparing the initial model results to the ones from the models with friction, it can be seen that the implementation of friction also decreases the transmissibility and increases the eigenfrequency as expected. When friction is used only in the dampers, it is not possible to reach the real eigenfrequency without obtaining a too low transmissibility. This is improved when friction is also implemented in the ball-joints. A reason for this could be, that when the damper is in stiction, only the top mount acts as an additional parallel spring, but when on of the ball joints is in stiction, all bushings act as parallel springs. This results in a highly increased stiffness, without getting additional damping from dynamic friction when the friction is increased in the damper. Nevertheless, the problem remained. There could be many reasons for this, but the ones deemed most likely are, that the friction model in Adams is not accurate enough (compare the different friction models in Dymola), other model parameters as damping could be a missing smaller part to obtain full correlation and/or the simulations deliver not accurate enough results due to solver issues. Friction also improved results in the high frequency range. However in the range between $6Hz$ to $15Hz$ correlation is not good and is not really influence by the amount of friction. It is possible that this is due to inaccurate tire or engine bushing representations.

6 Conclusion

In general a good understanding for vertical vibration insulation simulations could be gained during this work. The theory part was written with the aim not only to deliver knowledge to understand this thesis work, but also to be a starting point for other persons, that want to investigate problems within this field using physical testing and CAE simulations. It would have been liked to conduct more physical test during this study. Especially re-testing Car B on the shaker rig for different peak velocities and measuring accelerations at the engine block would have provided valuable information. Additionally tests on friction in the suspension assembly, a SPMM test with locked pads and vertical tire stiffness tests at different amplitudes[1] would have been desirable. It could provide data to parametrize friction more accurately, model frequency dependency of tires is Dymola and compare the Adams tire models to test data. This was not possible due to time, availability of the test car and no suitable testing facilities.

The main conclusion of this thesis is that friction seems to be the main reason why the initial model did not correlate to test data. It both gives a significant amount of damping, and additional system stiffness. A remaining task is to parametrize the friction, i.e. find the sources and divide the friction accordingly. It is also suggested to investigate whether a hybrid friction model can be implemented in Adams, this should give a more physical representation together with faster simulation times. By adding a more advanced damper model that captures the hysteresis behaviour, very little is gained. However it can still be important for other operating conditions. In the high frequency range there is a strong interaction between engine bushing and tires with regard to body transmissibility, this topic needs further investigation, and verification of the tire models are recommended. In general all suspension bushings should be modelled since the system is sensitive to change in dynamic stiffness and damping. All in all, the outcome of this thesis should be helpful to further improve vertical dynamics simulations at the Volvo Car Cooperation. Some parts, as the friction or damper modeling, might also be useful for lateral/longitudinal dynamics, since they could be equally or even more important for correlation in certain areas.

[1]similar to the way bushing tests are conducted

References

[Alt99]   F. Altpeter. *Friction Modeling, Identification and Compensation.* École Pplytechnique Federale de Lausanne, 1999.

[Anh03]   L. xuan Anh. *Dynamics of Mechanical Systems with Coulomb Friction.* Springer, 2003. ISBN: 978-3-642-05624-6.

[AO02]   M. Aberger and M. Otter. Modeling Friction in Modelica with the Lund-Grenoble Friction Model (Mar. 2002).

[Bar00]   A. J. Barber. *Accurate Models for Complex Vehicle Components using Empirical Methods.* SAE, Proceedings of the Automotive Dynamics & Stability Conference, P-354, ISSN 0148-7191, 2000.

[Bar93]   D. E. Baracat. *Damper Performace Development.* SAE paper No. 931691, 1993.

[BCT07]   S. K. Byoung, H. C. Chang, and K. L. Tae. *A study on radial directional natural frequency and damping ratio in a vehicle tire.* Applied Acoustics 68 538-556, 2007.

[Ben+13]   M. Benaziz et al. *Double Tube Shock Absorber Model for Noise and Vibration Analysis.* SAE, Int. J. Passeng. Cars - Mech. Syst. 6(2), 2013.

[Bes+10]   D. Besdo et al. *Elastomere Friction. Theory, Experiment and Simulation.* Springer, 2010. ISBN: 978-3-642-10656-9.

[Cam81]   C. Campbell. *Automobile Suspensions.* Chapman and Hall, 1981. ISBN: 978-1-4613-3391-3.

[com16]   W. common. *Viscoelasticity.* 2016. URL: https://en.wikipedia.org/wiki/Viscoelasticity.

[CWT95]   S. Cafferty, K. Worden, and G. Tomlinson. *Characterization of Automotive Shock Absorbers Using Random Excitations.* IMechE, Proceedings of the Institution of Mechanical Engineers, Vol. 209, 1995.

[Dix07]   J. C. Dixon. *The Shock Absorber Handbook.* John Wiley & Sons, Ltd, 2007. ISBN: 0-7680-0050-5.

[Duy97]   S. Duym. *An Alternative Force State Map for Shock Absorbers.* IMechE, Proceedings of the Institution of Mechanical Engineers, 211:3, pg. 175, 1997.

[Fas94]   J. W. Fash. *Modeling of Shock Absorber Behavior using Artificial Neural Networks.* SAE, International Congress & Exposition Detroit, ISSN 0148-7191, 1994.

[Fin89]   W. N. Findley. *Creep and Relaxation of Nonlinear Viscoelastic Materials. with an introduction to linear viscoelasticity.* Dover Publications, INC, 1989. ISBN: 0-486-66016-8.

[GM09]   G. Genta and L. Morello. *The Automotive Chassis.* Springer, 2009. ISBN: 978-1-4020-8674-8.

[HE11]   B. Heissing and M. Ersoy. *Chassis Handbook.* Vieweg + Teubner, 2011. ISBN: 978-3-8348-0994-0.

[HG81]   B. B. Hall and K. Gill. *The Mechanics of Automotive Hydraulic Dampers at High Stroking Frequencies.* Vehicle System Dynamics, 10:2-3, pp.82-85, 1981.

[ISO95]   ISO. Mechanical vibration Road surface profiles Reporting of measured data. *ISO 8608:1995* (Sept. 1995).

[Jac14]   B. Jacobson. *Vehicle Dynamics Compendium.* CHALMERS, 2014.

[Kee11]   K. J. Keesman. *System Identification. An Introduction.* Springer, 2011. ISBN: 978-0-8572-9522-4.

[KM86]   R. Karadayi and G. Y. Masada. A Non-linear shock-absorber Model. *Symposium on Simulation and Control of Ground Vehicles and Transportation Systems* (1986), 149–165.

[Kow+01]   D. Kowalski et al. *The Effect of Different Input Excitation on the Dynamic Characterization of an Automotive Shock Absorber.* SAE, Proceedings of the 2001 Noise and Vibration Conference, NOISE2001CD), 2001.

[KP03]   F. Karlsson and A. Persson. *Modelling Non-Linear Dynamics of Rubber Bushings - Parameter Identification and Validation.* Lund University, 2003.

[LaJ96]   J. C. LaJoie. *Damper Performace Development.* SAE paper No. 962551, 1996.

[Mil06]   J. Millard F. Beatty. *Principles of Engineering Mechanics: Volume 2. Dynamics. The Analysis of Motion.* Springer, 2006. ISBN: 978-0-38723-704-6.

[MTS16]   MTS. *Damper Test Systems.* 2016. URL: https://www.mts.com/en/products/producttype/test-systems/load-frames-uniaxial/servohydraulic/damper/index.htm (visited on 05/12/2016).

[NFB07]   D. B. Nguyen, A. A. Ferri, and O. A. Bauchau. *Efficient Simulation of a Dynamic System with LuGre Friction.* Journal of Computational and Nonlinear Dynamics, Vol. 2, 2007.

[OEM99]   M. Otter, H. Elmqvist, and S. E. Mattsson. Hybrid Modeling in Modelica based on the Synchronous Data Flow Principle (Aug. 1999).

[PC75]   G. R. Potts and T. T. Csora. *Tire Vibration Studies: The State of the Art.* Tire Science and Technology, TSTCA, Vol. 3, No. 3, 1975.

[Plo13]   M. Ploechl. *Road and Off-Road Vehicle System Dynamics Handbook*. CRC press, 2013. ɪsʙɴ: 978-0-8493-3322-4.

[Pop10]   K. Popp. *Ground Vehicle Dynamics*. Springer, 2010. ɪsʙɴ: 978-3-540-68553-1.

[Rey92]   K. Reybrouck. *On the Non-Linear Characteristics of Automotive Shock Absorbers*. SAE, Vehicle Suspension System Advancements, SP-1031, 1992.

[SL81]   L. Segel and H. H. Lang. *The Mechanics of Automotive Hydraulic Dampers at High Stroking Frequencies*. Vehicle System Dynamics, 10:2-3, pp.82-85, 1981.

[Sof14]   C. S. Software. *FTire - Flexible Structure Tire Model. Modelization and Parameter Specification*. Gipser + Hofmann, Ingenieure, Partnerschaft, 2014.

[SWT92]   C. Surace, K. Worden, and G. R. Tomlinson. *On the Non-Linear Characteristics of Automotive Shock Absorbers*. IMechE, Proceedings of the Institution of Mechanical Engineers, Part D: Journal of Automobile Engineering, Vol. 206, 1992.

[TBS00]   R. K. Taylor, L. L. Bashford, and M. D. Schrock. *Methods for Measuring Vertical Tire Stiffness*. American Society of Agricultural Engineers, Vol. 43(6), 2000.

[Web09]   W. Weber. *Fahrdynamik in Perfektion*. Motorbuch Verlag, 2009. ɪsʙɴ: 978-3-6130-3254-5.

Appendices

A Damper model with hysteresis

In all figures the damper model is overlaid with the test results for the corresponding velocity and amplitude. Figure 6.1 shows results for $1047\frac{mm}{s}$ at 38.5 and $15mm$ amplitude. The correlation is good, only the behavior in the low speed area is not captured in every detail. At the plots for $15mm$ amplitude it can be seen that the control system of the damper rig was not able to deliver the desired $1047\frac{mm}{s}$. Instead the velocity in the test was slightly higher around $1150\frac{mm}{s}$.
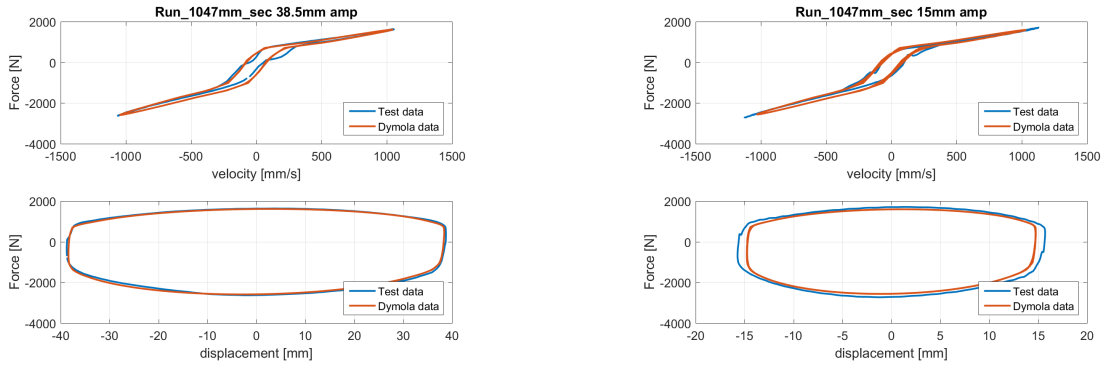
(a) *38.5 mm amplitude and 1047mm/s peak velocity*   (b) *15 mm amplitude and 1047mm/s peak velocity*

Figure 6.1: *Correlation of damper model in Dymola*

In Figure 6.2 the same amplitudes as above are tested but for a velocity of $393\frac{mm}{s}$. The correlation is also good here, only around the knees of the damper curves the two curves deviate in both plots. By looking at the force-deflection curves it can be seen that the difference is still small and acceptable considering the simplicity of the model.
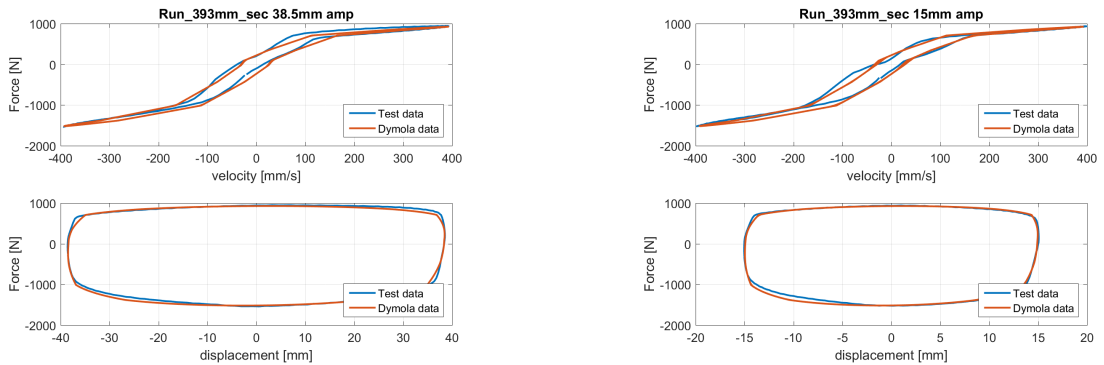
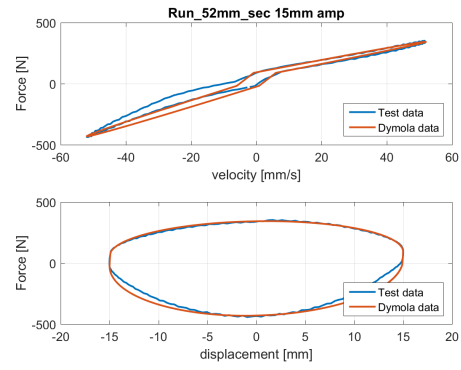(a) *38.5 mm amplitude and 393mm/s peak velocity*   (b) *15 mm amplitude and 393mm/s peak velocity*

Figure 6.2: *Correlation of damper model in Dymola*

Again the same amplitudes for an even lower velocity of $52\frac{mm}{s}$ are displayed in Figure 6.3. It becomes clear that the correlation tend to get worse for lower damper speeds. However the model is still not far off.
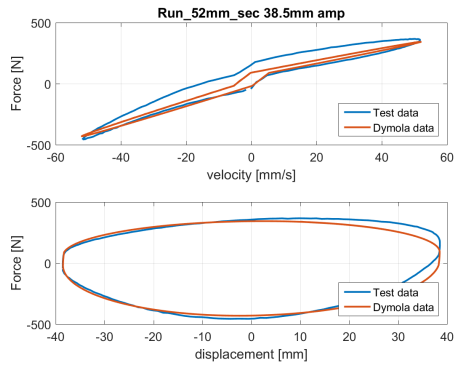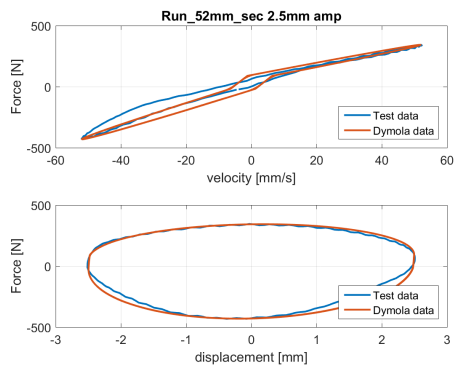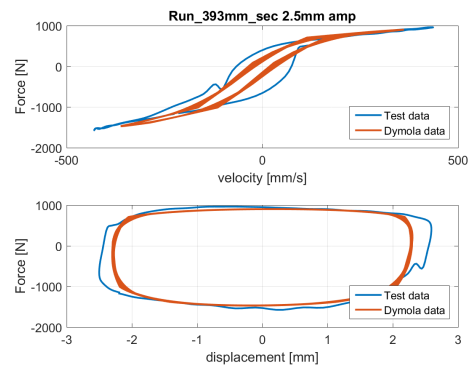
(a) *38.5 mm amplitude and 52mm/s peak velocity*

(b) *15 mm amplitude and 52mm/s peak velocity*

Figure 6.3: *Correlation of damper model in Dymola*

Finally in Figure 6.4 small amplitudes are simulated for low damper speeds $(52\frac{mm}{s})$. Especially for the high velocity test $(393\frac{mm}{s})$ the limitations of this model become apparent. It fails to capture the extensive hysteresis loop size as well as an occurring dip in the test data. Instead, it maintains the "normal" loop shape. For the low velocity $(52\frac{mm}{s})$ the model does not feature the different behavior in the rebound are (left side). But also here needs to be noted that the model doesn't fail to represent the damper.

(a) *2.5 mm amplitude and 52mm/s peak velocity*

(b) *2.5 mm amplitude and 393mm/s peak velocity*

Figure 6.4: *Correlation of damper model in Dymola*

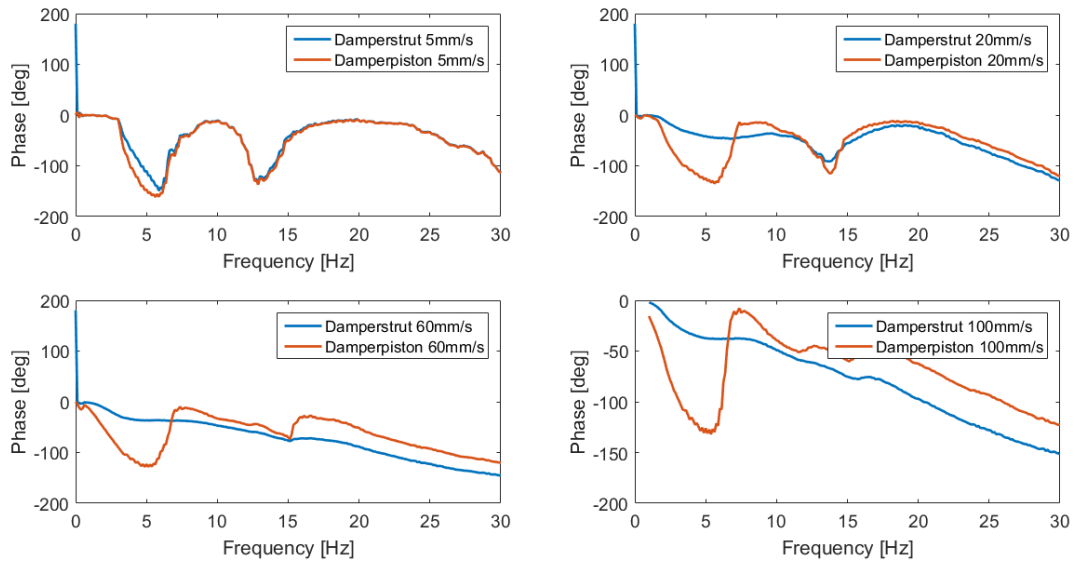# B   Shaker rig measurements

Figure 6.5: *Phase angle between road and damperstrut and road and damperpiston*
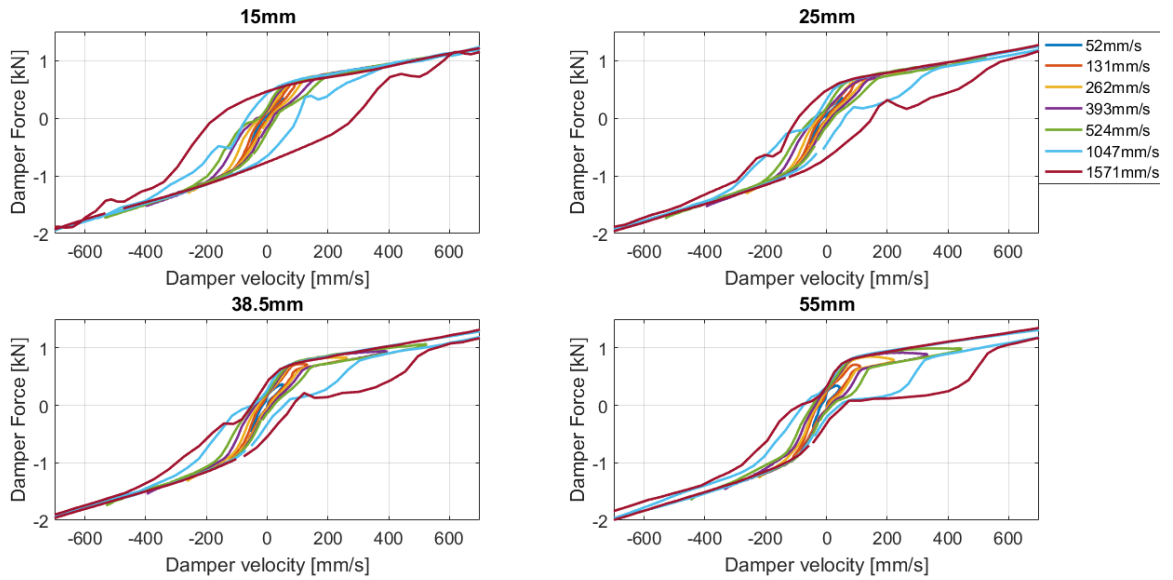
C   Damper test results

Figure 6.6: *Force velocity traces for bigger amplitudes*

D Damper tests performed Car A

Table 6.1: List of test points performed

|		50	50	50	50	50	50	50
	Amplitude [mm]	50	50	50	50	50	50	50
Test 1	Frequency [Hz]	0,17	0,42	0,83	1,25	1,67	3,33	5
	Peak velocity [mm/s]	53,41	131,95	260,75	392,70	524,65	1046,15	1570,80
	Amplitude [mm]	38,5	38,5	38,5	38,5	38,5	38,5	38,5
Test 2	Frequency [Hz]	0,22	0,55	1,08	1,62	2,17	4,32	6,49
	Peak velocity [mm/s]	53,41	131,95	260,75	392,70	524,65	1046,15	1 570,80
	Amplitude [mm]	30	30	30	30	30	30	30
Test 3	Frequency [Hz]	0,28	0,70	1,38	2,08	2,78	5,55	8,33
	Peak velocity [mm/s]	53,41	131,95	260,75	392,70	524,65	1046,15	1 570,80
	Amplitude [mm]	25	25	25	25	25	25	25
Test 4	Frequency [Hz]	0,34	0,84	1,66	2,50	3,34	6,66	10,00
	Peak velocity [mm/s]	53,41	131,95	260,75	392,70	524,65	1046,15	1 570,80
	Amplitude [mm]	15	15	15	15	15	15	15
Test 5	Frequency [Hz]	0,57	1,40	2,77	4,17	5,57	11,10	16,67
	Peak velocity [mm/s]	53,41	131,95	260,75	392,70	524,65	1046,15	1 570,80
	Amplitude [mm]	5	5	5	5	-	-	-
Test 6	Frequency [Hz]	1,70	4,20	8,30	12,50	-	-	-
	Peak velocity [mm/s]	53,41	131,95	260,75	392,70	-	-	-
	Amplitude [mm]	2,5	2,5	2,5	2,5	-	-	-
Test 7	Frequency [Hz]	3,40	8,40	16,60	25,00	-	-	-
	Peak velocity [mm/s]	53,41	131,95	260,75	392,70	-	-	-
	Amplitude [mm]	1	1	1*	1*	-	-	-
Test 8	Frequency [Hz]	8,50	21,00	*	*	-	-	-
	Peak velocity [mm/s]	53,41	131,95	260,75*	392,70*	-	-	-

E Adams initial model
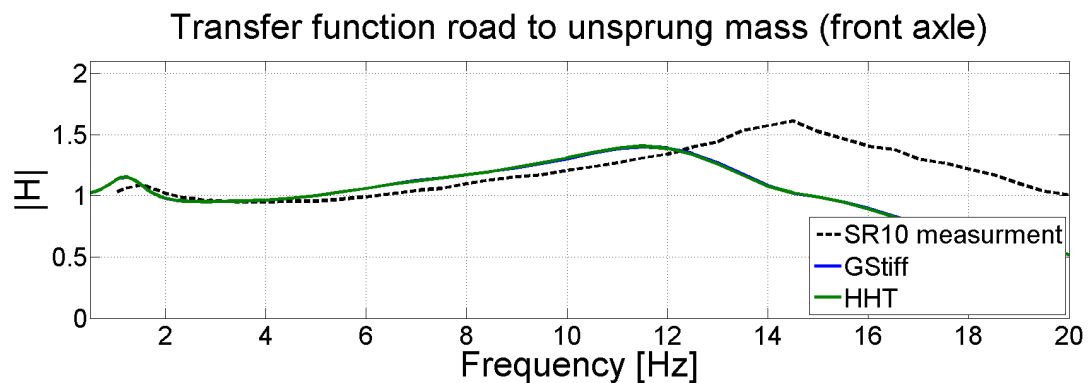
Figure 6.7: *Transmissibility $(0-20Hz$ front) road to rim for the initial model with different solvers*
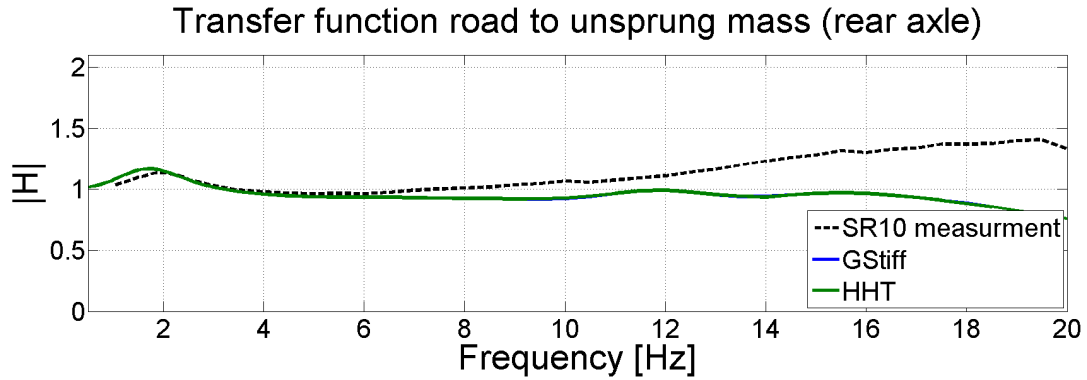
Figure 6.8: *Transmissibility (0 − 20Hz rear) road to rim for the initial model with different solvers*

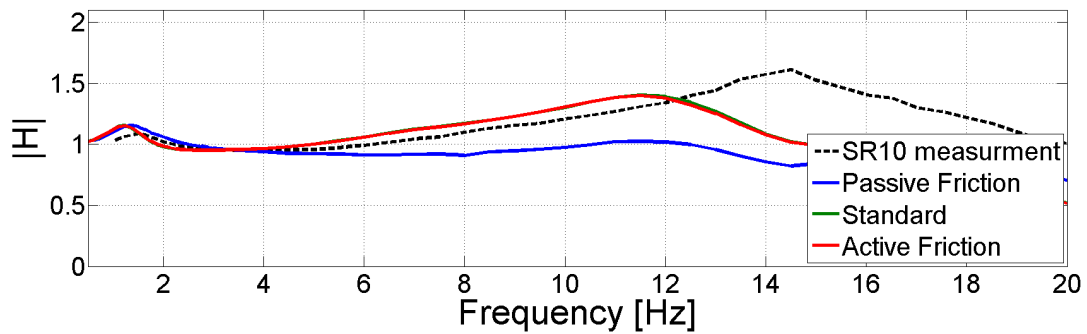## F   Adams model with friction at the front axle

Figure 6.9: *Transmissibility (0 − 20Hz front) road to rim for a model with friction in the front damper struts*
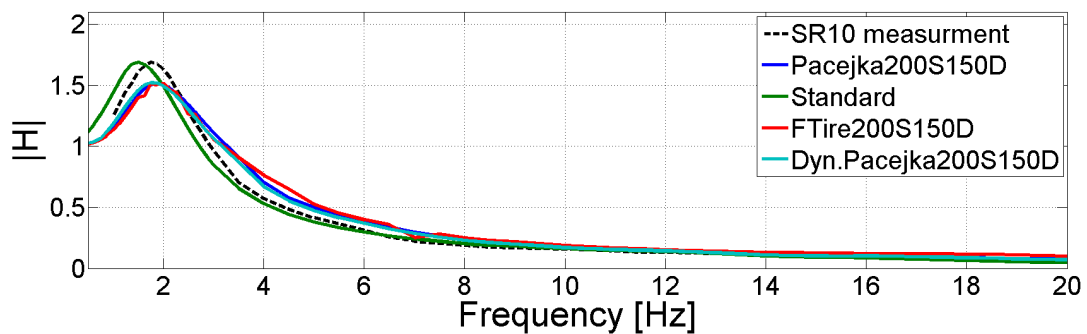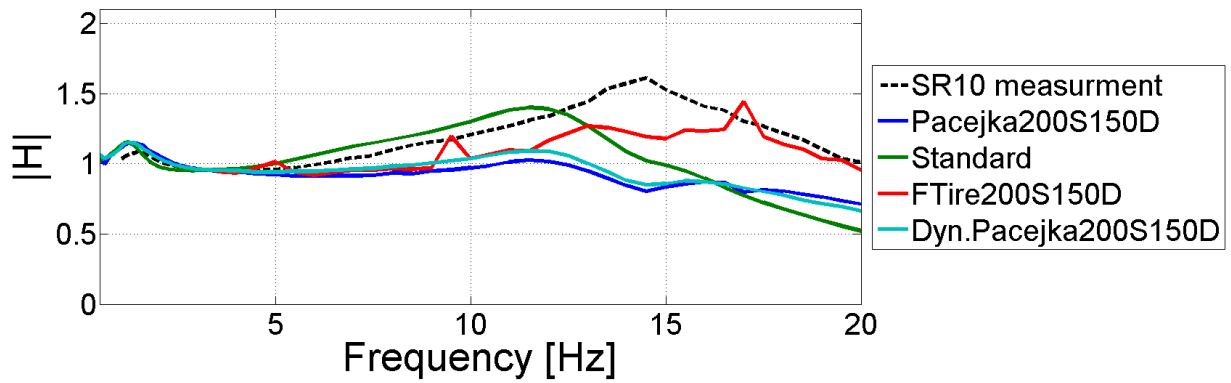
G   Adams model with friction in all dampers

Figure 6.10: *Transmissibility (0 − 20Hz rear) road to body for the model with friction implemented in all damper struts*

Figure 6.11: *Transmissibility (0 − 20Hz front) road to rim for the model with friction implemented in all damper struts*
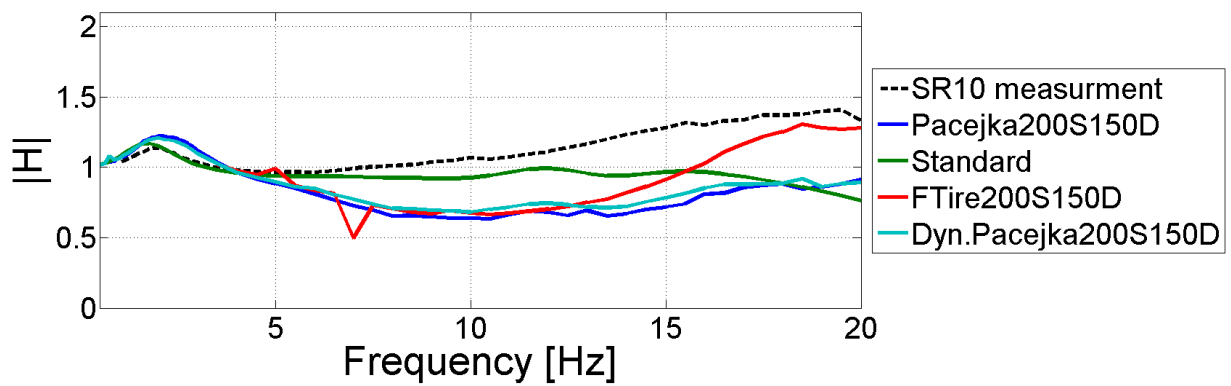

Figure 6.12: *Transmissibility (0 − 20Hz rear) road to rim for the model with friction implemented in all damper struts*

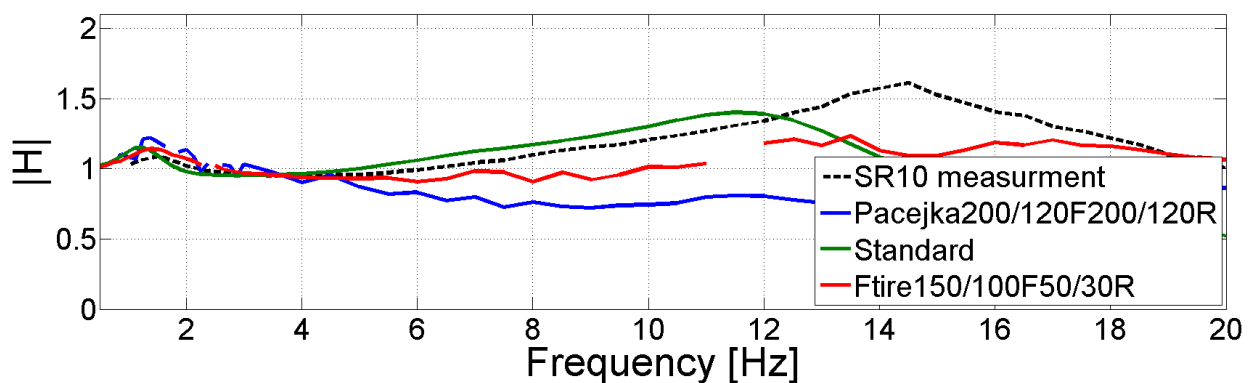# H   Adams model with friction in dampers and ball joints

Figure 6.13: *Transmissibility (0 − 20Hz front) road to rim for the model with friction implemented in all dampers and ball joints*
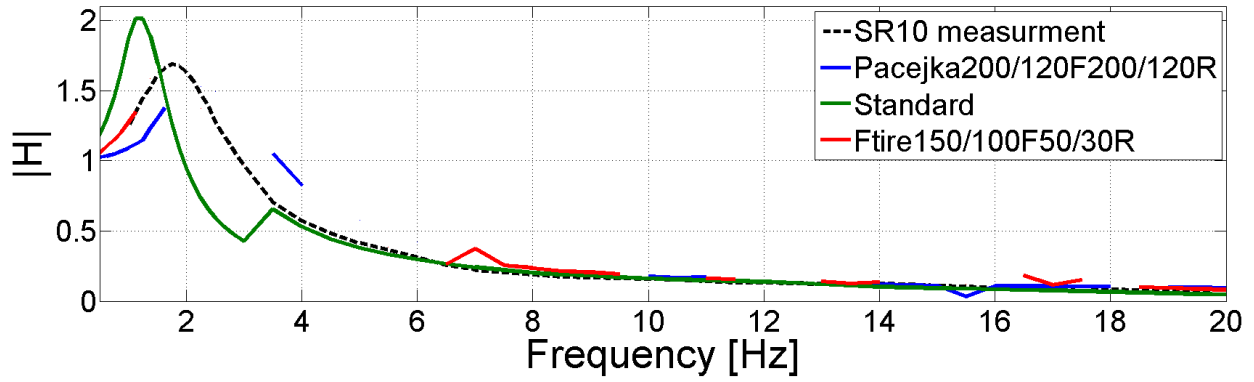
Figure 6.14: *Transmissibility (0 − 20Hz rear) road to body for the model with friction implemented in all dampers and ball joints*
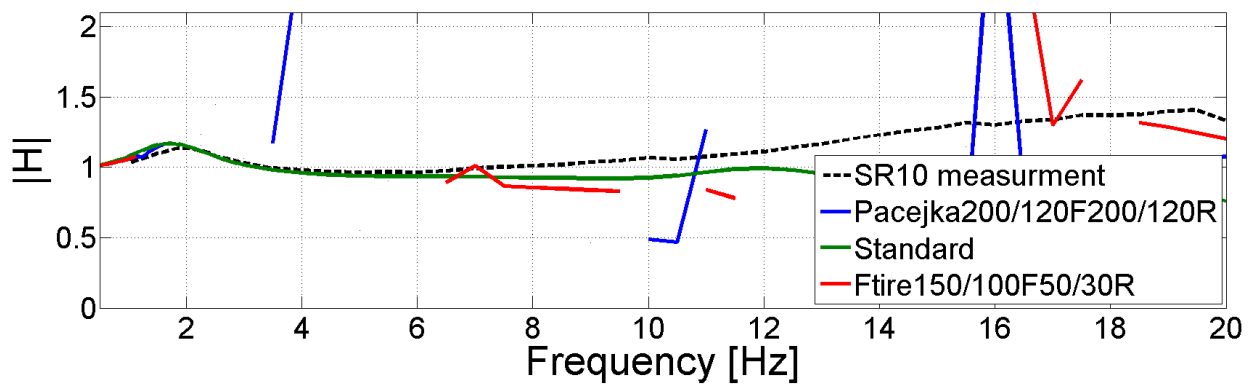

Figure 6.15: *Transmissibility (0 − 20Hz rear) road to rim for the model with friction implemented in all dampers and ball joints*